DIPLOMARBEIT

Susceptibility Imaging using CAIPIRINHA acceleration

zur Erlangung des akademischen Grades

Diplom-Ingenieur

im Rahmen des Studiums

Physikalische Energie- und Messtechnik

eingereicht von

Jan Bertle, BSc

Matrikelnummer 11705346

ausgeführt am Atominstitut

der Fakultät für Physik der Technischen Universität Wien

in Zusammenarbeit mit dem Hochfeld MR Zentrum, Zentrum für Medizinische Physik und

Biomedizinische Technik, Medizinische Universität Wien

Betreuung:

Em.Univ.Prof. Dipl.-Ing. Dr.techn. Gerald Badurek

Assoc.Prof. Dr. Simon Robinson (Med. Univ. Wien)

Mitbetreuung:

Ass.Prof. Dipl.-Ing. Dr. techn. Karin Poljanc

Wien, 16.04.2024   _____   _____

                                                     Jan Bertle   Gerald Badurek

Master Thesis

Susceptibility Imaging using CAIPIRINHA acceleration

Submitted in partial fulfilment of the requirement for the degree of

Master of Science

in

Physical Energy and Measurement Engineering

by

Jan Bertle, BSc

Registration number 11705346

at the Atomic Institute

of the Faculty of Physics at the Vienna University of Technology

in cooperation with the HFMRC Centre, Centre for Medical Physics and Biomedical

Engineering, Medical University of Vienna

Supervised by:

Em.Univ.Prof. Dipl.-Ing. Dr.techn. Gerald Badurek

Assoc.Prof. Dr. Simon Robinson (Med. Univ. Wien)

Co-Supervision:

Ass.Prof. Dipl.-Ing. Dr. techn. Karin Poljanc

Vienna, 16.04.2024   _____   _____

                                            Jan Bertle   Gerald Badurek

Erklärung zur Verfassung der Arbeit

Jan Bertle,
Groxstraße 11b, 6800 Feldkirch, Austria

Hiermit erkläre ich, dass ich diese Arbeit selbstständig verfasst habe, dass ich die verwendeten Quellen und Hilfsmittel vollständig angegeben habe und dass ich die Stellen der Arbeit – einschließlich Tabellen, Karten und Abbildungen –, auf anderen Werken oder dem Internet im Wortlaut oder dem Sinn nach entnommen sind, auf jeden Fall unter Angabe der Quelle als Entlehnung kenntlich gemacht habe.

| Wien, 16. April 2024 | Jan Bertle |

Acknowledgements

At this point I would like to thank everyone who supported me throughout the course of my thesis. First and foremost, I would like to thank my supervisor from the Medical University of Vienna, Simon Robinson, since without his expert advice and guidance this work would not have been possible. His help, be it relating to the subject or outside, was invaluable for the completion of my thesis. I would also like to express my gratitude to Gerald Badurek and Karin Poljanc for allowing me to work in this fascinating subject by supervising my thesis at the Vienna University of Technology.

I would also like to personally thank Gert Reiter, for coordinating the communication with the Siemens Developers and of course the Developers themselves, who took their time to respond and provide insights into our findings. A special thanks also goes out to Korbinian Eckstein, who helped guide me during my short adventure into ICE programming.

Furthermore, I would like to express my gratitude towards my family and friends, for supporting me during the course of my thesis, as well as all my colleagues at the HFMRC in Vienna, which whom I had many interesting talks over coffee.

Abstract

Magnetic Resonance Imaging (MRI) is an extremely versatile diagnostic imaging modality. It is widely used in a clinical setting to acquire structural and functional images of for example the brain, abdomen and knee. While MRI is not only highly adaptable, as well as very safe, one main problem is that the duration of some brain scans can exceed 10 minutes. Therefore, acceleration methods have been developed in order to speed up the data acquisition process by undersampling the raw data matrix (k-space).

This thesis is concerned with the comparison of two specific MRI acceleration methods for high- and ultra-high field structural brain imaging. The main focus was on multi-echo susceptibility weighted imaging (SWI), a method which allows for added generation of contrast for certain tissues based on their susceptibility differences. The acceleration methods in question are GRAPPA and the more recently developed CAIPIRINHA acceleration. GRAPPA allows for an acceleration of the data acquisition time by undersampling k-space. CAIPI is based on GRAPPA, and grants more flexibility in choosing the desired undersampling scheme, allowing for a spatially more even sampling of k-space which should result in better image quality. The aim of this work was to qualitatively and quantitatively compare these two methods using a multi-echo gradient-echo sequence and evaluate whether an implementation of CLEAR-SWI into the VIBE sequence would be beneficial.

Measurements were made of spherical oil phantoms and human subjects at 3T and 7T field strengths using various GRAPPA and CAIPI acceleration schemes. Additionally, the effects of changing parameters such as the number of reference lines, as well as the way these reference lines were acquired, be it integrated into the main scan or in a separate scan, had on the signal-to-noise ratio of the resulting images was investigated. SNR maps of the phantom scans were calculated, to quantify the image quality of both acceleration methods at comparable total acceleration factors. Phase images of the in-vivo scans were reconstructed, which were then used to create SWI images for qualitative comparisons of the in-vivo measurements.

Contrary to expectations, the images acquired with the more recently developed CAIPIRINHA acceleration method showed overall lower calculated SNR values in the phantom measurements compared to their GRAPPA counterparts. Using reference lines which were integrated into the main sequence, instead of a more conventional separate reference line scan, resulted in a roughly twofold increase in acquisition time and caused strong artifacts to arise for later echoes, while also substantially increasing the reconstruction times.

Optimal CAIPIRINHA schemes for these measurements were examined for total acceleration factors of R = 4 and R = 6, with successive measurements using these CAIPI configurations. Further qualitative comparisons of magnitude- and SWI images demonstrated that no clear improvements could be observed for CAIPIRINHA acceleration over GRAPPA. Additionally, the

results comparing magnitude images of GRAPPA and CAIPIRINHA accelerated images at total acceleration factors of R = 4, published in the literature, could not be replicated in this study.

Higher SNR efficiency for GRAPPA accelerated scans with R = 4 was observed for an increased number of reference lines. An implementation of higher default values of reference lines in the SWI protocol should therefore lead to noticeably better image quality at just fractionally higher acquisition times. Images acquired with CAIPI acceleration, with R = 6, in conjunction with a larger field-of-view and higher resolution showed slightly improved image quality compared to a less accelerated (R = 4) GRAPPA scan with a similar acquisition time, due to a decrease in aliasing artifacts.

In conclusion, CAIPIRINHA acceleration showed no clear improvement in SNR or overall image quality. Nonetheless, a future implementation of CLEAR-SWI into the VIBE sequence might still be beneficial, given that the GRAPPA acceleration method can also be used in VIBE. Some applications might still profit from the added flexibility that CAIPIRINHA allows for in the achievable undersampling patterns, e.g. depending on the distribution of coils in relation to the object. Methods such as increasing the default number of reference lines or using higher accelerated factors in conjunction with larger FOV and higher resolution, showed positive results regardless of the acceleration method used.

Kurzfassung

Die Magnetresonanztomographie (MRT) ist ein äußerst vielseitiges bildgebendes Diagnoseverfahren. Sie wird im klinischen Alltag häufig eingesetzt, um strukturelle und funktionelle Bilder z. B. des Gehirns, des Abdomens und des Knies zu erhalten. Die MRT ist nicht nur äußerst anpassungsfähig, sondern auch sehr sicher. Ein Hauptproblem ist jedoch, dass die Dauer einiger Gehirnscans bis zu 10 Minuten überschreiten kann. Daher wurden Beschleunigungsverfahren entwickelt, um den Datenerfassungsprozess zu verkürzen. Diese Beschleuningungsmethoden basieren in der Regel auf einer Unterabtastung der Rohdatenmatrix, dem sogenannten k-Raum.

Diese Arbeit befasst sich mit dem Vergleich zweier MRT-Beschleunigungsmethoden für die strukturelle Hirnbildgebung im Hoch- und Ultrahochfeld. Das Hauptaugenmerk lag dabei auf der Multi-echo Suszeptibilitäts-gewichteten Bildgebung (SWI). Diese Methode ermöglicht eine zusätzliche Kontrasterzeugung für bestimmte Gewebe auf Grundlage ihrer Suszeptibilitätsunterschiede. Bei den Beschleunigungsmethoden in Frage handelt es sich um GRAPPA, und die deutlich neuere CAIPIRINHA-Beschleunigung. GRAPPA ermöglicht eine Beschleunigung der Datenerfassungszeit durch Unterabtastung des k-Raums. CAIPI basiert auf GRAPPA und bietet eine erhöhte Flexibilität bei der Wahl des gewünschten Unterabtastungsschemas. Dadurch lässt sich eine räumlich gleichmäßigere Abtastung des k-Raums erreichen, was zu einer besseren Bildqualität führen sollte. Ziel dieser Arbeit war es, diese beiden Methoden anhand einer Multi-echo Gradientenecho-Sequenz qualitativ und quantitativ zu vergleichen und zu bewerten, ob eine Implementierung von CLEAR-SWI in die VIBE-Sequenz vorteilhaft wäre.

Es wurden Messungen an sphärischen Ölphantomen und freiwilligen Probanden bei Feldstärken von 3T und 7T unter Verwendung verschiedener GRAPPA- und CAIPI-Beschleunigungsschemata durchgeführt. Darüber hinaus wurde untersucht, welche Auswirkungen die Änderung von Parametern wie der Anzahl der Referenzlinien auf das Signal-Rausch-Verhältnis der resultierenden Bilder hatte. Neben der Anzahl wurde auch der Modus mit der diese Referenzlinien aufgenommen wurden, entweder integriert in den Haupt-Scan oder in einem separaten Scan, untersucht. Die SNR Verteilung der Phantom-Scans wurden berechnet, um die Bildqualität beider Beschleunigungsmethoden bei vergleichbaren Gesamtbeschleunigungsfaktoren zu quantifizieren. Die Phasenbilder der In-vivo-Scans wurden rekonstruiert und anschließend zur Erstellung von SWI-Bildern für qualitative Vergleiche der In-vivo-Messungen verwendet.

Entgegen den Erwartungen zeigten die mit der neueren CAIPIRINHA-Beschleunigungsmethode aufgenommenen Bilder in den Phantommessungen insgesamt niedrigere berechnete SNR-Werte als ihre GRAPPA-Pendants. Die Verwendung von Referenzlinien, die in die Hauptsequenz integriert wurden, anstelle eines konventionellen

separaten Referenzlinien-Scans, führte zu einer etwa zweifachen Erhöhung der Akquisitionszeit und verursachte starke Artefakte bei spätere Echos, während sich auch die Rekonstruktionszeiten erheblich erhöhten.

Optimale CAIPIRINHA-Schemata für diese Messungen wurden für Gesamtbeschleunigungsfaktoren von R=4 und R=6 untersucht, wobei die darauf folgenden Messungen mit diesen CAIPI-Konfigurationen durchgeführt wurden. Weitere qualitative Vergleiche von Magnituden- und SWI-Bildern zeigten, dass für die CAIPIRINHA-Beschleunigung keine eindeutigen Verbesserungen gegenüber GRAPPA festgestellt werden konnten. Außerdem konnten die in der Literatur veröffentlichten Ergebnisse zum Vergleich der Magnitudenbilder von GRAPPA und CAIPI bei Gesamtbeschleunigungsfakor R=4 nicht reproduziert werden.

Eine höhere SNR-Effizienz für mit R=4 beschleunigte GRAPPA Scans wurde bei einer höheren Anzahl von Referenzlinien beobachtet. Eine Implementierung höherer Standardwerte für die Referenzlinien im SWI-Protokoll sollte daher zu einer deutlich besseren Bildqualität bei nur geringfügig höheren Aufnahmezeiten führen. Bilder, die mit CAIPIRINHA Beschleunigung mit R=6 in Verbindung mit einem größeren Sichtfeld und höherer Auflösung aufgenommen wurden, zeigten eine leicht verbesserte Bildqualität im Vergleich zu einem weniger beschleunigten (R=4) GRAPPA Scans mit ähnlicher Aufnahmezeit, was auf eine Verminderung von Aliasing-Artefakten zurückzuführen ist.

Zusammenfassend lässt sich sagen, dass die CAIPIRINHA-Beschleunigung keine eindeutige Verbesserung des SNR oder der Gesamtbildqualität bewirkte. Eine künftige Implementierung von CLEAR-SWI in die VIBE-Sequenz könnte aber auch dann von Vorteil sein, wenn CAIPIRINHA selbst nicht zu den erwarteten Verbesserungen der Bildqualität führt, da die herkömmlichere GRAPPA-Beschleunigungsmethode auch in VIBE verwendet werden kann. Einige spezifische Anwendungen könnten dennoch von der zusätzlichen Flexibilität profitieren, die CAIPIRINHA in den erreichbaren Unterabtastungsmustern ermöglicht. Methoden wie die Erhöhung der Standardanzahl von Referenzlinien oder die Verwendung höherer Beschleunigungsfaktoren in Verbindung mit einem größeren FOV und einer höheren Auflösung zeigten positive Ergebnisse unabhängig von der jeweiligen Beschleunigungsmethode.

List of Abbreviations:

A Simple Phase Image Reconstruction for multi-Echo acquisitions	(ASPIRE)
Acquisition Time	(TA)
Alzheimer's Disease	(AD)
Attention Deficit Hyperactivity Disorder	(ADHD)
Autocalibration Signal	(ACS)
Computer Tomography	(CT)
Contrast-to-Noise Ratio	(CNR)
Contrast-weighted, Laplace-unwrapped, bipolar multi-Echo, ASPIRE-combined, homogeneous, improved Resolution SWI	(CLEAR-SWI)
Controlled Aliasing in Parallel Imaging Results In Higher Acceleration	(CAIPIRINHA)
Digital Imaging and Communications in Medicine	(DICOM)
Echo Time	(TE)
Fast Low Angle Shot	(FLASH)
Field of View	(FOV)
Free Induction Decay	(FID)
GeneRalized Autocalibrating Partially Parallel Acquisitions	(GRAPPA)
Gradient Recalled Echo	(GRE)
High Field MR Centre	(HFMRC)
Image Calculation Environment	(ICE)
Magnetic Resonance Imaging	(MRI)
Minimum Intensity Projection	(mIP)
Multiple Sclerosis	(MS)
Neuroimaging Informatics Technology Initiative	(NIfTI)
Nuclear Magnetic Resonance	(NMR)
Parallel Imaging	(PI)
Parkinson's Disease	(PD)
Phase Encoding	(PE)
Positron Emission Tomography	(PET)
Quantitative Susceptibility Mapping	(QSM)
Radio Frequency	(RF)

Region of Interest   (ROI)

Repetition Time   (TR)

Retro-Reconstruction   (RR)

Signal-to-Noise Ratio   (SNR)

Susceptibility Weighted Imaging   (SWI)

Volume of Interest   (VOI)

Table of Contents

1 Introduction

1.1 Motivation

Magnetic Resonance Imaging (MRI) is a highly versatile and diagnostic imaging modality. It is used extensively in a clinical setting to acquire not only structural but also functional images of various parts of the human body, such as the brain, abdomen or knee. Not only is this imaging method highly adaptable, but it is also very safe compared to other comparable methods like X-ray CT or PET, which expose patients to relatively high doses of ionizing radiation [1].

Conventional MRI scanners, especially in clinical settings, range between 1.5 and 3.0 Tesla. With higher field strengths, such as the 7 Tesla scanner used in the High Field MR Centre (HFMRC) in Vienna, additional detail can be visualized and enhanced contrasts can be generated [2].

MRI is not without disadvantages, however, as high-resolution scans correspond to long data acquisition times (TA), with some brain scans for example taking 5-10 minutes. This not only triggers anxiety in many patients [3], but also leads to movement artifacts in the image, which MRI is very prone for. These movement artifacts [4] manifest themselves as ghosting and blurring, and greatly decrease the usability of these scans for medical diagnosis. Subject motion is especially problematic in children, for whom remaining still for extended periods of time is more challenging. Additionally, there are a number of diseases which make it exceptionally difficult for patients to stay still sufficiently long enough to acquire the data required. Examples of such diseases include ADHD (attention deficit hyperactivity disorder), Alzheimer's disease (AD) and Parkinson's disease (PD) [5, 6].

Considering these movement artifacts and the stress-induced anxiety of patients, as well as general drawbacks in cost and logistics caused by long scan times, the development of acceleration methods for magnetic resonance imaging has many advantages. Parallel Imaging techniques (PI) [7] rely on acquiring a reduced number of k-space lines according to a pre-defined undersampling pattern. K-space [8] is the space of the acquired signal in MRI; the spatial frequency domain which corresponds to the Fourier Transform of the image. . Undersampling k-space can drastically reduce the acquisition time, but leads to a decrease in signal-to-noise ratio (SNR) [9]. With the signal-to-noise ratio being an important metric of image quality. Besides the decrease in SNR, the undersampling of k-space causes aliasing artifacts.

One of the most widely used parallel imaging techniques is GRAPPA (GeneRalized Autocalibrating Partially Parallel Acquisitions) [10], which uses a radio frequency (RF) coil array for parts of the spatial encoding. This spatial encoding would normally be done through the use of field gradients and therefore cost valuable scan time. To make this possible, a

comparatively small number of phase encoding lines need to be acquired conventionally, which are called the autocalibration signal (ACS) reference lines. These reference lines contain information about the RF coil sensitivities and can be used to reconstruct the missing k-space information. While this method greatly reduces acquisition times and still retains high SNR, it causes aliasing artifacts which then need to be removed during the image reconstruction.

CAIPIRINHA (Controlled Aliasing in Parallel Imaging Results In Higher Acceleration) [11] is a more recently developed parallel imaging method based on GRAPPA. Compared to GRAPPA, CAIPI allows for a higher degree of freedom in choosing the sampling patterns, by shifting every following k-space line by a chosen factor, a feature that is referred to as the reorder shift. Through this reorder shift, the raw data, which is stored in k-space, can be sampled in a spatially more evenly distributed manner. This is especially useful at higher acceleration factors, and for acceleration in multiple directions, as in these cases the distances between the actually sampled data points can become quite large. The resulting unevenly distributed k-space sampling pattern makes interpolating between the individual data points suboptimal. This is why applying the CAIPI reorder shift, and therefore sampling k-space more evenly, allows for better utilization of the coil sensitivities, which should increase the SNR.

In contrast to classical MRI, which only utilizes the magnitude information of the acquired complex signal, Susceptibility Weighted Imaging (SWI) [12] takes advantage of the phase information. The phase is proportional to local field inhomogeneity, which is caused by susceptibility variations between different types of tissues. This allows for the creation of additional contrast [13] between tissues with concentration differences in deoxygenated blood, calcium or iron. Susceptibility weighted imaging benefits greatly from high- and ultrahigh field strengths, as the local field differences are proportional to the external magnetic field. The problem that emerges at these ultra-high fields is that the complex phase filtering used in standard SWI, which was originally developed for 1.5 T, causes artifacts to arise if inhomogeneities in the magnetic fields B_1 and B_o are present. To counteract this, CLEAR-SWI (Contrast-weighted, Laplace-unwrapped, bipolar multi-Echo, ASPIRE-combined, homogeneous, improved Resolution SWI) [12] was developed. This method has a number of advantages over standard SWI, including higher contrast-to-noise (CNR) ratio at ultra-high field strengths, a decrease in signal dropouts and a reduction in artifacts. It also utilizes the highly efficient and robust ASPIRE (A Simple Phase Image Reconstruction for multi-Echo acquisitions) [14] method to combine the multi-echo phase information from the individual coils in a phased array radiofrequency coil.

Quantitative Susceptibility Mapping (QSM) [15] is a related method, with its main advantage being that the susceptibility can be quantified. This allows for the observation of venous oxygen saturation and in vivo iron content [15-17]. This is especially beneficial as iron has shown to accumulate in the brains of patients suffering from diseases such as Parkinson's disease (PD), multiple sclerosis (MS) and Alzheimer's disease (AD) [16].

The previously mentioned CLEAR-SWI and ASPIRE reconstructions are used in conjunction with a gradient recalled echo (GRE) sequence based on the GRE product sequence supplied by SIEMENS, the vendor of the MRI scanners used at the High Field MR Centre in Vienna. This GRE sequence is limited in terms of acceleration methods to GRAPPA, with the newer CAIPIRINHA not yet being implemented. In contrast to that, the volumetric interpolated breath-hold examination [18] (VIBE) sequence, is a variant of the GRE sequence which allows undersampling and reconstruction with CAIPIRINHA. The ASPIRE and CLEAR-SWI methods have yet to be integrated into the VIBE sequence, to allow CAIPIRINHA acceleration of SWI and QSM.

A future implementation of ASPIRE and subsequently CLEAR-SWI into the VIBE sequence could lead to higher usable acceleration factors with a decreased amount of aliasing artifacts through the use of the more recently developed CAIPIRINHA method. The expected increase in SNR could either be used to increase the image quality in scans with similar acquisition times as with GRAPPA, or to decrease the scan time while still retaining the same signal-to-noise ratio.

1.2 Aim

The aim of this project was to use the VIBE sequence to quantify the difference in SNR between the GRAPPA and CAIPIRINHA acceleration methods, both in vivo and for phantom measurements. The purpose of these experiments was to quantify the SNR change with regards to conventional undersampling and reconstruction using GRAPPA, and identify the optimum undersampling scheme for the brain, given the geometry of the coils. Then it could be decided if a future implementation of ASPIRE and CLEAR-SWI into the VIBE sequence would be beneficial.

Additionally, scan parameters and other methods to increase the signal-to-noise ratio in both GRAPPA and CAIPIRINHA were searched for, in order to possibly improve the current applications of CLEAR-SWI in conjunction with the GRE sequence.

2 Theory

2.1 Principles of Magnetic Resonance Imaging

Magnetic resonance imaging is a well-established, versatile and non-invasive imaging technique which is used extensively in a clinical setting. It is based on the physical principle of nuclear magnetic resonance (NMR) [19] and uses a strong magnet field to align a fraction of the spins of certain nuclei, most commonly the nucleus of the hydrogen atom, which is a proton. Signal can be obtained from a variety of different tissues without requiring ionizing radiation as is the case in computer tomography (CT) scans or x-ray.

2.1.1 Magnetic Spin and Magnetization

Atomic nuclei are made up of protons and neutrons and possess an intrinsic quantum mechanical property called spin, which corresponds to the angular momentum $\boldsymbol{L}$ of the nuclei. This angular momentum $\boldsymbol{L}$ is quantized in both magnitude and direction as can be seen in [20]:

$$|\boldsymbol{L}| = \hbar \sqrt{I(I+1)} \qquad I = 0, \frac{1}{2}, 1, \frac{3}{2}, \dots. \tag{1}$$

$$L_z = m_l \cdot \hbar \qquad m_l = -I, -I+1, \dots, I-1, I, \tag{2}$$

with $\boldsymbol{I}$ being the spin quantum number, which can take either positive integer or half-integer values. The hydrogen atom possesses a spin of $I = \frac{1}{2}$, as it is comprised of a single proton. L_z denotes the projection of the angular momentum onto the z-axis, m_l is the corresponding magnetic quantum number, and $\hbar$ is the Planck constant ($h = 6.62607015 \cdot 10^{-34} \ [J\,s]$) divided by 2π. The spin of the hydrogen atom induces a magnetic moment proportional to the spin itself [18, p. 26]:

$$\boldsymbol{\mu} = \gamma \cdot \boldsymbol{L}. \tag{3}$$

The proportionality constant γ is called the gyromagnetic ratio, and depends on the specific nuclei, for hydrogen the gyromagnetic ratio is $\gamma = 42.58$ MHz/T.

When no external magnetic field is applied, the spins of the hydrogen atoms point in all directions indiscriminately. If, however, a strong magnetic field $\boldsymbol{B_o}$ is introduced, the spins of the hydrogen atoms tend to align themselves either parallel or antiparallel to the external field $\boldsymbol{B_o}$. For hydrogen atoms with $I = \frac{1}{2}$, this corresponds to the two eigenstates $m_l = \frac{1}{2}$ (spin up) and $m_l = -\frac{1}{2}$ (spin down). The discrete energy levels of the two eigenstates can be calculate with [20]:

$$E_{m_l} = -\hbar \, \gamma \, m_l \, |\boldsymbol{B_o}|. \tag{4}$$

In the case of spin up ($m_l = \frac{1}{2}$), the spins align parallel to the external magnetic field $\boldsymbol{B_o}$ and the energy decreases, while for spin down ($m_l = -\frac{1}{2}$) the spins align antiparallel to $\boldsymbol{B_o}$ and the energy increases. This is referred to as Zeeman splitting and the energy difference between the two states is given as [22]:

$$\Delta E = \hbar \, \gamma \, |\boldsymbol{B_o}| = \hbar \, \omega. \tag{5}$$

As can be seen, the energy difference is proportional to the applied external magnet field. A transition between these two energy states can be induced by photons with frequency ω_o such that:

$$\omega_0 = \gamma \, |\boldsymbol{B_o}|. \tag{6}$$

The Larmor frequency ω_o [19, p. 24] corresponds to the frequency with which the spins precess around the external magnetic field $\boldsymbol{B_o}$.

Since lower energy states are more favourable, a given ensemble of spins will align primarily in the direction parallel to $\boldsymbol{B_o}$. This in turn creates a net magnetization $\boldsymbol{M_0}$ which only consists of a longitudinal component (along the z-axis), and is consequently referred to as the longitudinal magnetization at the thermal equilibrium.

2.1.2 Radiofrequency Pulse

The radiofrequency pulse is essentially an electromagnetic field in the $\boldsymbol{B_1}$ direction, perpendicular to $\boldsymbol{B_o}$ [22]. By applying a short RF pulse with a frequency closely matching the Larmor frequency (in the case of hydrogen 42.58 MHz/Tesla), spins can be resonated, which lets them absorb energy from the radiofrequency pulse. This allows the spins to transition from the lower energy state to the higher energy state, which consequently tips the net magnetization into the xy-plane. This magnetization, which is perpendicular to the longitudinal magnetization along the z-axis $\boldsymbol{M_z}$, is called the transverse magnetization $\boldsymbol{M_{xy}}$.

The degree by which the magnetization is tipped into the xy-plane is referred to as the flip angle α [19, p. 36], which as can be seen,

$$\alpha = \gamma \, B_1 \, T \tag{7}$$

is proportional to the gyromagnetic ratio of the tissue in question, as well as the field strength of the RF pulse and the duration of the pulse, which equates to its pulse width. A flip angle of $\alpha = 90°$ describes a state in which the total net magnetization has been tipped from the longitudinal direction (z-axis) into the transverse plane (xy). Commonly used RF pulses include the previously mentioned 90° pulse, and the 180° pulse, which inverts the original longitudinal magnetization $\boldsymbol{M_0}$.

The transverse magnetization M_{xy} precesses around the z-axis, in direction of the external magnetic field B_o, with the Larmor frequency ω_0. This rotating transverse magnetization is what ultimately creates the MR signal, by inducing a small, measurable, voltage in the receiver coils [22]. This signal is called the free induction decay (FID).

2.1.3 Relaxation

After the radiofrequency pulse ends, the spins in the higher energy state, which cause the transverse magnetization, gradually return towards the thermal equilibrium by exchange of energy with their surroundings and due to dephasing of the spins. The thermal equilibrium being the initial state before the RF pulse, where the spins were aligned parallel and antiparallel to the external magnetic field B_o, and the net magnetization consisted of solely a component along the z-axis M_0[20].

This process is referred to as relaxation and consists of two separate mechanisms, the first of which being longitudinal relaxation, also commonly called T_1 relaxation or spin-lattice relaxation. T_1 relaxation describes the fact that the net magnetization along the z-axis M_z, which is zero right after a 90° RF pulse, increases exponentially with time until it has reached the longitudinal magnetization at the equilibrium M_0. This effect is due to the interaction between the higher energy spins and the surrounding lattice, causing them to exchange energy and return to the lower energy state. This can be appreciated from:

$$M_z(t) = M_o \left(1 - e^{-\frac{t}{T_1}}\right).$$

(8)

With the time constant T_1 being defined as the point in time at which the longitudinal magnetization has reached 63% of the equilibrium magnetization M_0.

The second relaxation phenomenon is the so-called T_2 decay (spin-spin relaxation, or transverse relaxation). Immediately after the RF pulse, the excited spins are in a state called coherent phase [20], meaning that they all share the same phase of 0°. From then on, the coherence of the spins is lost due to dephasing of the individual spins. This effect is caused by stochastic interactions between neighbouring spins [24] and consequently decreases the transverse magnetization M_{xy}. The T_2 time constant is defined as the time by which the transverse magnetization has decreased to 37% of its original value. In an ideal external magnetic field, this T_2 decay would be solely responsible for the decrease in transverse magnetization. Local field inhomogeneities, caused for example by the susceptibility differences of various tissues, or technical limitations in shimming of the B_o field, lead to additional dephasing of the spins. This issue is addressed by a second, inhomogeneity time constant T_2'. The effective decay time constant T_2^* is hence comprised of the time constants of both aforementioned effects and is defined as [19, p. 581]:

$$\frac{1}{T_2^*} = \frac{1}{T_2} + \frac{1}{T_2'}$$

(9)

The corresponding decrease in transverse magnetization M_{xy} as a function of time is therefore given as:

$$M_{xy}(t) = M_{xy}(0)\, e^{-\frac{t}{T_2^*}}.$$

(10)

In general, the longitudinal relaxation time T_1 is considerably higher than the transverse relaxation time T_2, which by definition is larger than the effective transverse decay time T_2^*.
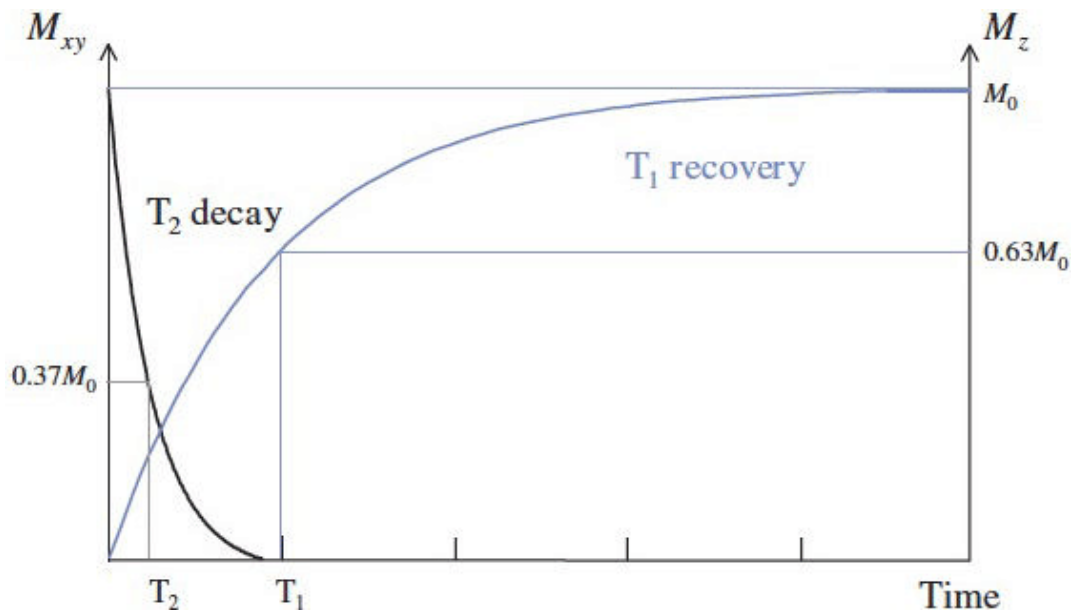
Figure 1. Longitudinal relaxation (T_1 recovery, spin-lattice relaxation) and transverse relaxation (T_2 decay, spin-spin relaxation) plotted as a function of time. The corresponding T_1 and T_2 time constants are marked on the time axis. Reproduced from [20].

This relation is clearly visible in Figure 1, where both the longitudinal relaxation and its T_1 time constant, as well as the transverse decay and its corresponding T_2 time are plotted as a function of time.

2.1.4 Magnetic Resonance Imaging

In the previous chapters, it was discussed how an ensemble of spins aligns along an external magnetic field B_o, and how this leads to a net magnetization M_0 (in the z-direction). We then saw how this longitudinal magnetization can be tipped into the transverse plane by the use of a radiofrequency pulse, and how this creates the measurable MR signal. Lastly, it was described through which relaxation processes the spins then return to the thermal equilibrium, and the signal decays.

The created signal, by itself, is not sufficient to create meaningful magnetic resonance images, as the information about where exactly the signal is coming from is still unknown. In the following chapters it will be explained which hardware components make up the MR scanner and how the MR signal can be spatially encoded through the use of gradient fields in the x-, y- and z-directions, namely the frequency encoding, phase encoding and slice selection.

2.1.4.1 MRI hardware

The scanner itself consists of multiple hardware components, which all serve a specific purpose. The main magnet, which is usually superconducting and therefore needs to be cooled by liquid helium, creates the static magnetic field B_o along the z-axis. Gradient coils produce ideally linear magnetic fields in the x-, y- and z-directions to allow for the spatial encoding to take place. In Figure 2 the gradient coils and the main magnet Helmholtz coils are shown. The z-gradient coil has a similar form to the Helmholtz coils, while the x- and y-gradient coils have a more complex, saddle like shape to allow for the creation of homogenous magnetic fields in these directions.
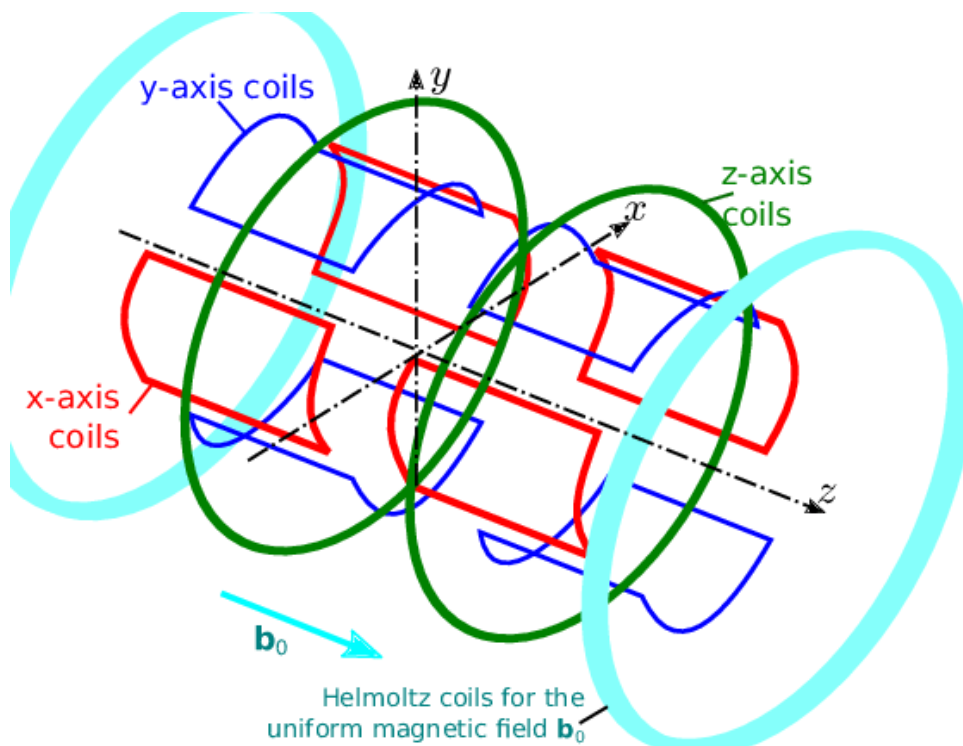
Figure 2: Visualization of the shape and location of the x-, y- and z-gradient coils, as well as the main magnet coils creating the static magnetic field. Reproduced from [25]

For the spatial encoding to take place, the gradient coils need to be rapidly switched on or off at times, which leads to the audible noise in the scanner. Transmit RF coils are used to tip the magnetization into the xy-plane by a certain angle, as described in Chapter 2.1.2, creating the signal, which is then received by the receive RF coils. If present in the scanner, body coils are commonly used as transmit coils, while receive coils are usually much closer to the measured subject, in the form of for example head or knee coils, as the lower distance increases the signal-to-noise ratio (SNR). The gradients and RF pulses are controlled by the scanner computer, depending on the used sequence.

2.1.4.2   Slice Selection

By applying a magnetic field gradient G_z along the z-axis, in the direction of the static magnetic field B_o, the precession frequency of the spins can be made spatially dependant on their location along the z-axis. This is due to the Larmor frequency being directly proportional to the magnetic field strength, as seen in Eq. (6). Only spins for which their precession frequency matches the frequency of the RF pulse get excited, meaning that a specific slice along the z-axis (Δz) can be selected by choosing the appropriate values of the magnetic field gradient G_z, as well as the bandwidth of the radiofrequency pulse $\Delta \omega_{RF}$. This relation is given as [21, p. 18]:

$$\Delta \omega_{RF} = \gamma \, G_z \, \Delta z. \tag{11}$$

A visual representation of the slice selection and the corresponding gradient an RF pulse is shown in Figure 3.
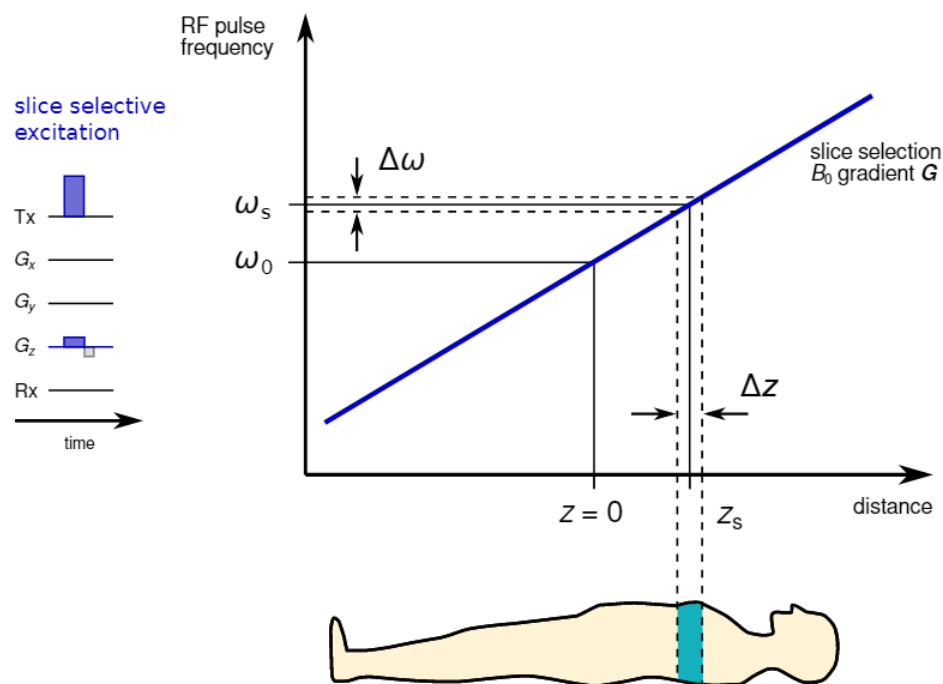
Figure 3: Schematic image of slice selection through a gradient G_z, applied in the z-direction during the RF pulse. The relation between the pulse bandwidth $\Delta \omega$ and the slice thickness Δz is shown. Reproduced from [22, , p. 45].

The slice selection gradient G_z is applied at the same time as the RF pulse. Slice thickness can be adjusted either by varying the gradient strength or the RF pulse bandwidth. Higher gradients and smaller bandwidths lead to thinner slices, while low gradient strengths and broad RF pulses create thicker slices. The position of the slice can be selected by adjusting the frequency of the RF pulse for a given gradient strength and pulse bandwidth.

2.1.4.3   Frequency Encoding

Similar to the slice selection gradient along the z-axis, frequency encoding relies on a linear magnetic field gradient G_x to make the precession frequency of the spin ensembles dependant on their location along the x-axis. This change in frequency at a given point x at time t is [21, p. 144]:

$$\omega(x,t) = \omega_0 + \omega_G(x,t). \tag{12}$$

Here ω_0 denotes the Larmor frequency and $\omega_G(x,t)$ is the corresponding deviation

$$\omega_G(x,t) = \gamma\, x\, G(t), \tag{13}$$

which is linear in its position x and gradient $G(t)$. Based on this spatially dependant frequency change, an inverse Fourier transformation can then be applied to the measured MR signal to give us the corresponding frequency spectrum, which contains information about the spin density at any given frequency [19, p. 243]. The spin density can therefore be interpreted as a projection of the measured object onto the x-axis.
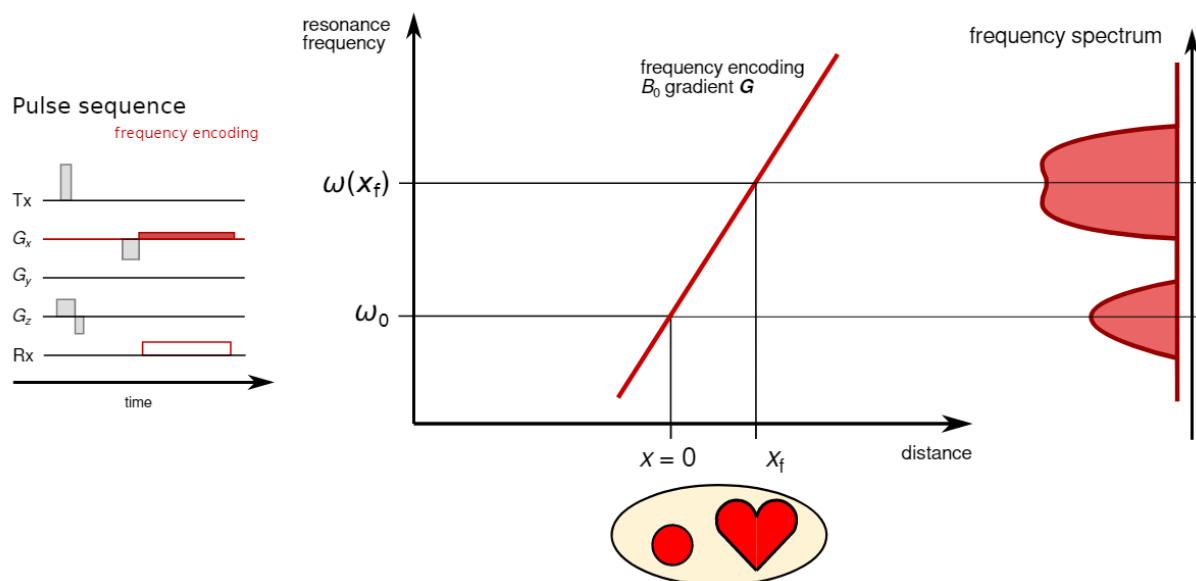
Figure 4: Schematic image of the frequency encoding gradient G_x, applied during readout R_x, the measured objects on the bottom and the resulting frequency spectrum to the right. The pulse sequence also shows the previously mentioned RF pulse during T_x, and the slice selection gradient G_z. Reproduced from [22, p. 56].

An example of how such a frequency spectrum would look for two given objects is shown in Figure 4. Not only is it possible to resolve the two distinct objects along the x-axis, but we can also determine the amount of signal each object generates based on the magnitude of the signal at each frequency. As a consequence of the applied gradient, phase begins to accumulate over time [21, p. 145]

$$\phi_G(x,t) = -\gamma\, x\, \int_0^t dt'\, G(t'), \tag{14}$$

10

which means that the spins begin to dephase, leading to a decrease in transverse magnetization. To counteract this, a dephasing gradient, which can be seen in Figure 4, is applied prior to the actual frequency gradient itself. It is equal in area to half of the frequency gradient's and therefore allows for the maximum amount of transverse magnetization (phase coherence) to be measured at the time of the echo.

2.1.4.4 Phase Encoding

The last direction which needs to be spatially encoded is along the y-axis, and is done so by the use of what is called phase encoding. This step happens between slice selection and the frequency encoding. A magnetic field gradient G_y is applied with a given strength during a window of time where the magnetization is in the transverse plane [19, p. 256]. This creates spatial variation of the phase of the spins along the y-direction, since the phase encoding gradient G_y causes the spins to dephase in varying degrees based on their location along the y-axis. An example of how this dephasing would look like for a spin ensemble, prior to the application of the frequency encoding gradient, is shown in Figure 5.
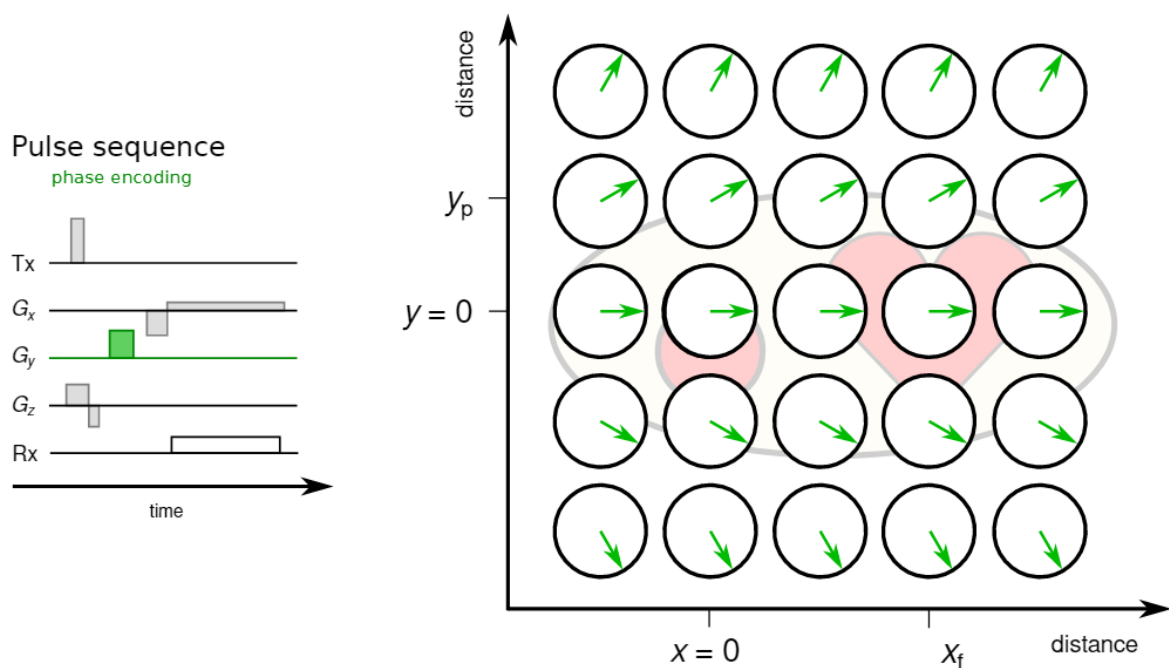
Figure 5: Schematic image of how a phase encoding gradient G_y causes dephasing of a spin ensemble in relation to the location of the individual spins along the y-axis. RF pulse T_x, frequency encoding gradient G_x during the readout Rx and slice selection gradient G_z are shown in the pulse sequence diagram. Reproduced from [22, p. 68].

This sequence is then repeated a certain number of times, called the number of phase encoding steps, with different gradient strengths. Since only one phase encoding step can be measured during each repetition time, phase encoding is very time consuming. After the measured signal has been spatially encoded in all directions and was measured, the image can then be reconstructed by applying a Fourier transformation.

2.1.5 K-space

Once a slice has been selected along the z-axis and the spins within it have been spatially encoded using frequency encoding gradients and phase encoding gradients, the resulting phase at a point in space $\boldsymbol{r}(x,y)$ at a time t, can be written as [22, p. 81]:

$$\phi(\boldsymbol{r},t) = \gamma\,\boldsymbol{r}\,\int_0^t \boldsymbol{G}(t')dt'. \tag{15}$$

Given that relaxation effects are ignored for the sake of simplicity, the time dependant transverse magnetization $\boldsymbol{M_{xy}}(t)$, can be denoted as

$$M_{xy}(t) = \int_{-\infty}^{+\infty} \boldsymbol{M_o}(\boldsymbol{r})\,e^{i\gamma\int_0^t \boldsymbol{r}\,\boldsymbol{G}(t')dt'}\,d\boldsymbol{r}, \tag{16}$$

where $\boldsymbol{M_o}(\boldsymbol{r})$ is the spin density at a given point $\boldsymbol{r}$. By introducing a spatial frequency variable $\boldsymbol{k}$(t) [22, p. 153] commonly referred to as the k-space vector

$$\boldsymbol{k}(\text{t}) = \gamma\int_0^t \boldsymbol{G}(t')dt', \tag{17}$$

The transverse magnetization can be written as a function of $\boldsymbol{k}(t)$, and simplified to [22, p. 81]:

$$M_{xy}\big(\boldsymbol{k}(\text{t})\big) = \int_{-\infty}^{+\infty} \boldsymbol{M_o}(\boldsymbol{r})\,e^{i\,\boldsymbol{k}(t)\boldsymbol{r}}\,d\boldsymbol{r}. \tag{18}$$

As can be appreciated from Eq. (18), the transverse magnetization can be interpreted as an inverse Fourier transformation of $\boldsymbol{M_o}(\boldsymbol{r})$, and the measured MR signal is proportional to $\boldsymbol{M_{xy}}(t)$. The transverse magnetization values for different k-space vectors, which correspond to specific frequency- and phase encoding gradients, are stored in a data matrix called k-space. It contains the raw data measured at the MR scanner prior to any reconstruction, from which the image can then be reconstructed through the Fourier transformation.

The x-axis of k-space relates to the spatial frequencies ranging from the lowest frequency encoding gradient $-k_{f,max}$ to its highest value $+k_{f,max}$. Contrary to that, y-axis corresponds to the strength of the applied phase encoding gradient, ranging from $-k_{p,max}$ to $+k_{p,max}$. The points in k-space can be acquired with various so-called sampling patterns by adjusting the frequency- and phase encoding gradients, with the most commonly used sampling pattern being Cartesian. For Cartesian sampling, one line of k-space is acquired per repetition time TR. After the RF pulse and slice selection gradient, a specific phase encoding gradient is applied, as described in Chapter 2.1.4.4, which relates to a value on the y-axis of k-space. Next the frequency encoding gradient is switched on, and the data points in k-space along this line are measured during the so-called data acquisition period. This sequence is then repeated until all desired phase encoding steps are acquired, and k-space is fully sampled.

Each point in k-space contains information about the entire image, at a given combination of frequency- and phase encoding gradients. Lower spatial frequencies, which make up the

centre of k-space, correlate to smaller frequency- and phase encoding gradients. This in turn means that the corresponding spins experience a lower degree of dephasing and therefore create more signal. This means that the centre of k-space is primarily responsible for the signal and contrast of the reconstructed image, as is visualized in Figure 6 marked by (B).
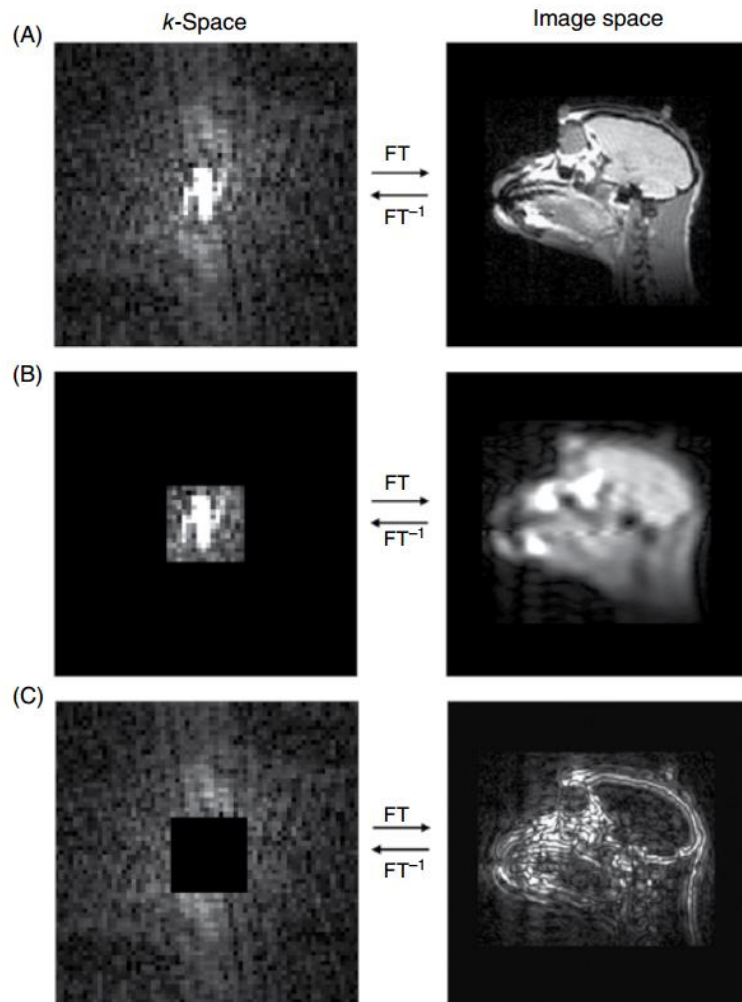

Figure 6: Schematic image of the impact certain regions of k-space have on the image. A) Shows the image for a fully sampled k-space, B) shows that the centre of the image relates to signal and contrast, while in C) the relation of the edges of k-space to the sharpness of the image is visualized. Reproduced from [29].

In comparison to that, the outer edges of k-space, which are made up of the higher spatial frequencies, contain information about the spins experiencing stronger dephasing. While they naturally contribute less signal, they are essential for the edge definition and sharpness of the image [8], as seen in (C).

A number of so-called parallel imaging methods have been developed in order to speed up the process of k-space acquisition. They allow for k-space to be undersampled according to pre-defined patterns and therefore reduce scan times. Two such acceleration methods, GRAPPA and CAIPIRINHA, will be explained in more detail in Chapters 2.2.2 and 2.2.3.

2.1.6   Gradient-recalled Echo Sequence (GRE)

The gradient-recalled echo (GRE) sequence uses opposing gradients (instead of a 180° pulse as in spin-echo) to dephase the FID signal generated by the RF pulse, and then subsequently rephase it again to create the echo. A typical 2D gradient echo pulse sequence is shown in Figure 7. As explained in Chapter 2.1.2, an RF pulse flips the longitudinal magnetization into the transverse plane by a certain flip angle, here written as θ, which creates the measurable FID signal. At the same time a slice selection gradient, as mentioned in Chapter 2.1.4.2, is used to excite a specific slice along the z-axis, and the dephasing caused by the slice selection gradient is reverted by the refocusing gradient (negative portion of slice selection gradient).
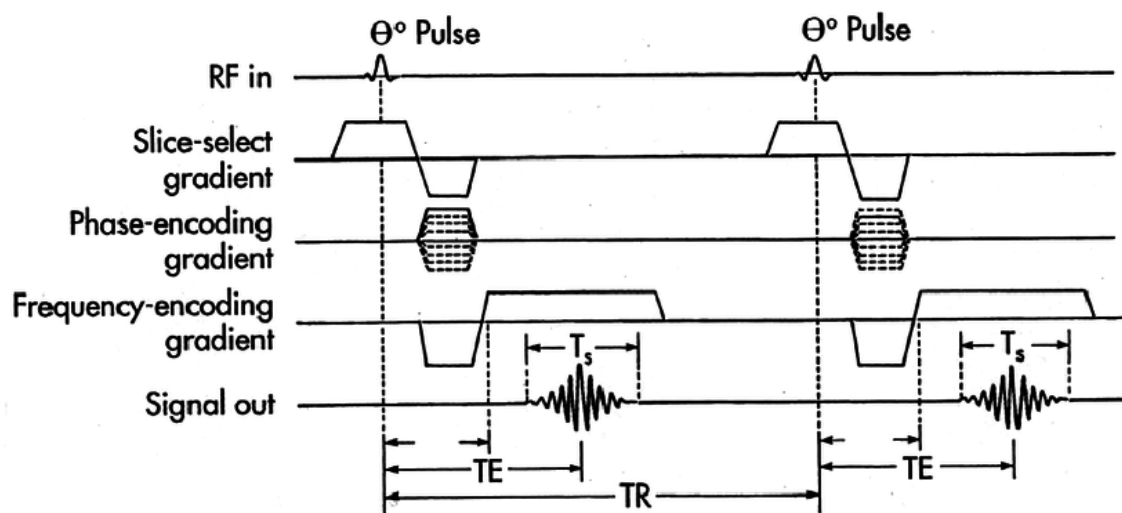
Figure 7: Image of a 2D gradient-recalled echo pulse sequence. From top to bottom: radiofrequency pulse (RF), the slice selection gradient (z-axis), phase-encoding gradient (y-axis), frequency encoding gradient (x-axis), the generated signal (Signal out), echo time TE and repetition time TR. The time axis goes from left to right. Reproduced from [30].

The phase encoding gradient, as described in Chapter 2.1.4.4, is used to dephase the spins by a varying degree depending on their position along the y-axis. In terms of k-space, each phase encoding step relates to a specific k_y coordinate. The frequency encoding gradient, as stated in 2.1.4.3, is comprised of a negative component which dephases the spins, followed by an opposing gradient which begins to rephase them again. Once phase coherence of the spins is reached, the echo is created. Since there is no 180° refocussing pulse, as is the case in spin echo, the obtained images are T_2^* weighted. The time it takes between the RF pulse is applied and the echo is generated, is referred to as the echo time (TE). After the echo, the frequency encoding gradient once again dephases the spins. In k-space the dephasing gradient is used to move to $-k_{x,max}$. The rephrasing gradient then traverses k-space along the k_x direction, sampling each data point in between, up to $k_{x,max}$. This sequence is then repeated until all desired k-space lines are acquired for a given slice, with the time between each RF pulse being called the repetition time TR. Once the two-dimensional k-space matrix of a slice is fully

14

sampled, the frequency of the RF pulse is adjusted to select the next slice, and the entire process is repeated. This continues until the entire three-dimensional k-space matrix is acquired.

Besides the above described 2D gradient echo sequence, where the spatial encoding along the z-axis is performed by the use of the slice selection gradient, GRE also allows for volumetric imaging where a whole 3D volume is excited during each (TR). This 3D volume, also commonly called a slab, is then spatially encoded through the use of an additional phase encoding direction along the z-axis [19, p. 424].

A considerable benefit of the of the gradient-recalled echo sequence is that the same process of creating a single echo, through the opposing gradients, can be repeated a number of times to acquire multiple echoes during the same repetition time TR. An example of this is shown in Figure 8, where three echoes are generated by repeatedly applying opposing dephasing (De) and rephasing (Re) gradients. As can be seen, the signal measured by the individual echoes follows the T_2^* decay curve, decreasing significantly over time. This means that there is a limit to the maximum number of echoes that can be generated, which depends on the echo time TE and the type of tissue measured. Typically, between 3-6 echoes can be acquired before the signal is lost due to the T_2^* decay.
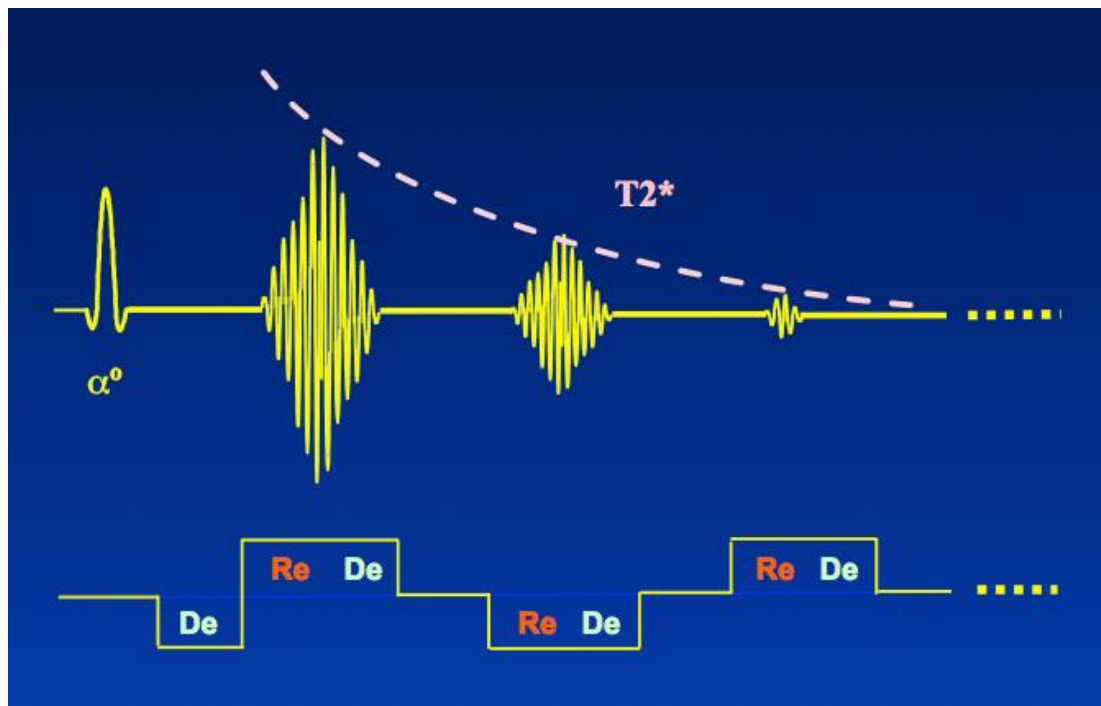
Figure 8: Schematic Image of how multiple echoes can be generated from a single RF pulse (with a flip angle α) by repeatedly applying opposing dephasing (De) and rephasing (Re) gradients. The measured signal of the echoes follows the T_2^* decay. Reproduced from [31].

Other advantages of the gradient echo sequence are that the use of small flip angles, and it being T_2^* weighted, which is considerably shorter compared to T_2, allows for shorter echo times TE and consequently shorter repetition times TR. Small flip angles are particularly useful at ultra-high-field strengths, since higher frequency RF pulses are problematic in terms

15

of the specific absorption rate (SAR). Smaller flip angles, as seen in Eq. (7), require shorter RF pulses, which consequently reduces the amount of absorbed energy in the subject.

The optimal flip angle, which yields the strongest signal in the case of volumetric imaging (3D) is referred to as the Ernst angle and is given by [23, p. 430]:

$$\theta_E = arccos\big(e^{-TR/T_1}\big).$$

(19)

The T_2^* weighting is also what allows the GRE sequence to be used in conjunction with SWI and QSM [32]. GRE sequences are therefore able to acquire high resolution images in relatively short acquisition times, and provide the user high versatility in the types of contrasts that can be generated.

The volumetric interpolated breath-hold examination (VIBE) sequence, from here on only referred to as the VIBE sequence, is a 3D gradient-recalled echo sequence developed by Siemens. As the name suggests, the primary application of this sequence is the imaging of the breast and abdominal region, with a focus on what is called breath-hold examinations. The respiratory cycle causes a high degree of movement of the chest region, leading to movement artifacts in the acquired scans, which in turn greatly diminishes the image quality and diagnostic usability. To prevent this effect, breath-hold examinations require the patients to inhale and then hold this position for an extended period of time, commonly up to 30 seconds, while a short scan is acquired during this time window [18]. After letting the patient exhale again and waiting for their breath to recover, this process is then repeated.

Since the acquisition times for breath-hold examinations are limited to such a short period of time, the need for state-of-the-art acceleration methods is evident. Therefore, Siemens implemented the CAIPIRINHA (Controlled Aliasing in Parallel Imaging Results in Higher Acceleration) [11] method into the VIBE sequence. CAIPIRINHA is a more recently developed acceleration method based on GRAPPA (GeneRalized Autocalibrating Partially Parallel Acquisitions) [10], and both methods will be described in more detail in the following chapters. Through the use of CAIPIRINHA acceleration, the VIBE sequence offers a great degree of flexibility in choosing the desired undersampling patterns. It is therefore hypothesized that the VIBE sequence should be able to reduce acquisition times of breast, abdominal and brain imaging [33].

2.2 Parallel Imaging Techniques

Parallel imaging (PI) is a group of techniques developed to reduce image acquisition time by reducing the number of phase encoding steps, which are time consuming, and replacing the missing information with data acquired by a RF coil array [21, p. 859]. The name is derived from the fact that multiple detectors are used in parallel to measure the RF data

16

simultaneously. It also often referred to as replacing the Fourier encoding with sensitivity encoding.

The resulting acceleration of the data acquisition has a multitude of benefits, the most obvious one being that it allows for substantially shorter scans at higher resolutions than would have been possible otherwise. The decrease in acquisition time not only increases the comfort for the patients, but also makes it possible to more efficiently use a given MRI scanner in a clinical setting. Applications like breath-hold examinations of the breast and abdominal region, are especially prone to movement artifacts, which appear in the reconstructed image as blurring. There are also a number of diseases, such as ADHD (attention deficit hyperactivity disorder), schizophrenia and ASD (autism spectrum disorder), that make it particularly difficult for patients to remain still for extended periods of time [5]. For these mentioned examples, reducing the scan times through parallel imaging can have a drastic increase in SNR by reducing the effect movement artifacts have on the image. It is important to note that parallel imaging is not without drawbacks, most importantly it can introduce aliasing in the reconstructed images [7].

In the following two chapters, the parallel imaging techniques GRAPPA (GeneRalized Autocalibrating Partially Parallel Acquisitions) and CAIPIRINHA (Controlled Aliasing in Parallel Imaging Results in Higher Acceleration) will be described in detail. Both GRAPPA and CAIPI, in contrast to their predecessor method SENSE (SENSitivity Encoding) [34], operate in k-space [21, p. 873]. In this method, k-space is undersampled according to a specific pattern, and the missing data points are then reconstructed based on the coil sensitivities of a RF coil array.
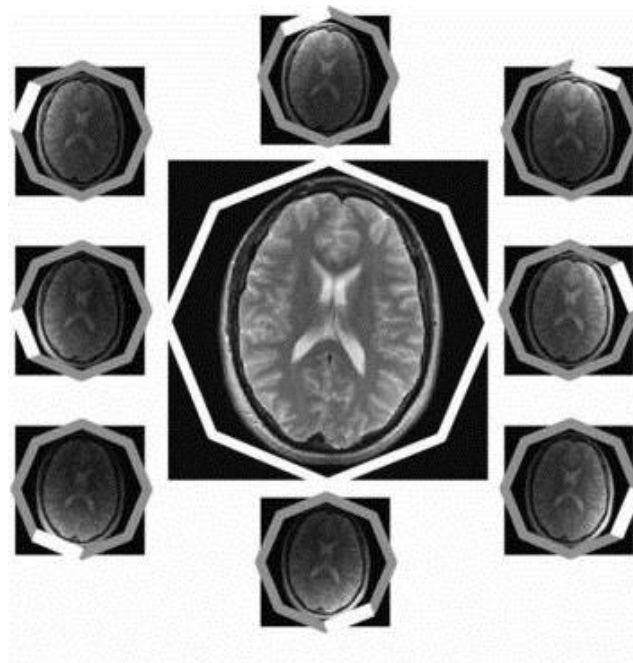
Figure 9: Example of a head coil array with 8 individual RF coils, arranged in a circle around the to be measured object. The location and reconstructed image of the measured signal of each independent coil is shown, as well as the combined image in the middle. Reproduced from [7].

An example of such an RF coil array is shown in Figure 9, with 8 separate coils being arranged in a circle around an object, in this case a brain. While each coil measures the object in its entirety, the signal the strongest in close proximity to the specific coil. This is referred to as the coil sensitivity and needs to be accounted for in parallel imaging. Figure 10 shows how pixels in the measured single coil image relate to their corresponding locations in the object by multiplication with the coil sensitivity profile.
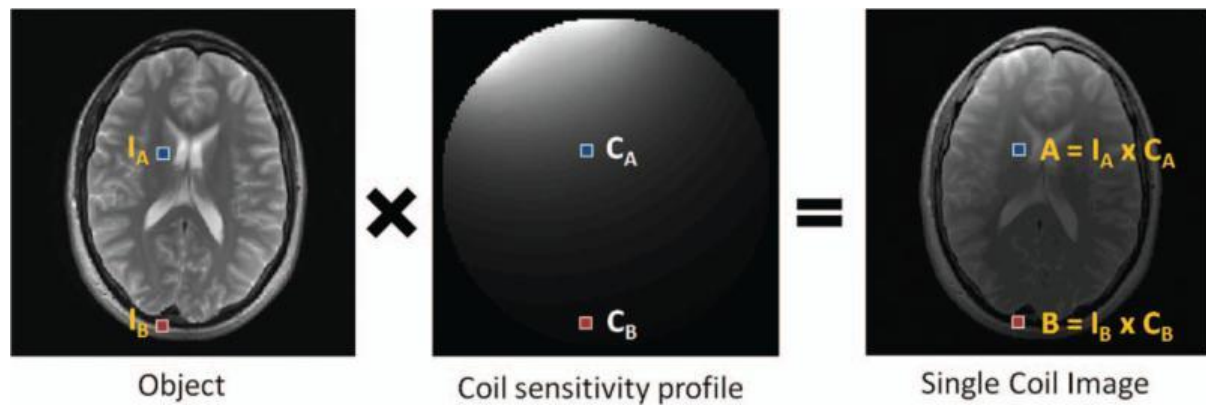
Figure 10: The pixels I_A and I_B of the measured object are multiplied (weighted) by the corresponding coil sensitivities C_A and C_B to obtain the pixels A and B in the single coil image. Reproduced from [7].

2.2.1 Signal-to-noise ratio (SNR)

The signal-to-noise ratio is a measure of image quality, and allows for the performance of MRI systems, different sequences, acceleration methods to be quantified [35]. It describes the relation between the measured signal and the background noise.

Various methods have been developed in order to accurately measure the SNR of an image, the most commonly used one being the two-region approach. It involves selecting two distinct regions of interest (ROI) inside one image. The first ROI is selected inside the tissue one wants to image, and is used to determine the mean intensity of the signal. The second ROI is selected from the background of the image, ideally from a region without any signal, for example air surrounding the object [36]. This ROI is used to determine the standard deviation of the background noise which is assumed to be uniformly distributed throughout the image. The main advantage of this method is that the SNR can be determined from a single image. The drawback, though, is that any non-uniform distributions of noise, such as ghosting in the background ROI, can significantly affect the calculated SNR value. In order for the two-region SNR approach to be valid, the noise distribution has to be spatially homogenous across the entirety of the image [35]. Furthermore, the statistical distribution of the background noise should be known in order to accurately determine the noise superimposed over the measured tissue. These conditions are not generally satisfied in the case of images acquired with the use of parallel imaging. The noise distribution in parallel imaging greatly depends on factors such as the coil geometry and the acceleration factor. This effect is described in the geometry (g)-factor [37]. The SNR of a parallel imaging method with a given acceleration factor *R* and g-factor *g* equates to [38]:

$$SNR_{PI} = \frac{SNR_{Full}}{g\,\sqrt{R}}. \tag{20}$$

In order to more accurately determine the SNR of accelerated images, an alternative to the two-region approach was developed, the so-called difference method [35]. Two images with identical scan parameters are acquired subsequently, and sum and difference images of the two acquisitions are generated. The mean signal of the sum image m_{sum}, and the standard deviation of the difference image s_{diff} are then calculated from the same ROI. The SNR is then given as [35]:

$$SNR_{diff} = \frac{\frac{m_{sum}}{2}}{\frac{s_{diff}}{\sqrt{2}}} = \frac{1}{\sqrt{2}}\frac{m_{sum}}{s_{diff}}. \tag{21}$$

Assuming that the noise of each image is statistically independent, the SNR is proportional to the square root of the number of acquisitions [21, p. 331]. This effect is compensated by dividing by $\sqrt{2}$ in Eq. (21). The signal-to-noise ratio in general scales linearly with the voxel volume and proportional to the square root of the acquisition time TA, according to [19, p. 428]:

$$SNR \propto \Delta x\,\Delta y\,\Delta z\,\sqrt{TA}. \tag{22}$$

To compare the signal-to-noise ratio of various sequences and acceleration methods with differences in scan times, the SNR efficiency is defined as [39]:

$$\eta = \frac{SNR}{\sqrt{TA}}. \tag{23}$$

It compensates for the fact that scans with longer acquisition times have an inherently higher SNR as seen in Eq. (22).

2.2.2 GeneRalized Autocalibrating Partially Parallel Acquisitions (GRAPPA)

GRAPPA (GeneRalized Autocalibrating Partially Parallel Acquisitions) [10] allows for the acceleration of the data acquisition by undersampling of k-space in a specific pattern. The missing information, namely the data points of the k-space lines that were skipped due to the undersampling, is then reconstructed based on the measured coil sensitivities and by utilizing the neighbouring k-space lines that were acquired. This allows for a reconstruction of full field of view (FOV) images of accelerated scans.

To achieve this, a small number of so-called autocalibration signal lines (ACS) are measured either separately or integrated into the main scan. The ACS lines make up a smaller sub region, most commonly in the centre of k-space, that is fully sampled.
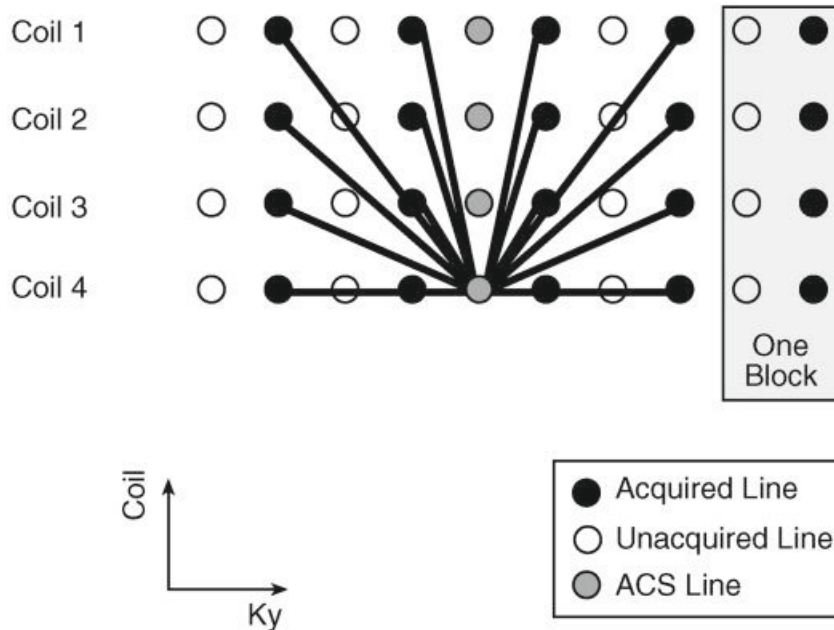
Figure 11: Schematic Image of the GRAPPA algorithm. Acquired lines are shown in black, not acquired lines in white and the ACS lines in the centre as grey. The visualized portion of k-space is measured through 4 RF coils. ACS lines are fitted with information from multiple neighbouring acquired k-space lines of multiple coils. The block consists of one acquired k-space line and the neighbouring skipped lines. Reproduced from [10].

As can be seen in Figure 11, a single ACS line is fitted through the sampled data of (in this case) four k-space lines, acquired by four individual coils. The ACS lines are what ultimately allows the missing data points to be reconstructed by determining the so-called GRAPPA weights. To calculate these weights, the GRAPPA kernel is introduced, which describes the number and pattern of source points used in the reconstruction [7]. By moving the GRAPPA kernel through both the ACS region and the corresponding area in the undersampled k-space matrix measured by the individual coils, the GRAPPA weights can be calculated. Increasing the number of ACS reference lines can lead to more accurate GRAPPA weights, but correlates with longer acquisition times.

An example of this sliding kernel approach is depicted in Figure 12, for an acceleration factor of R=3. The weights w are calculated by multiplying the target matrix S_{trg} with the Moore-Penrose pseudoinverse of the source matrix S_{src}. This pseudoinverse matrix, which solves the least-square problem of a linear system, can be used to invert the source matrix S_{src} even if this matrix is not square or its rows are not linearly independent. Applying the GRAPPA weights to the accelerated acquisition then allows for the calculation of the missing data points in k-space, based on the information obtained from the neighbouring measured k-space lines. Therefore, a fully sampled k-space matrix for each individual RF coil can be created. A Fourier transformation is then applied to the k-space of each coil in the array to attain the single coil images, and the final image is then generated by combining all the individual images of the coil array. Advantages of GRAPPA are that it is a very robust method even for regions with low signal or scans affected by a moderate amount of patient movement

[7]. It also allows for a considerable degree of freedom in choosing the undersampling pattern as well as the size of the ACS region, and the form of the GRAPPA kernel.
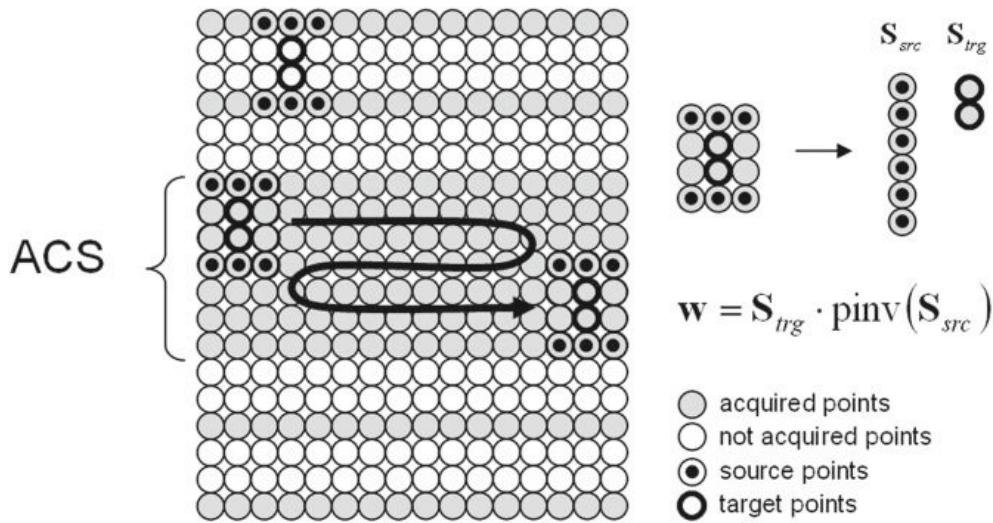
Figure 12: Schematic image of how GRAPPA weights are determined based on the acquired data points of the ACS reference lines, for an acceleration factor of R=3. To the right, the corresponding GRAPPA kernel is shown, as well as the source matrix S_{src} and the target matrix S_{trg}. Reproduced from [37].

2.2.3 Controlled Aliasing in Parallel Imaging Results in Higher Acceleration (CAIPIRINHA)

The CAIPIRINHA (Controlled Aliasing in Parallel Imaging Results in Higher Acceleration) [11] method is based on GRAPPA, and as the name suggests, already manipulates the aliasing artifacts during data acquisition. This is done through the reorder shift, the method's main distinct feature. This shift, as well as examples of the resulting undersampling patterns GRAPPA and CAIPIRINHA are shown in Figure 13.
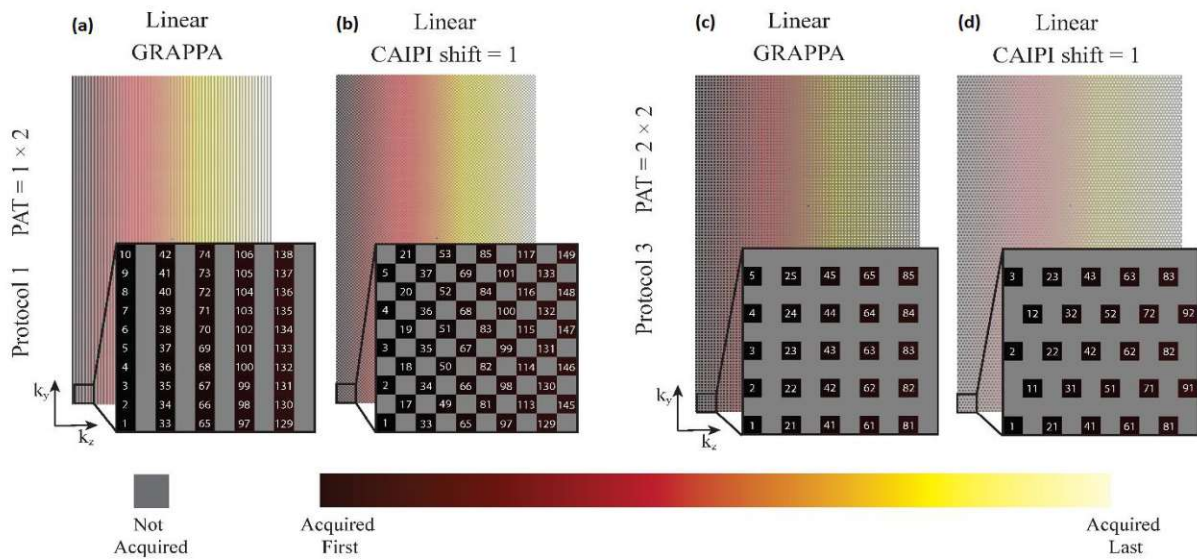
Figure 13: K-space sampling pattern visualized for GRAPPA 1×2 (a), CAIPI121 (b), GRAPPA 2×2 (c) and CAIPI221 (d). Acquired data points are depicted in black while not acquired points in k-space are shown in grey. The reorder shift of CAIPIRINHA can be seen in (b) and (d). Reproduced from [40].

In (a), the sampling pattern for GRAPPA 1×2 is visualized, with only every second k-space line in the k_z-direction being acquired. The corresponding CAIPI 121 pattern shifts every second k-space line by one additional data point, leading to the scheme seen in (b). By accelerating not only in the k_z-direction, but also along the second phase encoding direction ky, the sampling pattern for GRAPPA 2×2 (c) is produced. Once again, the CAIPI scheme is shifted by 1 point every second acquired k-space line due to the reorder shift of $\Delta k_z = 1$, seen in (d).

The idea behind the reorder shift, which is accomplished by additional phase encoding gradient offsets, is that the shift in the sampling pattern also shifts the aliasing, allowing for a more efficient use of the coil sensitivity variations of the RF coil array. The resulting modification of the aliasing is already performed during data acquisition, which consequently improves the conditions of the image reconstruction, leading to overall improved image quality [41].

An example of how this shifting of the aliasing looks like in practical terms is shown in Figure 14, where images with an acceleration factor of $R = 2$ in the partition (slice) direction, and their generated images in transversal- and sagittal view, are compared. The transversal image is masked in order to more clearly demonstrate the form and location of the aliasing artifacts (light grey) in relation to the measured object (central region with white border).
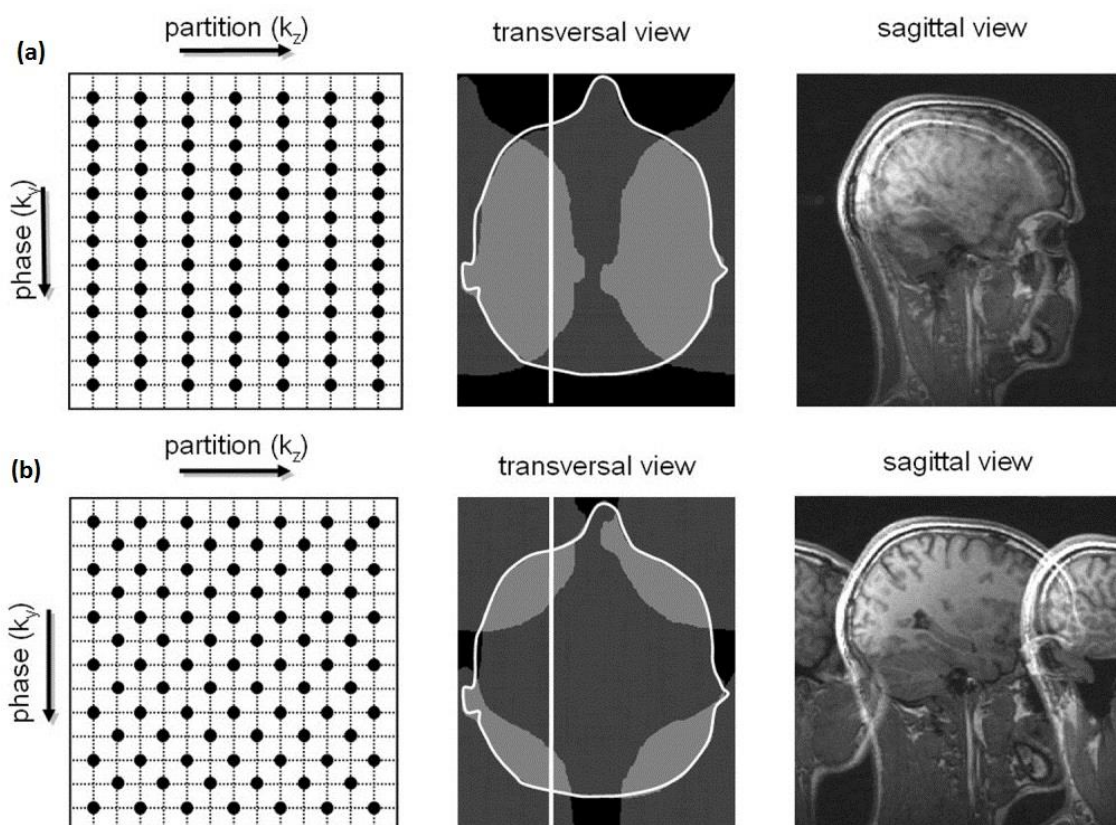
Figure 14: Undersampling patterns (left) as well as the corresponding masked transversal view (middle) are shown in order to demonstrate the aliasing conditions. A selected slice, marked by the vertical bar in the transversal view, is depicted in the sagittal view (right). Both images were acquired with an acceleration factor of R=2, image (a) is accelerated in the partition direction without a reorder shift and image (b) is accelerated in the phase encoding direction with a reorder shift of $\Delta k_z = 1$. Reproduced from [41].

The sampling pattern depicted as (a) in Figure 14 does not have a reorder shift (GRAPPA 1×2), and the resulting image shows aliasing along the partition direction (k_z). From the sagittal view it can be seen that the aliasing for superimposed partitions along the k_z-direction lies directly on top of each other.

In the undersampling pattern (b), a reorder shift of $\Delta k_z = 1$ is applied (CAIPI 221), which causes the aliasing to shift along the phase encoding direction k_y as well. This allows for the aliasing to be removed more efficiently during reconstruction, since the shift by FOV/2 better separates the aliasing artifacts from the image of the measured object, making it easier to remove the artifacts during reconstruction. Besides this effect, the separation caused by the reorder shift, observed in (b), allows for the coil sensitivities to be accurately determined, since they are not directly superimposed as is the case in (a).

The reorder shift in CAIPIRINHA grants the user additional freedom in choosing the undersampling pattern [42], especially at higher acceleration factors. With these patterns, more even k-space sampling can be achieved and the form of aliasing artifacts can be controlled during data acquisition. This means that, for any given application, an ideal sampling pattern can be found to allow for better image quality at higher acceleration factors by maximizing the efficiency of the coil sensitivity variations and minimizing the signal overlap of the measured data points in k-space [41].

The effect this reorder shift can have on the overall image quality can be observed in Figure 15, where the results published in the Magnetom Flash 1/2012 [43] article are shown.

GRAPPA 2x2   CAIPI 221
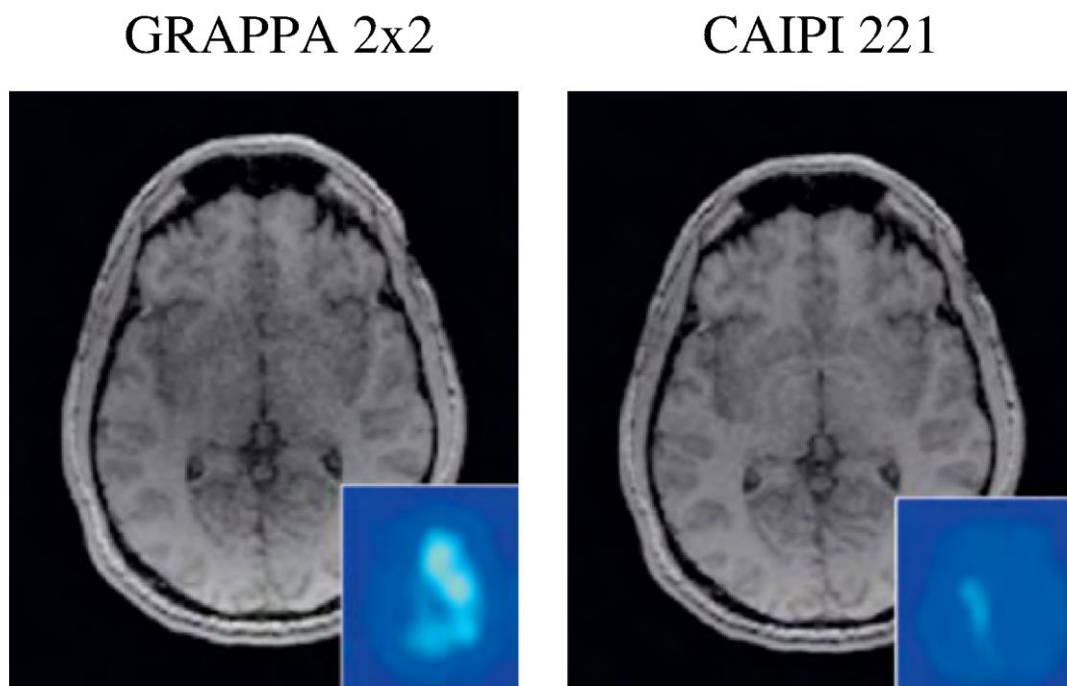
Figure 15: Comparison of magnitude images using GRAPPA 2×2 and CAIPI 221 acceleration. The corresponding g-factor maps are shown in the bottom right corner. A clearly visible reduction in noise can be observed in the CAIPI 221 image compared to GRAPPA 2×2. Reproduced from [43].

In this figure, single echo in-vivo scans acquired using GRAPPA 2×2 and CAIPI 221 acceleration are shown. A clear reduction in visible noise over the entire image can be seen, which is also apparent when looking at the g-factor maps in the bottom right corner of the GRAPPA 2×2 and CAIPI 221 images.

2.3   High- and Ultra-High Field Magnetic Resonance Imaging

In the development of MRI scanners, a trend exists towards increasing the static magnetic field strengths B_0, specifically 3T (high) and 7T (ultra-high). This is due to both SNR and tissue contrast scaling proportionally to the magnetic field strength [44]. While the signal increases quadratically with B_0, the noise unfortunately also increases linearly with the B_0-field [18, p. 10]. The resulting increase in SNR at higher fields should therefore be linear in theory. Empirically it has been shown that if physiological noise can be removed, a supralinear increase in SNR, roughly proportional to $B_0^{1.65}$ [9], can be achieved. The SNR increase at higher field strengths allows for higher resolution scans to be acquired during the same acquisition times compared to their lower field strength counterparts. Another way to utilize the increase in the signal-to-noise ratio at ultra-high fields is to reduce scan times while still retaining similar image quality, and therefore not impacting the diagnostic usability of the scans.

Relaxation times are also dependant on the external magnetic field strength, with longitudinal relaxation T_1 increasing according to B_0, while the effective transversal relaxation T_2^* decreases with B_0 [9]. This decrease in T_2^* is especially beneficial for T_2^*-weighted structural imaging, as the faster transversal decay speeds up the overall data acquisition. Combined with the already mentioned intrinsic increase in SNR and spatial resolution, this allows for structural imaging with previously unseen detail at a given TA. These improvements in resolution and detail have made it possible to more effectively detect lesions and accurately image smaller regions of interest, such as microbleeds, the amygdala or the hippocampus [44]. Other clinical applications include the diagnosis of brain tumours, smaller epileptic lesions and multiple sclerosis (MS) lesions, just to name a few. Besides structural imaging, the benefits of ultra-high field strengths are evident as well in magnetic resonance spectroscopy, since besides the enhanced SNR, the chemical shift dispersion also increases due to the stronger B_0 field. This allows for a more accurate detection and quantification of metabolites compared to lower field strengths.

The application of ultra-high fields is not without challenges, however, as the increase in the magnetic field strength also correlates to a rise in B_0 inhomogeneity. This inhomogeneity in the static magnetic field can lead to effects like signal loss or spatial distortions. Homogeneity is also decreased in the B_1 field of the RF pulse, which is perpendicular to B_0. This can cause variations in the signal intensity and contrast of the image [44]. Furthermore, higher field strengths require more powerful RF pulses, which consequently makes it more challenging to stay within the legally allowed (SAR). As there are currently no 7T MRI scanners which possess a body-coil, due to the higher field inhomogeneities, transmit elements need to be integrated

into the RF receive coils. This means that at ultra-high fields, more complex RF coil array designs are necessary. Additionally, the changes in longitudinal- and transverse relaxation times, although beneficial for T_2^*-weighted imaging, require adaptations in the design of the pulse sequences [9].

2.4 Susceptibility Weighted Imaging (SWI)

Susceptibility weighted imaging (SWI) [12] allows for the generation of additional contrast in certain tissues based on their susceptibility differences. The magnetic susceptibility χ is the proportionality constant between the magnetization $\boldsymbol{M}$ and the magnetic field intensity $\boldsymbol{H}$ as can be seen in [18, p. 744]:

$$\boldsymbol{M} = \chi\,\boldsymbol{H}\,. \tag{24}$$

It describes the magnetic properties of tissues when placed in a magnetic field, such as the main magnet of an MRI scanner. Tissues with negative susceptibilities, referred to as diamagnetic, possess paired electrons, which changes the magnetization in a negative way [45, p. 11]. The most common diamagnetic material in regards to MRI is water. Materials with positive susceptibilities, called paramagnetic or ferromagnetic depending on the strength of this effect, possess unpaired electrons, which have a positive effect on the magnetization of these tissues. An example for a paramagnetic material would be air, while iron in its unbound state is ferromagnetic. Since the magnetic susceptibility is a material constant, it is dependent on the type of tissue being imaged, with many tissues possessing distinct variations in their magnetic susceptibility compared to other neighbouring tissues. These susceptibility differences cause dephasing of the respective spins and, given sufficiently long echo times, this effect becomes measurable [46]. In typical structural imaging, only the magnitude of the measured complex signal is utilized, with the phase information often being discarded completely. It is exactly this phase information which ultimately allows for the creation of the previously mentioned contrast.

Tissues of interest for susceptibility weighted imaging include paramagnetic tissues such as partially deoxygenated blood, tissues containing iron, and clot. An example of a diamagnetic material that can be used for SWI is calcium [9, 41]. The related clinical applications include the research of pathologies like microbleeds, stroke, tumours, multiple sclerosis (MS) and vascular dementia [13].

SWI are most commonly acquired through the use of single echo GRE sequences, due to their T_2^* weighting making them particularly suitable for detecting the susceptibility variations of different tissues. The small flip angles employed in gradient echo sequences also allow the SAR to stay well below the legal limits. Susceptibility weighted imaging profits greatly from high- and ultra-high field strengths, not only by virtue of the intrinsic SNR increase mentioned in Chapter 2.3, but also because the phase scales linearly with the product between the echo

time TE and the static magnetic field B_0, meaning that sufficient phase contrast can be attained at shorter echo times [48].

To create an SWI image, a number of image pre-processing steps are necessary. The phase image, marked in Figure 16 as a), needs to be high-pass filtered in order to remove the phase information induced by the background field c). The background phase would otherwise obscure the phase components created by the susceptibility differences. In the next step, a phase mask d) is generated from the filtered phase by adjusting the signal intensity of the paramagnetic and diamagnetic sources [46].
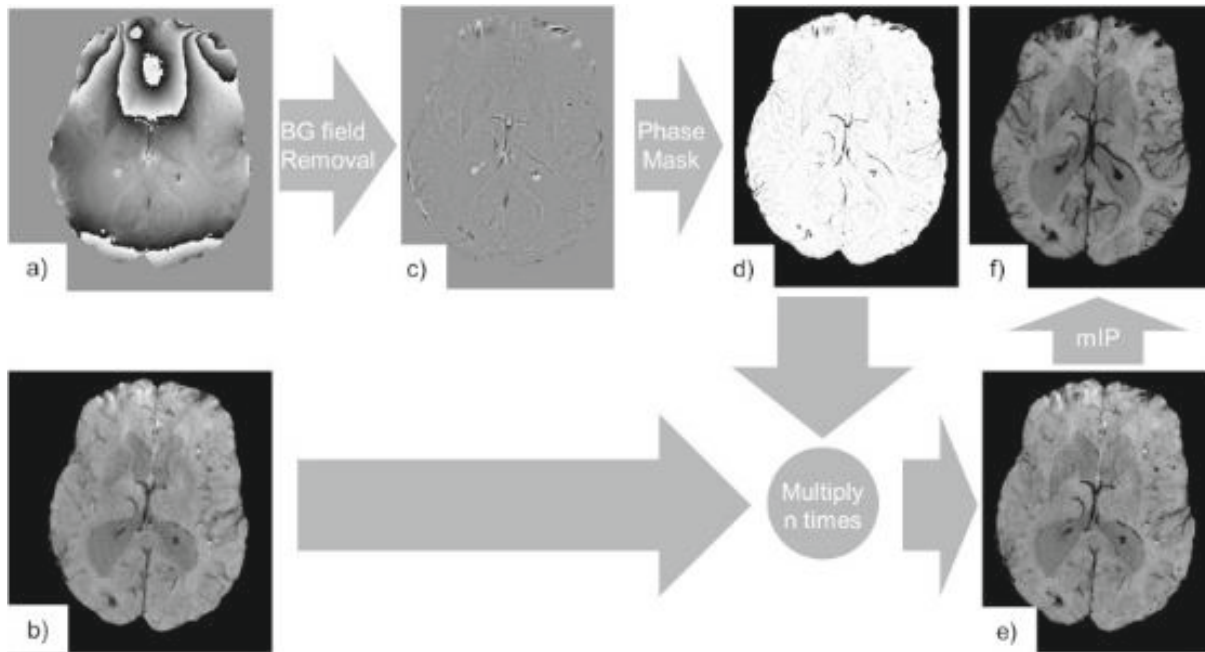
Figure 16: SWI Image processing steps. The phase image a) is high-pass filtered to remove the background phase c). A phase mask d) is generated from the filtered phase, with which the magnitude image b) is multiplied n times to create the susceptibility weighted image e). Additionally, a so-called minimum intensity projection mIP f) can be created in order to improve the visibility of veins. Reproduced from [46].

This allows the user to emphasize specific tissues based on their susceptibility χ value. This phase mask is then multiplied n-times with the magnitude image b) to create the susceptibility weighted image e) in the form of [46]:

$$SWI = Mag\ x\ Mask^n .\qquad(25)$$

The number of times *n* the magnitude needs to be multiplied by the phase mask is determined based on the maximum achievable contrast-to-noise (CNR) ratio. From the SWI image, a minimum intensity projection mIP can be created, which improves the visibility of veins.

2.5 CLEAR-SWI (Contrast-weighted, Laplace-unwrapped, bipolar multi-Echo, ASPIRE-combined, homogeneous, improved Resolution SWI):

Standard SWI, while showing improved contrast compared to more typically used imaging methods, suffers from a multitude of problems such as the high sensitivity to B_0 and B_1 inhomogeneities, signal dropout and wrap-like artefacts in regions with high ΔB_0 [13]. Much of this stems from the fact that standard SWI, and its homodyne phase filtering, were originally developed for field strengths of 1.5 T. This means that the stronger field inhomogeneities at high- and ultra-high fields were not accounted for, which ultimately causes the previously mentioned artifacts.

To overcome these challenges, the CLEAR-SWI (Contrast-weighted, Laplace-unwrapped, bipolar multi-Echo, ASPIRE-combined, homogeneous, improved Resolution SWI) [13] method was developed. In CLEAR-SWI the magnitude images of multiple echoes are contrast-weighted, either to maximize CNR or to optimize SNR, and then combined. This combination of the magnitude images over multi-echoes can decrease signal dropouts [49]. Phase unwrapping and filtering is divided into two distinct steps, and performed using the fast and robust Laplacian unwrapping method [50]. The phase information of each coil in the array for all echoes is combined using ASPIRE (A Simple Phase Image Reconstruction for multi-Echo data) [14]. The high B_1 field inhomogeneities are addressed without the need for manual configuration or a homogeneous reference coil [51]. The result of these improved image processing steps is that susceptibility weighted images with higher CNR and better resolution, free from wrap-around artifacts and with reduced signal dropout can be generated [13]. The enhancement in image quality is especially visible in smaller structure like veins.

Another advantage that has not yet been stated is that the data acquired for CLEAR-SWI can be used to create even more types of additional contrasts in retro-reconstruction. The multi-echo magnitude for example can be used to calculate T_2^* and R_2^* maps, which are matrices that store the voxel wise determined T_2^* and R_2^* values. Since R_2^* is proportional to the iron concentration, these maps can be beneficial in diagnosing pathologies which are shown to accumulate iron, such as Parkinson's disease (PD), multiple sclerosis (MS) and Alzheimer's disease (AD). Compared to that, the phase information can be further useful in applications such as quantum susceptibility mapping (QSM).

3 Methods

The primary aim of the experiments described in the next section was to compare GRAPPA and CAIPIRINHA accelerated measurements acquired with the VIBE sequence for high- and ultra-high fields (3T and 7T), both in terms of image quality, as well as quantitatively in regards to their SNR. From these acquired scans susceptibility weighted images (SWI) were created and comparisons were made between the two acceleration methods for various parameters.

3.1 Data Acquisition

Data was acquired with both a 7 Tesla MR whole body Siemens Magnetom scanner (Siemens Healthcare, Erlangen, Germany) and a 3T Siemens Prisma Fit scanner (Siemens Healthcare) at the High Field MR Centre in Vienna. Phantom measurements were performed with spherical oil phantoms in order to accurately determine the signal-to-noise ratio of the individual acceleration methods. This is because phantoms do not move and do not suffer from physiological noise, which would be detrimental to the SNR calculation based on the difference method, as the physiological noise is not consistent as opposed to the uneven noise distribution caused by the coil arrays needed for parallel imaging. One major problem with the spherical oil phantoms is, however, that they do not contain the same internal structures as human brains. Additionally, the wavelengths are different for phantoms compared to brain tissue, which means that not all effects visible in phantoms occur in the same way in in-vivo scans. This is why in-vivo data of three healthy volunteers was acquired as well, to analyse the effects CAIPI acceleration and other measurements parameters had in a more realistic setting. The in-vivo and phantom scans were performed using four different measurement protocols in total, which are listed in Table 1.

Protocol Name	Matrix Size	FA [°]	TE [ms]	TR [ms]
7T Protocol	704×594×144	10	4.3,8.6,12.9,17.2,21.5,25.8	31.00
3T Phantom	544×560×52	9	6.0,12.0,18.0,24.0,30.0,36.0	39.39
3T Magnetom	256×208×144	10	4.30	18.00
3T Multi Echo	256×208×80	15	5.0,10.0,15.0,20.0,25.0,30.0,35.0	40.00

Table 1: Measurement protocols and their resolution, flip angle (FA) in degrees, echo time (TE) in milliseconds and repetition time (TR) in milliseconds.

The coil used in conjunction with the 7T protocol is a 32-channel birdcage transceive coil (Nova Medical, Wilmington, USA) with 32 receive elements. The 3T Magnetom single echo images were acquired using a 20-channel birdcage head coil (Siemens Healthineers) with 20 receive elements, as this coil is very similar to the one that was used in [43]. The 3T Multi-echo scans were measured using a 64-channel birdcage head coil (Siemens Healthineers), since this coil with its 64 receive elements allows for higher image quality.

3.1.1 Phantom Measurements

Phantom measurements were acquired with spherical oil phantoms at high- and ultra-high field strengths using the 3T and 7T protocols listed in Table 1. To calculate their respective SNR values, each scan was performed twice in succession to utilize the difference method [35] mentioned in Chapter 2.2.1. At the start of each scan session (except for the scans listed in Table 3), 30 minutes were waited between inserting the oil phantom into the scanner and the start of the actual measurements in order to minimize the impacts of movement of the fluid on the SNR values. This effect was especially evident in earlier scan sessions where the first few scans showed strong movement artifacts and greatly reduced SNR compared to later scans which were acquired later in the same scan session. After accounting for the movement of the oil, the measured scans showed greater homogeneity and better reproducibility.

In the first series, scans were measured using the VIBE sequence (fl3d_vibe) with GRAPPA 3×3 and CAIPIRINHA 331 acceleration using the 7T protocol listed in Table 1. The GRAPPA 3×3 scans were acquired with GRE/separate reference lines while for CAIPI 331 both the reference region scan mode GRE/separate and integrated were measured. The specific acceleration factors, number of phase encoding (PE) and partition encoding (3D) reference lines, as well as the acquisition times are listed in Table 2.

Protocol	PE Reference lines	3D Reference lines	Acquistion Time TA [s]
VIBE_G3×3_separate	24	24	297
VIBE_CAIPI331_separate	24	24	297
VIBE_CAIPI331_integrated	128	96	634

Table 2: Number of reference lines in phase encoding direction (PE), partition direction (3D) and acquisition time (TA) for CAIPI331 separate, CAIPI331 integrated and GRAPPA 3×3 separate scans measured at 7T.

To create g-factor maps, scans using the same 7T protocol with no acceleration, GRAPPA 2×2, CAIPI 221, GRAPPA 3×3 and CAIPI 331 were acquired with 24 PE and 3D separate reference lines. The acquisition times for each acceleration method is listed in Table 3.

Protocol	Acquistion Time TA [s]
VIBE_no_acc	2433
VIBE_GRAPPA 2×2	610
VIBE_CAIPI 221	610
VIBE_GRAPPA 3×3	297
VIBE_CAIPI 331	273

Table 3: Differences in Acquisition time for scans measured with no acceleration, GRAPPA 2×2, CAIPI 221, GRAPPA 3×3 and CAIPI 331 at 7T field strength.

These measurements were taken prior to finding out the strong effects the movement of the oil within the phantom can have on the calculated SNR.

Similar scans to the first measurement series were reproduced at 3T field strengths using the 3T phantom protocol listed in Table 1, with a reduced number of slices and slight variations in resolution and echo times, to verify whether the effects found at 7 Tesla were also present at the lower field strengths. As can be seen in Table 4, the number of reference lines were kept constant to allow for better comparability. In terms of measurement parameters, only the acquisition time increased due to the switch from separate to integrated reference lines.

Protocol	Acquistion Time TA [s]
VIBE_G3×3_separate	134
VIBE_CAIPI331_separate	134
VIBE_CAIPI331_integrated	153

Table 4: Differences in Acquisition time for GRAPPA 3×3 separate, CAIPI331 separate and CAIPI331 integrated scans measured at 3T field strength.

Scans using the 7T protocol acquired with the VIBE sequence and GRAPPA 2×2 acceleration for a varying number of phase encoding (PE) and partition encoding (3D) reference lines were measured to determine the impact the number of reference lines in each encoding direction had on the calculated SNR values. To achieve this, a specific medium number of reference lines in one direction, approximately that in the centre of the available range (for example 70 reference lines in the phase encoding direction), was fixed and then five varying steps of partition encoding reference lines were measured. These steps ranged from a minimum number of 12 to the maximum number of 88 reference lines. All the measured phase encoding and partition encoding steps, as well as the acquisition time needed for this particular configuration, are documented in Table 5.

Protocol	Reference lines PE	Reference lines 3D	Acquisition Time TA [s]
GRAPPA_2×2_12_44	12	44	306
GRAPPA_2×2_41_44	41	44	310
GRAPPA_2×2_70_44	70	44	314
GRAPPA_2×2_99_44	99	44	318
GRAPPA_2×2_128_44	128	44	323
GRAPPA_2×2_70_12	70	12	307
GRAPPA_2×2_70_24	70	24	309
GRAPPA_2×2_70_44	70	44	314
GRAPPA_2×2_70_64	70	64	318
GRAPPA_2×2_70_88	70	88	324

Table 5: Reference lines in phase encoding (PE) direction, in partition (3D) direction and acquisition time in seconds for phantom measurements acquired with the VIBE sequence and GRAPPA 2×2 acceleration at 7T. Acquisition time scales proportionally to the number of reference lines.

3.1.2 In-Vivo Measurements

In-vivo measurements were acquired at high- and ultra-high field strengths with the 3T Magnetom, the 3T Multi-echo and the 7T protocols listed in Table 1, through the help of three healthy volunteers.

In the first in-vivo series, magnitude images were acquired using the VIBE sequence with the 7T protocol using CAIPI 331 acceleration for separate and integrated reference lines. The aim of these measurements was to verify the findings of previously measured phantom scans. The number of phase encoding (PE) and partition encoding (3D) reference lines, as well as the acquisition times are listed in Table 6.

Protocol	Reference lines PE	Reference lines 3D	Acquisition Time TA [s]
GRE/separate	24	24	273
Integrated_24ref	24	24	287
Integrated_48ref	48	48	334

Table 6: Reference lines in phase encoding (PE) direction, partition direction (3D) and acquisition time of CAIPI331 scans using GRE/separate reference lines, as well as 24- and 48 integrated reference lines.

With the 3T Magnetom protocol listed in Table 1, it was tested whether the findings published in Figure 7 of the Magnetom Flash 1/2012 [43] article could be replicated on the Prisma Fit scanner using near identical scan parameters. This figure compares single echo magnitude images accelerated with GRAPPA 2×2 and CAIPI 221. Additionally, the CAIPIRINHA reorder scheme of CAIPI 142 was acquired with the same settings to evaluate whether this configuration leads to improved image quality, and the same comparison was made for scans with total acceleration factor of six, namely GRAPPA 3×2, CAIPI 321 and CAIPI 164. The acceleration factors and their corresponding acquisition times are listed in Table 7.

Protocol	Acquistion Time TA [s]
VIBE_GRAPPA 2×2	119
VIBE_CAIPI 221	119
VIBE_CAIPI 142	119
VIBE_GRAPPA 3×2	87
VIBE_CAIPI 321	80
VIBE_CAIPI 164	80

Table 7: Protocol name with the used acceleration methods and their acquisition times single echo magnitude images measured at 3T.

Using the same single echo 3T protocol listed in Table 1, magnitude images were acquired with an acceleration factor of R = 4 in the phase encoding direction and reorder shifts ranging from zero to three. The corresponding CAIPI schemes are CAIPI 140, CAIPI 141, CAIPI 142, and CAIPI 143. All parameters except the reorder shift were identical for these scans. This was done in order to qualitatively determine the optimal reorder shift for this particular CAIPI

acceleration on the Prisma Fit scanner using this specific coil. It is important to note that during this scan session, only the bottom half of the coil was plugged in, resulting in greatly diminished image quality in the upper parts of all four scans. As this affected all images equally, and the comparison was strictly used to determine the optimal CAIPI scheme for this configuration relative to each other, the scans were not repeated.

Similar measurements were then made using the same 3T Magnetom Protocol, with a total acceleration factor of R = 6 in the PE direction, and reorder shifts from zero to 5 (the maximum). The related CAIPI schemes are CAIPI 160, 161, 162, 163, 164 and 165. Once again, all parameters except for the reorder shift stayed identical.

The 3T Multi-echo protocol listed in Table 1 was used to acquire fast multi echo scans with similar resolutions to their single-echo protocol counterparts. Their purpose was to allow for the creation of CLEAR-SWI images of GRAPPA 2×2 and CAIPI 142 as well as GRAPPA 3×2 and CAIPI 164 scans with differences in the size of their FOV and resolution. The field of view, resolution and acquisition time for each configuration is documented in Table 8.

Protocol	FOV	Matrix Size	Acquisition Time TA [s]
GRAPPA 2×2	210×170	256×208×80	166
CAIPI 142	210×170	256×208×80	166
GRAPPA 3×2	210×170	256×208×80	114
CAIPI 164	210×170	256×208×80	116
GRAPPA 3×2 large FOV	230×186	256×208×80	114
CAIPI 164 large FOV	230×186	256×208×80	116
GRAPPA 3×2 vlarge FOV high-res	256×208	352×286×80	154
CAIPI 164 vlarge FOV high-res	256×208	352×286×80	154

Table 8: Field of view (FOV), resolution and acquisition time for the different protocols measured at 3T in-vivo.

Using the 7T Protocol, high resolution in-vivo measurements were performed with GRAPPA 2×2, GRAPPA 3×3, CAIPI 221 and CAIPI 331 accelerations to create CLEAR-SWI images and compare the resulting image quality of both acceleration methods. The acquisition time for each acceleration method is listed in Table 9.

Protocol	Acquistion Time TA [s]
VIBE_GRAPPA 2×2	406
VIBE_CAIPI 221	449
VIBE_GRAPPA 3×3	212
VIBE_CAIPI 331	204

Table 9: Protocol name with the utilized acceleration methods and their corresponding acquisition times for SWI images measured at 7T.

4 Analysis

4.1 SNR analysis (Offline)

The raw DICOM-format [52] images of the measured phantom and in-vivo scans were exported from the scanner and converted into the NIfTI (Neuroimaging Informatics Technology Initiative) format. This step was done through the use of the in-house developed MATLAB program "Siemens DICOM sort and convert to NIfTI" [53]. The purpose of this conversion is that the NIfTI file format allows for more comprehensive viewing of image quality and differences between individual scans.

A script was written to calculate SNR values from these NIfTI files based on the difference method [35]. Sum- and difference images were created with the help of the command line tool fslmaths [54, 55]. These sum and difference images were then read into MATLAB for further processing. The magnitude values of each scan were combined over all echoes and subsequently divided by the echo number to create a combined magnitude image. The mean values of the entire images were calculated, and a binary mask was created based on a manually chosen cut-off point (a fraction of the mean value). This mask was used to remove the background from the rest of the image. SNR maps were then created by subdividing the sum and difference images of the phantom into 8×8×8 voxels (cubes), which each make up a single volume of interest (VOI). The SNR was calculated for each VOI based on formula (21), with the signal portion being derived from the mean value of the sum image, while the amount of noise was given by the standard deviation of the difference image. All calculated SNR values were then stored into the SNR maps to visualize their spatial distribution and the mean SNR value of the entire phantom was calculated.

Based on this SNR script, a modified version was written in order to calculate the SNR maps for each individual echo of multi-echo scans. This was particularity useful since the presence of strong artifacts was discovered in later echoes of scans acquired with the VIBE sequence with CAIPIRINHA acceleration and integrated reference lines.

Another modified version was created where in addition to the SNR maps, g-factor maps were calculated. This was achieved by acquiring one fully sampled (not accelerated) scan and then calculating the g-factor of each 8×8×8 voxel based on formula (20), by dividing the SNR of the fully sampled scan by the corresponding accelerated SNR values, as well as the additional square root of the total acceleration factor, according to:

$$g = \frac{SNR_{Full}}{SNR_{PI} \cdot \sqrt{R}}. \tag{26}$$

The division by the square root of the total acceleration factor accounts for the intrinsic increase in SNR for higher acquisition times.

4.2   Online Retro Reconstruction (RR)

The VIBE sequence only allows for the creation of magnitude images during the initial scan. Any phase images needed for the generation of susceptibility weighted images or CLEAR-SWI images had to be retro reconstructed from the raw data file (.dat). This was done directly on the scanner, using the ICE (Image Calculation Environment) [49, p. 19] developed by Siemens, with the software tool "TWIX", which allows image reconstruction parameters to be modified.

4.3   SWI Processing

Magnitude and phase images were used to create susceptibility weighted images (SWI) using the Linux standalone executable of CLEAR-SWI contained in the v.4.0.6 of mritools_ubuntu_22.04 [13].

5 Results

5.1 Phantom Results

5.1.1 SNR of GRAPPA 3×3 and CAIPI 331 with separate and integrated reference lines at 7T

In this first phantom measurement series, SNR values for three different scans were calculated for each individual echo using the method described in 4.1, and the results are listed in Table 10.

	SNR		
echo	CAIPI331_integrated	CAIPI331_separate	GRAPPA_3×3_separate
1	426.9	139.2	149.5
2	412.4	145	157.6
3	18.6	127.6	141.5
4	19.5	130.2	148.2
5	20.5	112.5	127.2
6	12.1	110.9	127.4
mean SNR	151.7	127.6	141.9

Table 10: Calculated SNR for each echo and mean SNR for CAIPI331 integrated, CAIPI331 separate and GRAPPA 3×3 separate scans acquired at 7T field strength.

As can be appreciated from this table, the SNR values in the case of CAIPI 331 with integrated reference lines are exceptionally high for the first two echoes, while a steep decrease in SNR occurs starting from echo 3. Comparing this to the scan acquired with the same acceleration factor but using GRE/separate reference lines, it can be seen that the SNR values are considerably more consistent, with only a slight decrease in SNR towards higher echo numbers. A similar trend is evident when looking at the scan using GRAPPA 3×3 acceleration with separate reference lines, which is even more homogeneous in terms of its SNR values.

The magnitude images and the corresponding SNR maps for all six echoes of the GRAPPA 3×3 separate, CAIPI 331 separate and CAIPI 331 integrated scans are depicted in Figure 17. The individual SNR values listed in Table 10 for each echo are included for reference and the SNR maps show which regions have particularly high or low SNR. In general, the outer edges, especially the lower parts, possess higher SNR. This is most likely due to these regions being closest to the receiver coils and therefore benefiting from the increased coil sensitivities.

The scans acquired with GRE/separate reference lines show aliasing artifacts towards the centre of the image, which are marked by green circles in echo 3. The SNR maps for the scans using separate reference lines, acquired with GRAPPA 3×3 and CAIPI 331 accelerations look quite similar. They show good homogeneity across all six echoes, with GRAPPA 3×3 having overall slightly higher SNR compared to CAIPI 331. Compared to that, the scan measured using

CAIPI 331 acceleration with integrated reference lines shows magnitude images free from aliasing artifacts for the first two echoes, with exceptionally high SNR, marked by a blue rectangle in Figure 17.
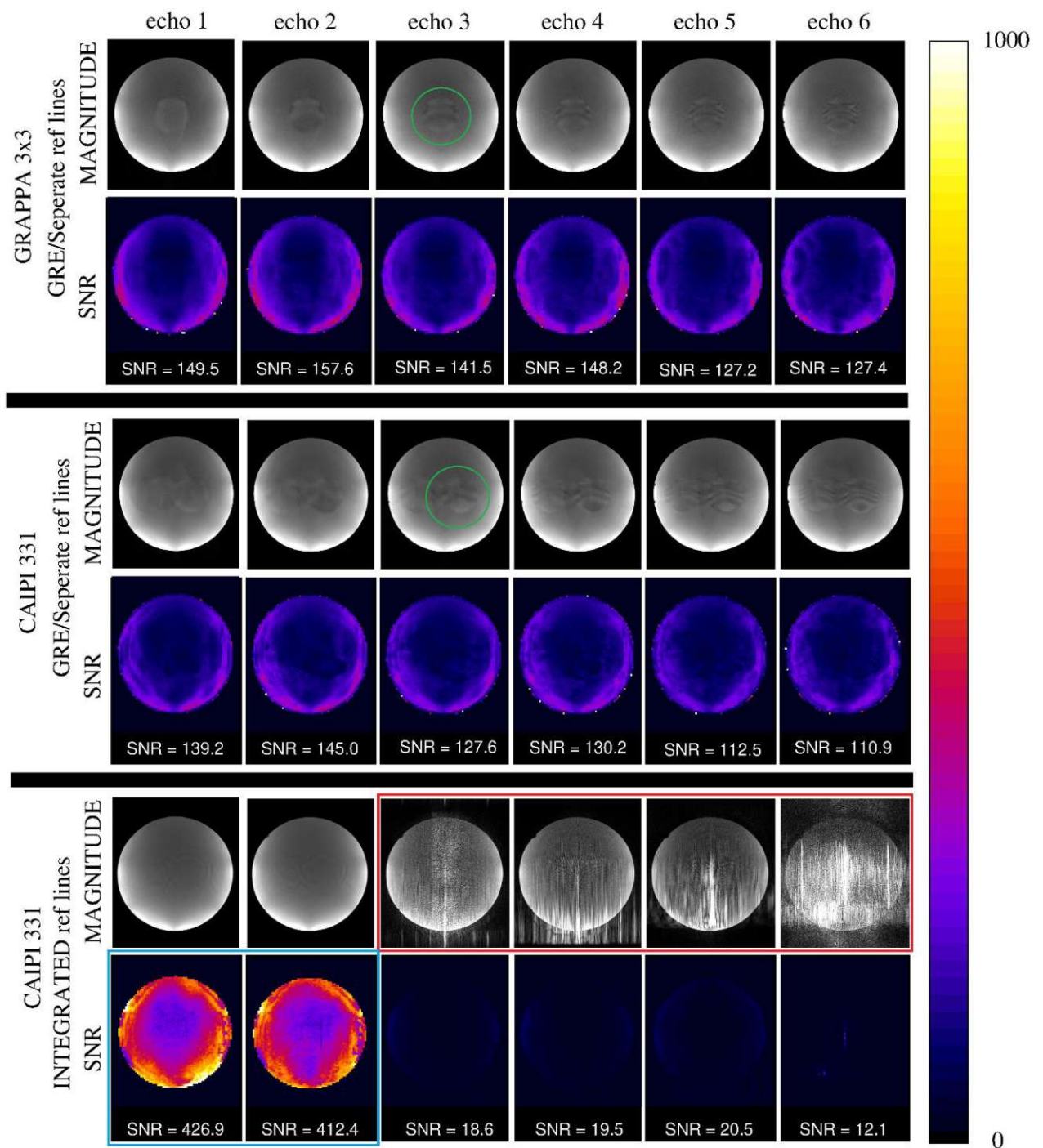
Figure 17: Magnitude images and SNR maps for all six echoes of three different protocols at a field strength of 7T. The top two rows show scans acquired with GRAPPA 3×3 acceleration and separate reference lines. The middle section shows the same scans using CAIPI 331, while the bottom section uses CAIPI 331 and integrated reference lines. GRAPPA and CAIPI images are quite similar for GRE/separate while "integrated" shows high SNR in the first two echoes, marked by a blue rectangle, and strong artifacts starting from the third echo, marked by a red rectangle. These artifacts drastically reduce the resulting SNR. Additionally, aliasing artifacts are visible in the magnitude images of the scans using separate reference lines, marked by green circles in echo 3.

Starting from echo number three, strong artifacts begin to arise which are clearly visible in the magnitude images, marked by a red rectangle. The corresponding SNR maps show that that the resulting SNR values for these echoes are extremely low, with the phantom being barely distinguishable from the background.

The reconstruction time of these scans measured with CAIPI acceleration and integrated reference lines was approximately 40 minutes, while their GRE/separate counterparts took about 2 minutes to reconstruct. This fact, coupled with the strong artifacts starting from echo 3, makes it likely that this effect is caused by an implementation issue of the integrated reference lines scan mode option in the VIBE sequence.

A comparison of the calculated SNR values of each echo for CAIPI 331 with integrated reference lines and CAIPI 331 with GRE/separate reference lines is shown in Figure 18, where the striking decrease in SNR for integrated reference lines is clearly visible.
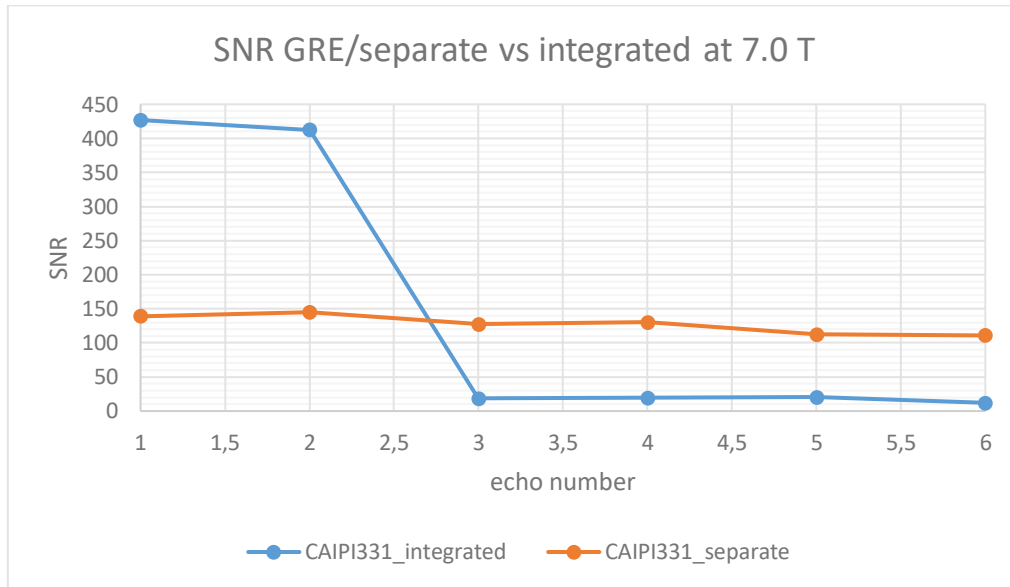
Figure 18: Calculated SNR values for each echo for scans acquired with the VIBE sequence and CAIPI 331 acceleration. Reference lines were measured by two different methods: integrated into the entire data acquisition (integrated) and in a prior, separate scan (GRE/separate). Integrated reference lines cause a strong decrease in SNR starting from the third echo, while separate stays relatively constant.

In terms of mean SNR over all six combined echoes, CAIPI 331 with integrated reference lines shows the highest value overall as can be seen in Table 11. However, the SNR efficiency described in Eq. (23) of Chapter 2.2.1, which accounts for the higher SNR due to the increased acquisition time, shows that the SNR efficiency of this method is actually the lowest.

Protocol	mean SNR	SNR efficiency	Acquistion Time TA [s]
CAIPI331_integrated	151.7	6.0	634
CAIPI331_separate	127.6	7.4	297
GRAPPA3×3_separate	141.9	8.2	297

Table 11: Mean SNR, SNR efficiency and Acquisition Time for CAIPI331 integrated, CAIPI331 separate and GRAPPA 3×3 separate scans at 7T.

While changing the reference scan mode from integrated to GRE/separate increases the SNR efficiency of CAIPI 331, it is still lower than then the more conventional GRAPPA 3×3 acceleration. This is also visible in Figure 19, where the SNR values of each of the six echoes for GRAPPA 3×3 and CAIPI 331, both measured with separate reference lines, are plotted. While the two lines are quite similar in form, the SNR values for GRAPPA 3×3 are 11% higher on average compared to their CAIPI 331 counterparts.
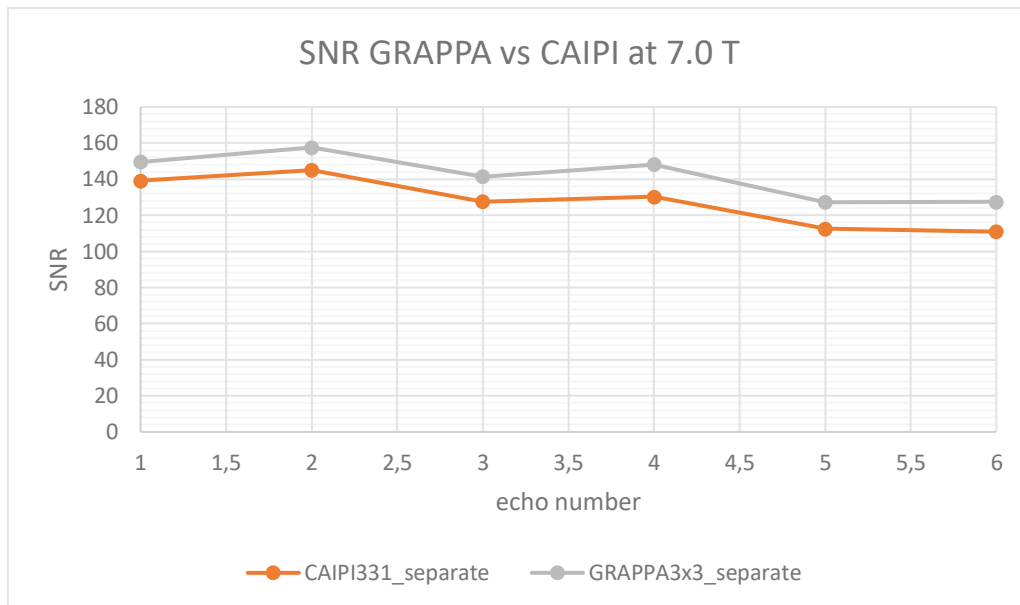
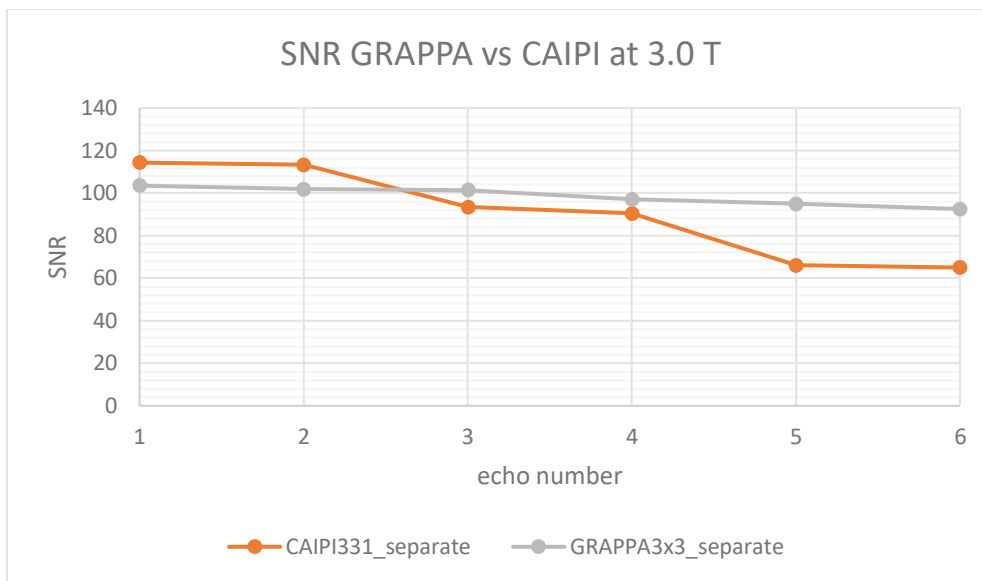*Figure 19: Calculated SNR values for each echo for two scans acquired with the VIBE sequence using separate reference lines for GRAPPA 3×3 and CAIPI 331 accelerations measured at 7T.Both acceleration methods show very similar behaviour with a slight decrease in SNR with increasing echo numbers.*

5.1.2 G-factor maps for GRAPPA 2×2, CAIPI 221, GRAPPA 3×3 and CAIPI 331 scans using separate reference lines at 7T

Figure 20 shows the magnitude images, SNR maps and g-factor maps for scans acquired with no acceleration, GRAPPA 2×2, CAIPI 221, GRAPPA 3×3 and CAIPI 331. As would be expected, the mean SNR is overall the highest for the scan without any acceleration. This can also be seen in the brightness of the SNR map. GRAPPA 3×3 and CAIPI 331 show results which are in line with the findings of Chapter 5.1.1, where the CAIPI scan has decreased homogeneity and SNR compared to its GRAPPA counterpart. Surprisingly the GRAPPA 2×2 scans has overall lower SNR compared to its CAIPI 221 counterpart, which is also visible in the g-factor maps. This behaviour could not be replicated in any of the later measurements. Most likely this is caused by movement artifacts, as these CAIPI 221 and GRAPPA 2×2 scans were acquired directly after inserting the phantom into the scanner, without the in later measurements added 30 minutes of wait time for the movement of the oil to subside.
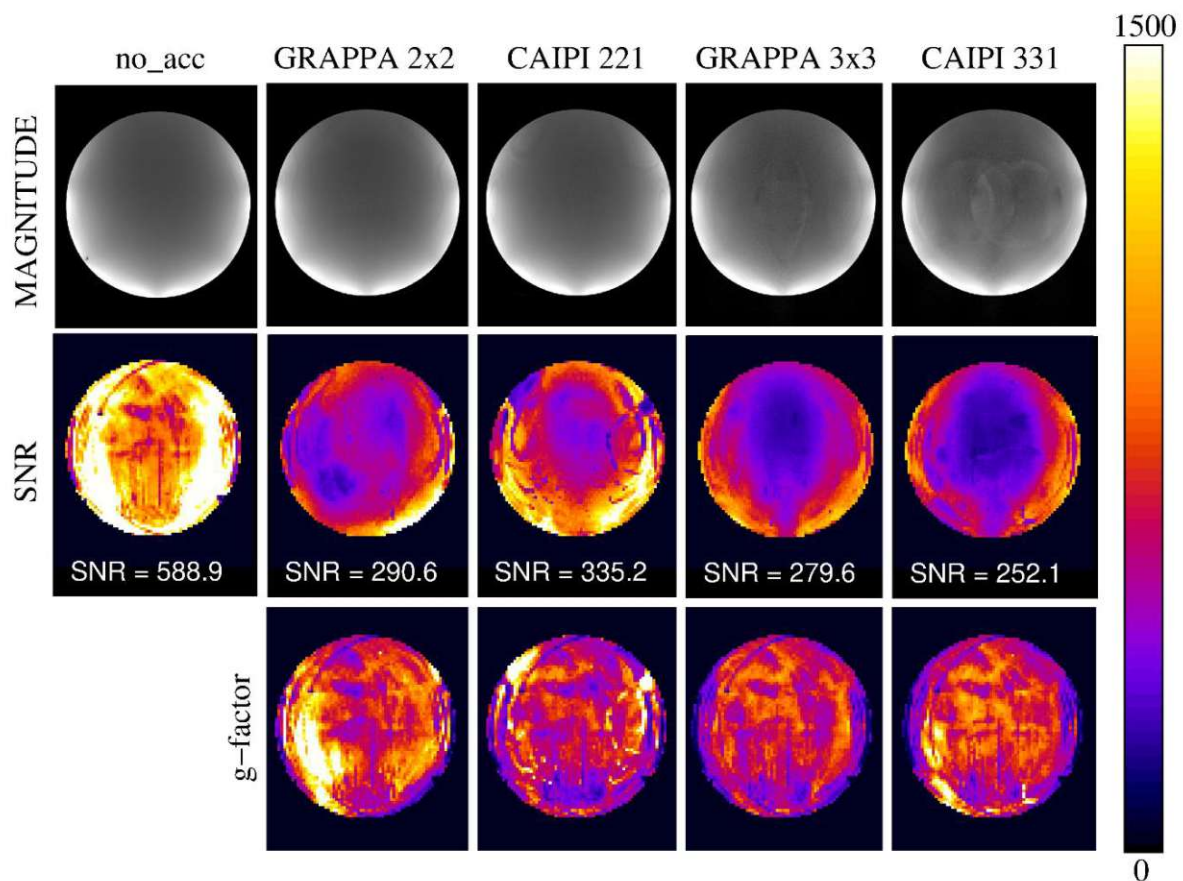
Figure 20: Magnitude images, SNR maps and g-factor maps for scans acquired with no acceleration, GRAPPA 2×2, CAIPI 221, GRAPPA 3×3 and CAIPI 331 acceleration. SNR for no acceleration is expectedly high, GRAPPA 3×3 looks slightly better than CAIPI 331 in SNR and g-factor maps. GRAPPA 2×2 has lower overall SNR compared to CAIPI 221 which is also visible in the g-factor map.

5.1.3 SNR of GRAPPA 3×3 and CAIPI 331 with separate and integrated reference lines at 3T

The calculated SNR values for each of the six echoes for the three measurements at 3T are listed in Table 12. As can be appreciated from this table, a similar trend can be observed as in the 7T scans, with GRAPPA 3×3 separate and CAIPI 331 separate showing strong similarities. The GRAPPA 3×3 scans once again show slightly increased mean SNR, around 9% higher than for their CAIPI 331 counterpart. The CAIPI 331 scan acquired with the integrated reference lines has, as expected, high SNR for the first two echoes and very low SNR for echoes three and four. Surprisingly, the SNR values for the last two echoes increase again to levels comparable with the scans measured using the separate reference lines.

	SNR		
echo	CAIPI331_integrated	CAIPI331_separate	GRAPPA3×3_separate
1	257.6	114.3	103.5
2	253.4	113.3	101.9
3	25.3	93.5	101.4
4	19.8	90.4	97.0
5	86.3	66.1	94.9
6	70.5	65.0	92.5
mean SNR	118.8	90.4	98.5

Table 12: Calculated SNR for each echo and mean SNR for CAIPI331 integrated, CAIPI331 separate and GRAPPA 3×3 separate scans acquired at 3 T field strength.

The reason for this increase in SNR for echo 5 and 6 for integrated reference lines is visible in Figure 21, where magnitude images and SNR maps for all echoes of each of the three compared scans are shown. Same as at 7T, strong artifacts begin to arise in the magnitude image of CAIPI 331 integrated starting from echo three, marked by the red rectangle in Figure 21. The difference to 7T is that the artifacts at 3T cover larger areas, especially at echoes five and six, where the majority of the image became saturated. This in turn lead to misleadingly high SNR of these two echoes, as the saturated images possess both high signal and comparably low standard deviations, marked by the blue rectangle.

The GRAPPA 3×3 and CAIPI 331 scans measured with separate reference lines show aliasing artifacts in the magnitude images, marked by the green circles in echo 3, which are more pronounced in the CAIPI accelerated image. Even though the SNR maps for both acceleration methods look quite similar, the stronger aliasing artifacts in CAIPI lead to decreased homogeneity.
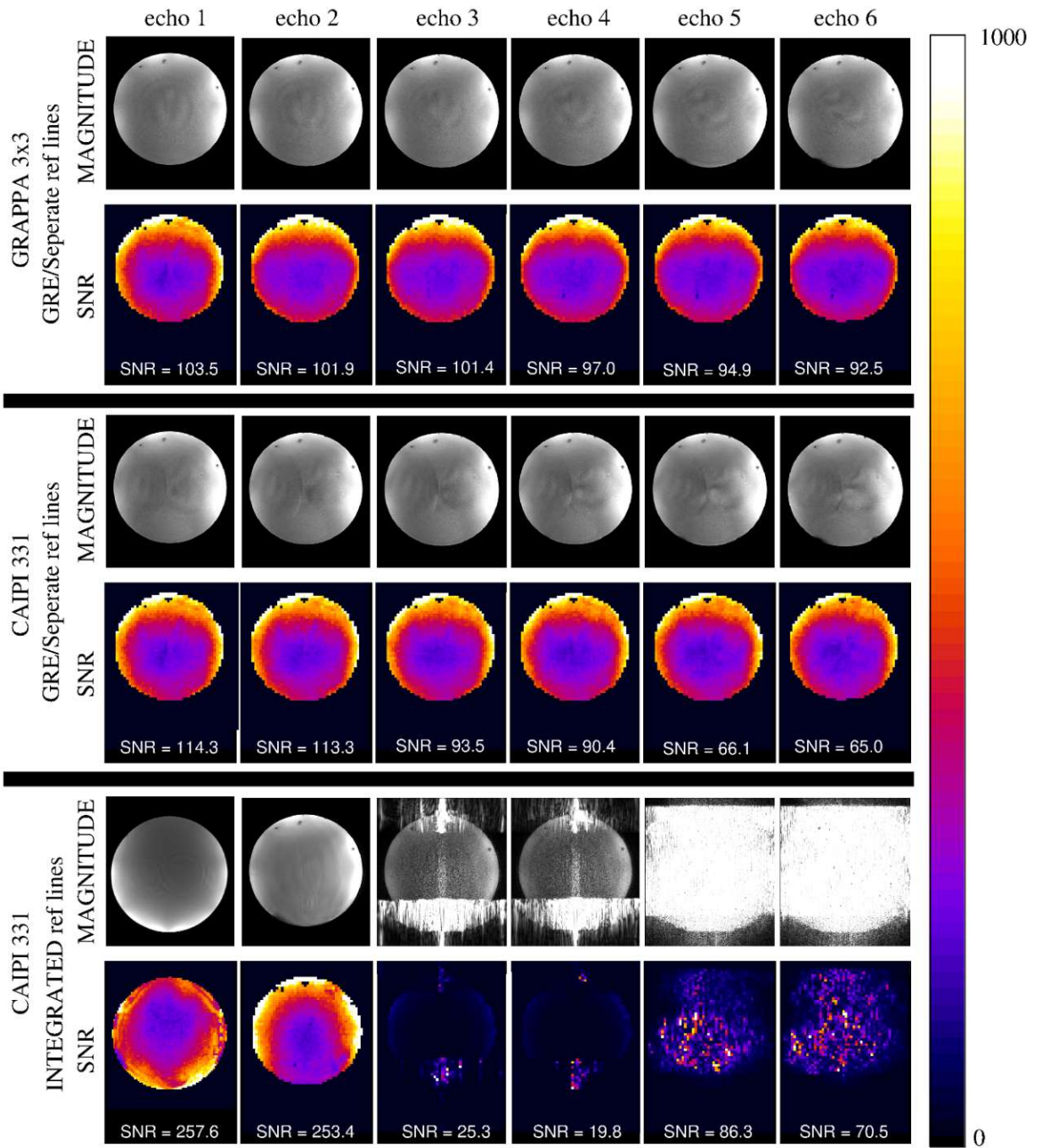
Figure 21: Magnitude images and SNR maps for all six echoes of three different protocols at a field strength of 3T. The top two rows show scans acquired with GRAPPA 3×3 acceleration and separate reference lines. The middle shows the same scans using CAIPI 331, while the bottom uses CAIPI 331 and integrated reference lines. The GRAPPA and CAIPI images acquired with GRE/separate reference lines are very similar, while integrated reference lines cause strong artifacts starting from the third echo, marked by a red rectangle. These strong artifacts cause saturation in echoes five and fix, falsely increasing the SNR values, marked by a blue rectangle.

The mean SNR values, SNR efficiency and acquisition times for the three scans are listed in Table 13. Not only is the mean SNR for CAIPI 331 acquired with integrated reference lines the highest, which would be expected due to the longer acquisition time, but also the SNR

efficiency combined over all six echoes. This, however, is only due to the last two echoes being saturated and the therefore falsely high SNR of echoes five and six.

Protocol	mean SNR	SNR efficiency	TA [s]
CAIPI331_integrated	118.8	9.6	153
CAIPI331_separate	90.4	7.8	134
GRAPPA3×3_separate	98.5	8.5	134

Table 13: Mean SNR, SNR efficiency and Acquisition Time for CAIPI331 integrated, CAIPI331 separate and GRAPPA 3×3 separate scans at 3T field strength.

In Figure 22, the calculated SNR values for each of the six individual echoes of CAIPI 331 integrated and CAIPI 331 separate are plotted. As can be seen, the difference in SNR between the two reference line modes is smaller compared to at 7T, but still considerable. The same decrease in SNR starting from echo three for integrated reference lines is visible, with echoes five and six being even higher than their CAIPI 331 separate counterparts due to the saturation of the magnitude images.
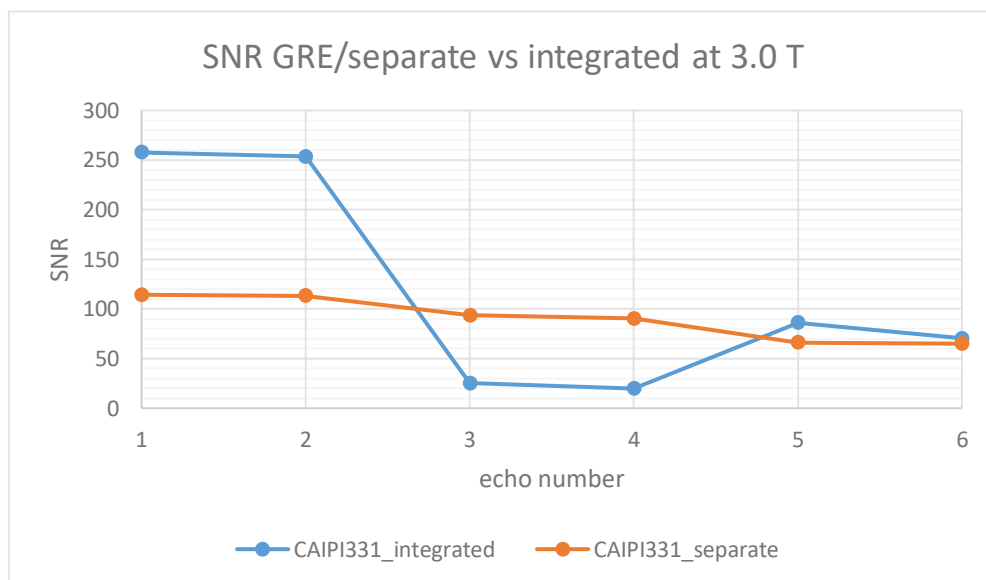
Figure 22: Calculated SNR values for each echo for scans acquired with the VIBE sequence and CAIPI 331 acceleration. Reference lines were measured either integrated into the entire data acquisition (integrated) or in a prior, separate scan (GRE/separate). Integrated reference lines cause a strong decrease in SNR starting from the third echo. SNR begins to increase again starting from echo 5 due to the strong artifacts.

A comparison between the calculated SNR values of CAIPI 331 and GRAPPA 3×3 with separate reference lines in Figure 22 shows that the first two echoes of the CAIPI 331 accelerated scan are higher than using GRAPPA 3×3. Later echoes, especially echoes five and six, are substantially lower in the case of CAIPI 331. Not only are the SNR values for the with CAIPIRINHA accelerated scans less homogeneous, but their combined mean SNR is lower overall.

Figure 23: Calculated SNR values for each echo of two scans acquired with the VIBE sequence using separate reference lines for GRAPPA 3×3 and CAIPI 331 acceleration. GRAPPA 3×3 shows a very constant and slight decrease in SNR for higher echo numbers, while CAIPI 331 shows a more pronounced, step-like SNR reduction.

5.1.4 SNR of GRAPPA 2×2 depending on the number of reference lines at 7T

5.1.4.1 SNR of GRAPPA 2×2 as a function of the number of phase encoding reference lines at 7T

To determine the effect that the number of phase encoding reference lines have on the SNR values of the resulting images, a constant number of 44 reference lines in partition direction was fixed and then five varying steps of phase encoding reference lines were measured. These steps ranged from a minimum of 12 to a maximum of 128 reference lines.

The calculated SNR values of these five configurations for each of the six echoes, and the mean SNR, are listed in Table 14. The naming scheme is PE_3D, meaning that the first number is the amount of phase encoding reference lines while the second number describes the amount of partition encoding reference lines.

	SNR				
echo	12_44	41_44	70_44	99_44	128_44
1	257	353.8	337.2	373.7	390.7
2	267.4	360	334.6	365.4	391.7
3	234.6	311.9	283.3	315.2	343.9
4	233.9	305.5	267.4	310.5	347.6
5	199.8	252.7	215.2	259.3	284.2
6	196.1	241.2	195.7	246.2	267.6
mean SNR	231.5	304.2	272.2	311.7	337.6

Table 14: Calculated SNR values for each of the six echoes of all measured variations in phase encoding reference lines and their mean SNR. SNR is proportional to the number of reference lines and decreases with the echo number.

As can be appreciated from this table, a trend towards higher SNR for increased number of phase encoding reference lines is visible, as would be expected. For easier comprehension, the SNR values listed in Table 14 are plotted in Figure 24. As can be seen in this figure, the largest deviation from this trend is the surprisingly low SNR value of the "medium" configuration with 70 phase encoding reference lines (marked in orange). A considerably strong decrease in SNR for the individual echoes can be seen for all configurations, but is especially evident for the variations with higher number of phase encoding reference lines. While the combination with only 12 PE reference lines has the lowest overall SNR, its deviations between the individual echoes is also the lowest.
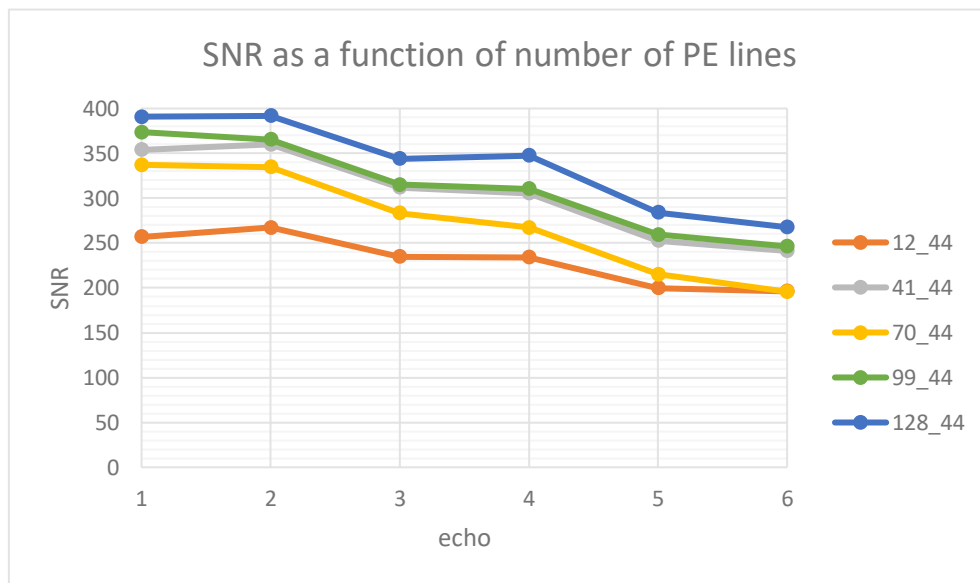
Figure 24: Calculated SNR for each of the six echoes for different configurations of phase encoding and partition reference lines, with the naming scheme being PE_3D. A step-like reduction in SNR for increasing echo numbers can be seen. Very low number of PE reference lines (12) lead to especially low SNR.

These effects can be seen in Figure 25, where the magnitude images and corresponding SNR maps of all six echoes for three reference line configurations are shown. The lowest number of PE reference lines, namely 12, is shown in the top, while the medium amount of 70 PE reference lines is depicted in the middle and the maximum number of 128 is illustrated at the bottom. The scan acquired with only 12 PE reference lines shows aliasing artifacts in the magnitude images, an example of this is marked by a red circle in echo 3. These artifacts would explain the resulting overall lower SNR for this configuration. The corresponding SNR maps, however, not only show the most consistent SNR values as seen in Figure 25, but are also spatially the most homogenous. The clear trend towards higher SNR with an increased number of phase encoding reference lines can be observed when comparing the SNR maps of all three configurations, with their overall brightness, which relates to their SNR values, increasing from top to bottom.
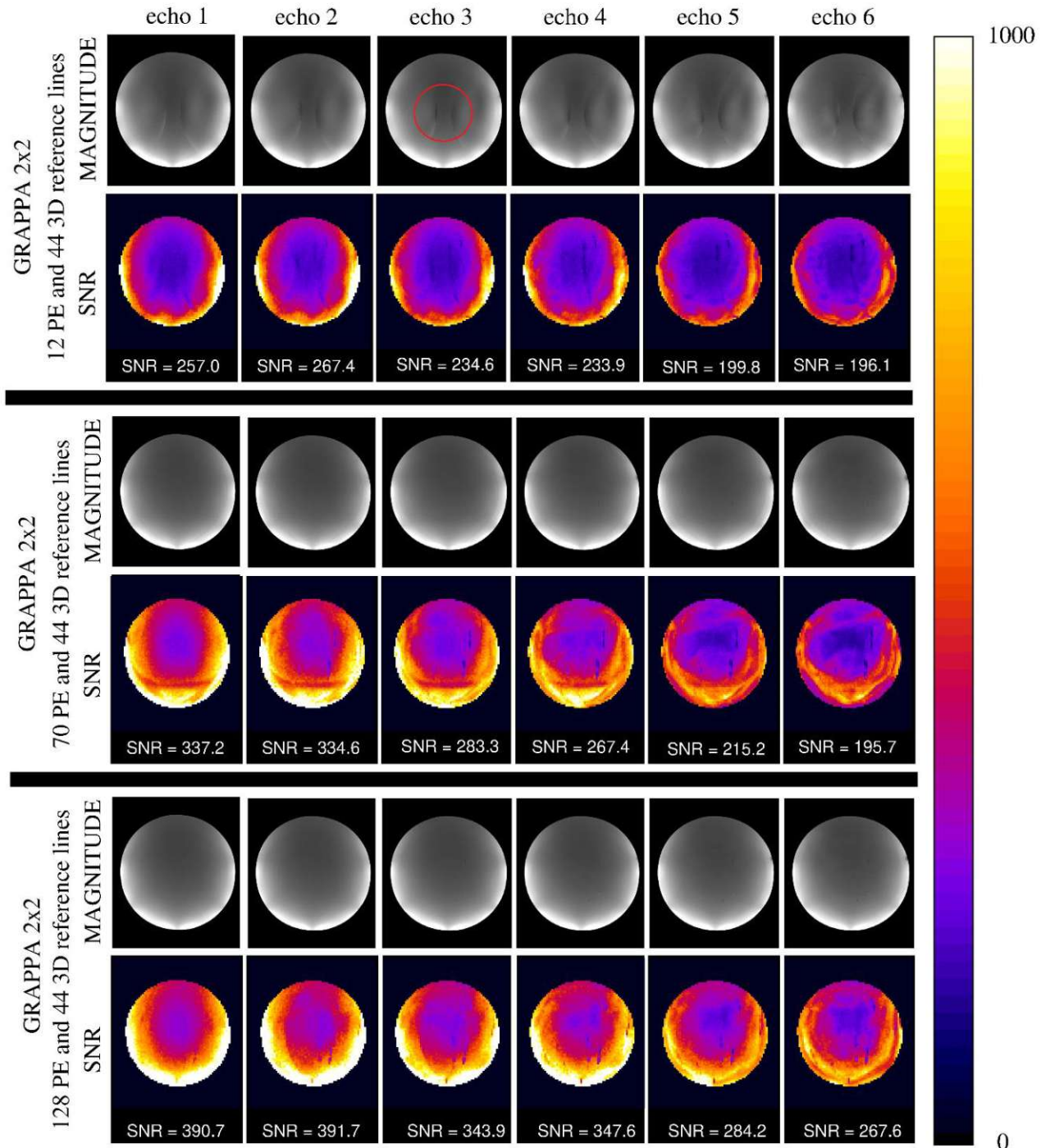
Figure 25: Magnitude images and the corresponding calculated SNR maps for all six echoes of GRAPPA 2×2 scans measured at 3T for varying numbers of phase encoding reference lines. The top two rows show a scan with 12 PE reference lines, the middle with 70 and the bottom with 128. The scan with only 12 PE reference lines clearly shows artifacts in the magnitude image, marked by a red circle in echo three. These artifacts reduce the SNR, and for higher numbers of reference lines the image becomes more homogeneous and SNR increases accordingly. The SNR is generally higher for earlier echoes and increases with the number of reference lines, which can be appreciated by the brighter colours of the SNR maps.

It is worth to mention that the SNR decreases significantly for the variations with 70 and 128 PE reference lines in their later echoes, namely echoes five and six. The magnitude images of both these configurations are free from aliasing artifacts.

45

The mean SNR, SNR efficiency and acquisition time of all five phase-encoding reference line configurations are listed in Table 15. It can be appreciated that while an increase in the number of reference lines intrinsically increases the acquisition time and therefore consequently also the mean SNR, the SNR efficiency which accounts for this effect, still increases in accordance to the number of phase encoding reference lines.

Variation	mean SNR (PE)	SNR eff. (PE)	TA [s]
12_44	231.5	13.2	306
41_44	304.2	17.3	310
70_44	272.2	15.4	314
99_44	311.7	17.5	318
128_44	337.6	18.8	323

Table 15: Calculated mean SNR, SNR efficiency and acquisition times, depending on the number of reference lines in the phase encoding direction. Mean SNR is proportional to the number of reference lines, which correlate to higher acquisition times. SNR efficiency is still higher overall for scans measured with more reference lines.

The only deviation from this trend is caused by the especially low mean SNR of the configuration with 70 PE reference lines. This is visible in Figure 26, where the SNR efficiency is plotted for each of the five variations.
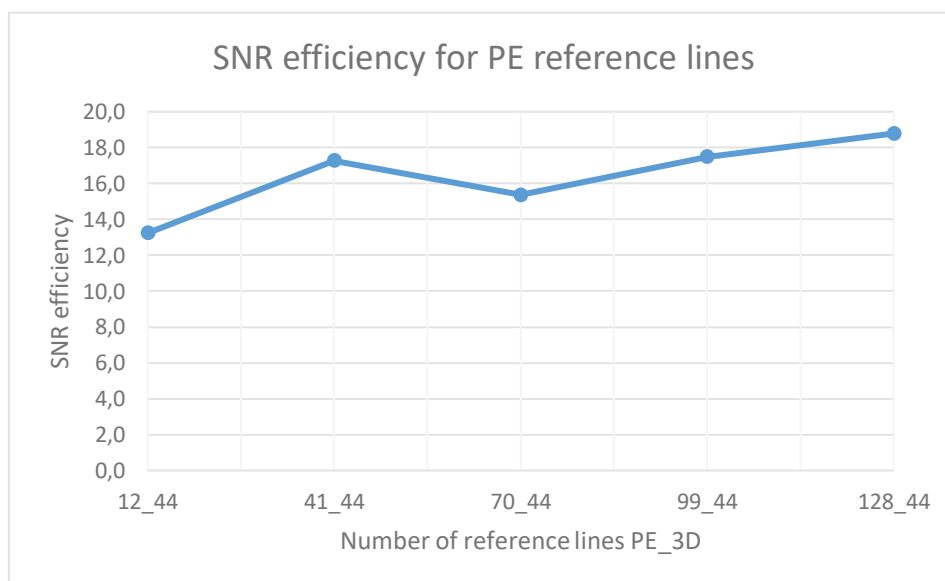
Figure 26: Calculated SNR efficiency of the five measured variations in phase encoding reference lines. A clear trend towards increases SNR efficiency for higher number of PE reference lines can be seen.

Nonetheless, an increase in PE reference lines to the maximum possible amount which still allows for the desired acquisition time seems to be beneficial to the resulting SNR of the measured image.

5.1.4.2 SNR of GRAPPA 2×2 as a function of the number of partition encoding reference lines at 7T

The calculated SNR values of five variations in partition encoding reference lines, for all six echoes, and their mean SNR, are listed in Table 16.

echo	70_12	70_24	70_44	70_64	70_88
	SNR				
1	257.1	316.1	337.2	360.8	363.6
2	258.5	323.9	334.6	364.7	364.3
3	235.2	285.9	283.3	317.2	312.7
4	236.3	282.8	267.4	312.8	298.3
5	204.4	237.7	215.2	260.1	245.3
6	198.7	231.6	195.7	244.8	231.2
mean SNR	231.7	279.7	272.2	310.1	302.6

Table 16: Calculated SNR values for each of the six echoes of all measured variations in partition reference lines and their mean SNR. SNR is proportional to the number of reference lines and decreases with the echo number.

As can be seen, a quite similar trend is visible as in the variation of the phase encoding reference lines in Chapter 5.1.4.1. The SNR values are once again plotted in Figure 27 for easier comparison. The configuration with only 12 partition encoding reference lines results in the decidedly lowest overall SNR, while an increase in the number of 3D reference lines increases the SNR as would be expected from the results obtained in Chapter 5.1.4.1.
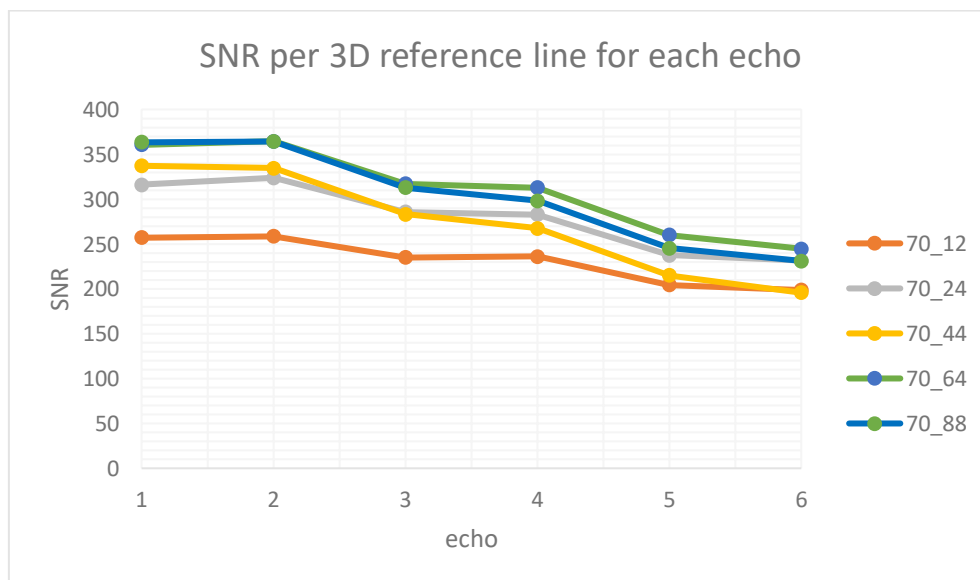
Figure 27: Calculated SNR for each of the six echoes for scans with a varying number of partition reference lines, with the naming scheme being #PE_#3D. A step-like reduction in SNR for increasing echo numbers can be seen. The measurement with only 12 reference lines in the partition direction shows exceptionally low SNR.

A small dip in mean SNR can be seen in this measurement series again for the configuration with a "medium" amount of 3D reference lines, namely 70_44.

The magnitude images and calculated SNR maps of all six echoes for three reference line configurations, more precisely 70_12, 70_44 and 70_88, are shown in Figure 28.
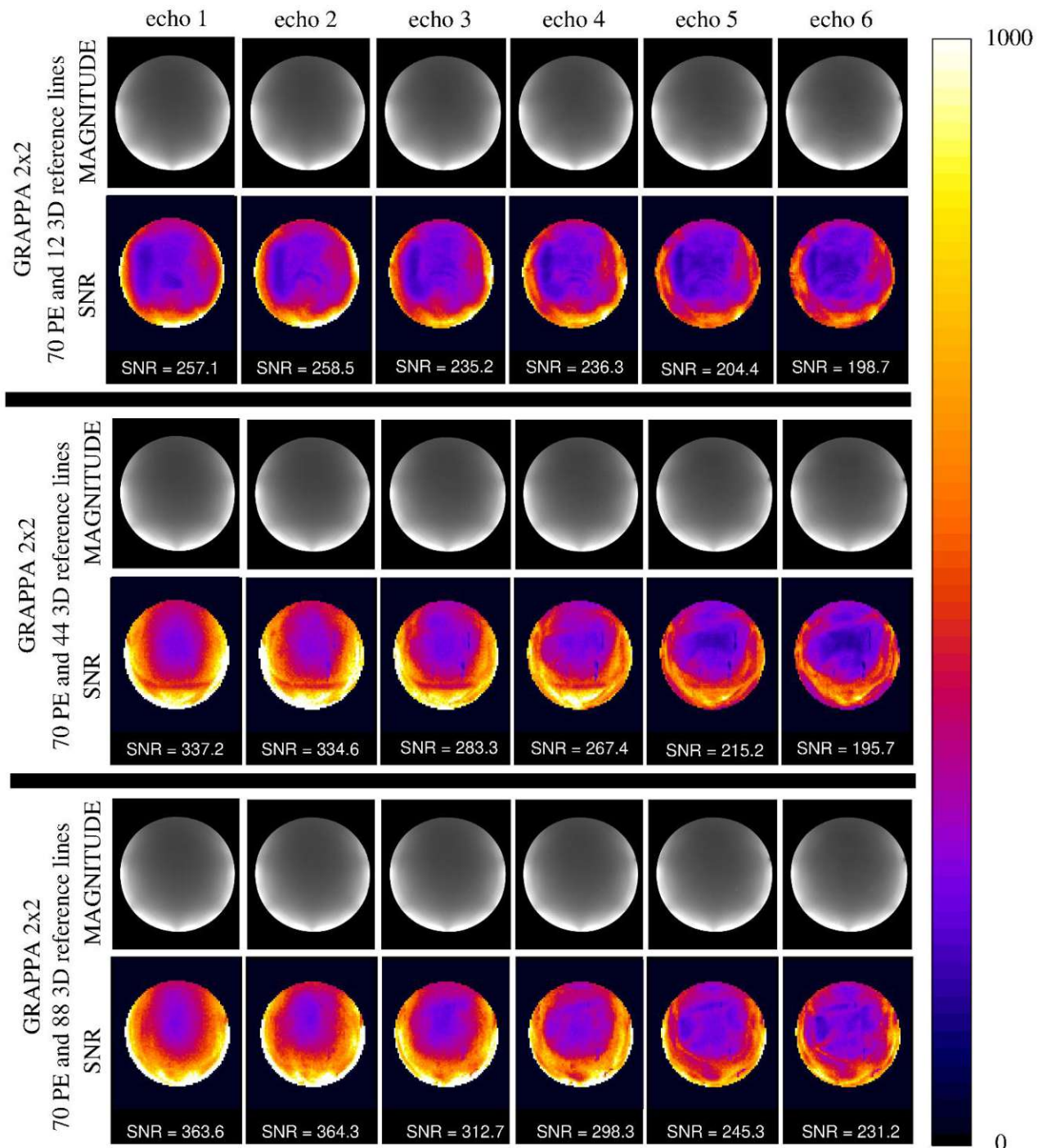
Figure 28: Magnitude images and the corresponding calculated SNR maps for all six echoes of GRAPPA 2×2 scans measured at 3T for varying numbers of partition encoding reference lines. The top two rows show a scan with 12 partition reference lines, the middle with 44 and the bottom with 88 3D reference lines. While all three scans look quite similar in their magnitude images, the SNR maps show a clear increase according to the number of reference lines (higher SNR values correspond to brighter SNR maps).

As can be seen in Figure 28, contrary to the findings in Chapter 5.1.4.1, all magnitude images from each of the three configurations are free from any visible aliasing artifacts. The

48

configuration with the lowest number of 3D reference lines (70_12) shows low, but consistent SNR with slightly improved spatial homogeneity compared to the other configurations. The overall SNR increases for higher numbers of 3D reference lines, which can be seen by the brighter colours of the SNR maps, corresponding to higher SNR values. This trend is very similar to what occurred for increased numbers of phase encoding reference lines. Once again, echoes five and six show a considerable decrease in SNR compared to earlier echoes.

The mean SNR, SNR efficiency and acquisition time for all five configurations in the number of 3D encoding lines are listed in Table 17. In the mean SNR values, a trend towards higher SNR for an increased number of partition encoding reference lines can be seen.

variation	mean SNR (3D)	SNR eff. (3D)	TA [s]
70_12	231.7	13.2	307
70_24	279.7	15.9	309
70_44	272.2	15.4	314
70_64	310.1	17.4	318
70_88	302.6	16.8	324

Table 17: Calculated mean SNR, SNR efficiency and acquisition times depending on the number of reference lines in the partition direction (3D). Mean SNR is proportional to the number of reference lines, which corresponds to higher acquisition times. SNR efficiency is higher for scans measured with an increased number of reference lines.

The 70_12 variation has especially low SNR compared to the other configurations. Similar to what was observed in the PE reference line comparison, 70_44 shows lower mean SNR than 70_24, even though this variation has less reference lines and shorter acquisition time. This can be seen more clearly in Figure 29, where the SNR efficiency for the five configurations of
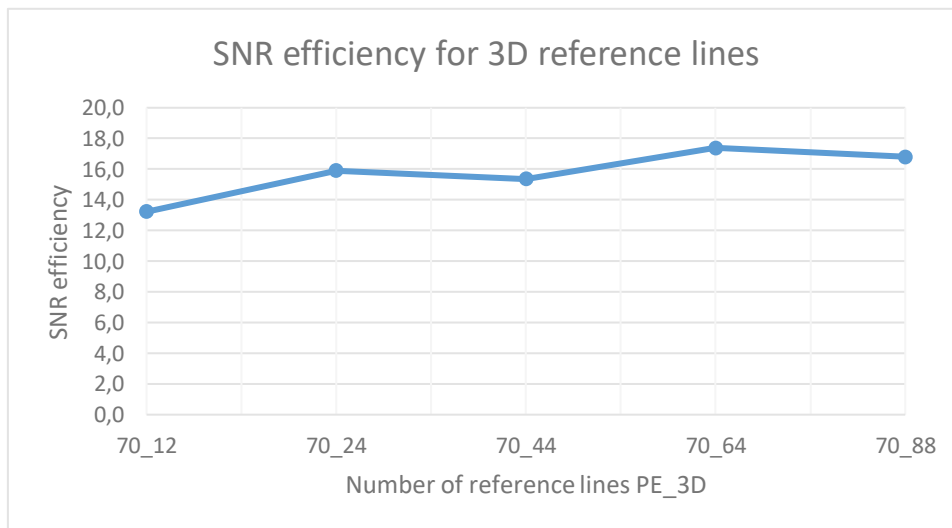
Figure 29: Calculated SNR efficiency of the five measured variations in the number of partition direction reference lines. A linear trend towards increased SNR efficiency for a higher number of reference lines can be observed.

3D reference lines is plotted. While there is an overall linear trend towards higher SNR for increased number of reference lines, the SNR efficiency was especially high for 70_24 and 70_64, which were even higher than the next configurations with more reference lines,

namely 70_44 and 70_88. This means that there may be a distinct sweet-spot for the number of 3D reference lines which is not necessarily the maximum.

The mean SNR for the configurations in the phase encoding and partition encoding direction are plotted in Figure 30 as a function of the acquisition time TA.
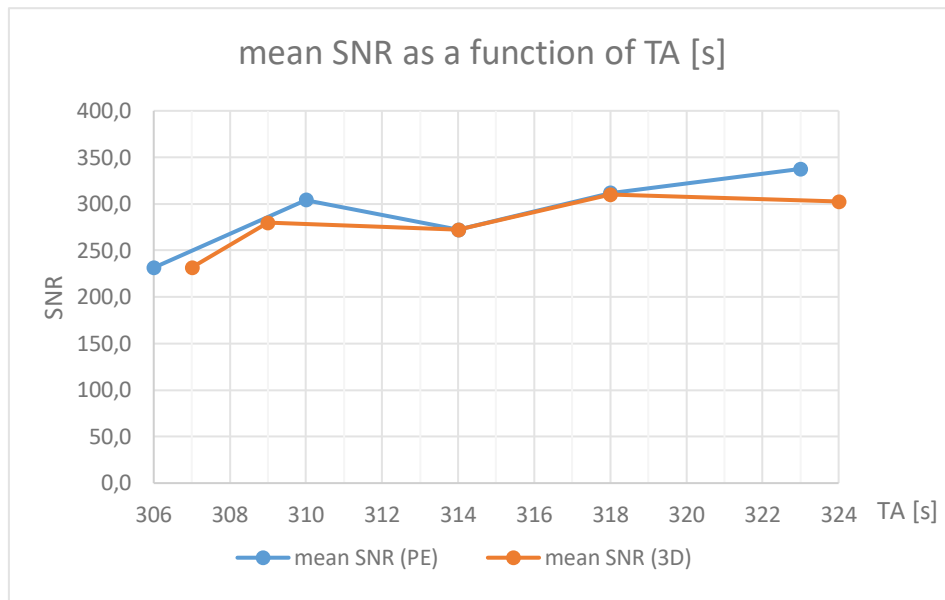
Figure 30: Mean SNR as a function of the acquisition time TA for both varying numbers of phase encoding- and partition direction reference lines. A similar trend can be seen for both directions with the SNR gains being slightly higher for phase encoding reference lines.

As can be appreciated, the 70_64 and 99_44 configurations have very similar SNR at the same acquisition time, the 70_44 variation is the same in both measurements and therefore identical. Using only 12 reference lines in either direction, be it 70_12 or 12_44, results in comparatively low SNR and even aliasing artifacts in the magnitude images in the case of the phase encoding direction. The 70_24 and 41_44 configurations showed considerably high SNR values relative to their acquisition time, meaning that their SNR efficiency was also quite high. Using the maximum number of possible reference lines seems to be more beneficial in the phase encoding direction compared to the partition encoding direction, where the SNR efficiency sweet-spot seems to be closer to the 70_64 configuration.

5.2 In-vivo Results

5.2.1 Magnitude Images of CAIPI 331 for separate and integrated reference lines at 7T

Figure 31 shows a comparison of in-vivo magnitude images for each of the six measured echoes, using three different configurations of reference lines, namely 24 GRE/separate, 24 integrated and 48 integrated reference lines.
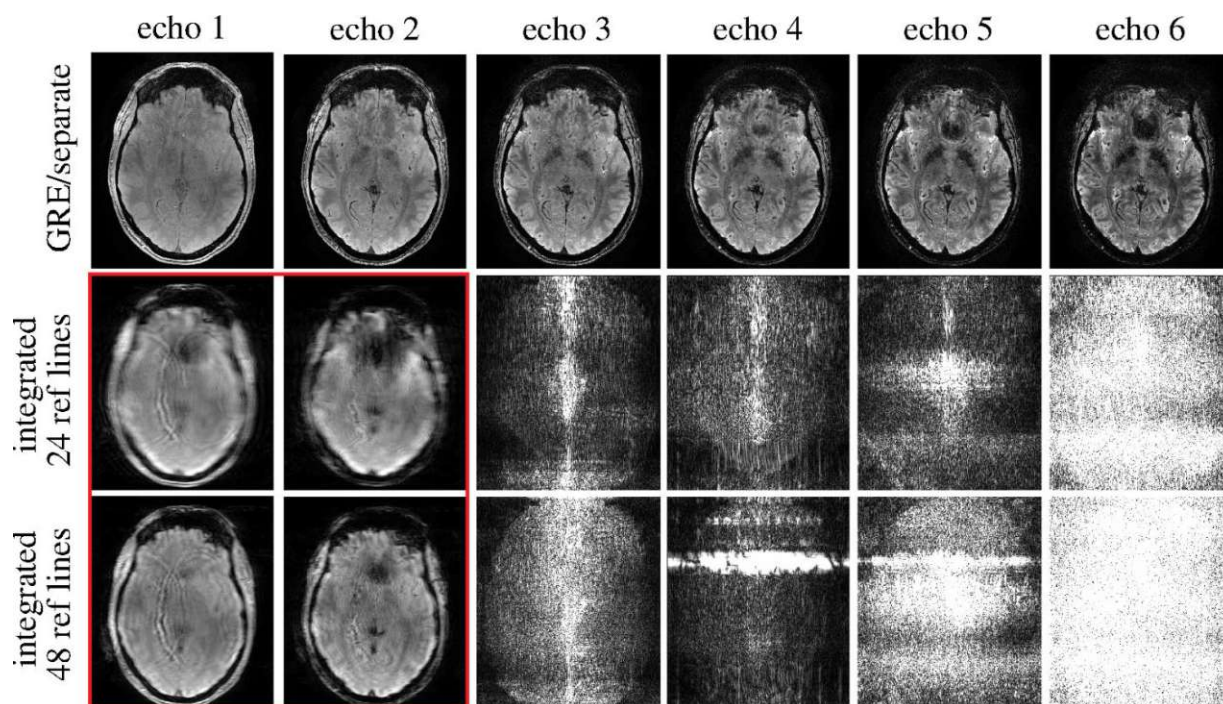
Figure 31: Comparison of magnitude images for each of the six echoes of scans measured with the VIBE sequence using CAIPI 331 acceleration at 7T. The top row shows the standard method of acquiring the reference lines in a prior separate scan, while the middle row depicts the use of 24 integrated reference lines in both phase encoding directions. The bottom row shows slight improvements by increasing the number of integrated reference lines to 48. This is visible in the reduced blurring of the first two echoes, marked by a red rectangle.

As can be seen, the scan measured using the standard 24 separate reference lines shows good image quality without any strong artifacts. In comparison to that, the scan acquired with 24 integrated reference lines shows very similar behaviour as seen in the phantom measurements, more precisely in Figure 17 of Chapter 5.1.1. Compared to the phantom scans, it is clearly visible that the images of the first to echoes, marked in Figure 31 by a red rectangle, are excessively blurred, which is not apparent in the phantom images. Increasing the number of integrated reference lines to 48, which did show improvements in image quality and even eliminated aliasing artifacts in some phantom scans, as seen in Figure 25 of Chapter 5.1.4.1, only lead to minor improvements in the in-vivo scans. The image acquired with 48 integrated reference lines appears only slightly sharper than its counterpart with 24 reference lines. It can also be seen that in echoes three to six of the same scans, increasing the number of reference lines even had a detrimental effect on the severity of the artifacts.

5.2.2 Magnitude Images of CAIPI 14X Shifts at 3T

Magnitude images were acquired with the single echo 3T Magnetom Protocol listed in Table 1, using CAIPIRINHA acceleration with R = 4, for all four possible reorder shifts. Except for the variation in the CAIPI shift, all other measurement parameters were kept the same. In Figure 32 the resulting images of CAIPI 140, CAIPI 141, CAIPI 142 and CAIPI 143 are shown.
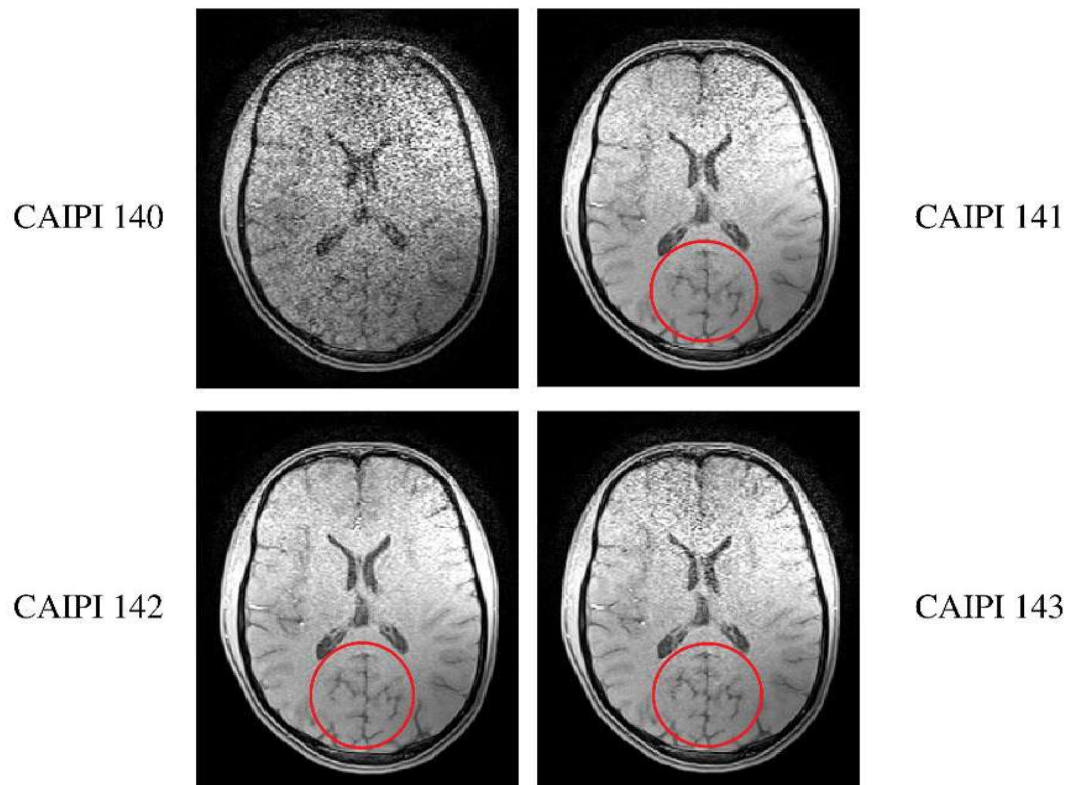
Figure 32: Comparison of the effects the CAIPI reorder shift has on the reconstructed magnitude image of scans acquired with a total acceleration factor of R = 4 at 3T. The reorder shift is written as the third number in the CAIPI naming scheme, with the first two numbers being the acceleration factors in the phase encoding- and partition encoding directions. CAIPI 140 has no reorder shift and is therefore identical to GRAPPA 1×4, CAIPI 142 results in noticeably less noise compare to CAIPI 141 and CAIPI 143, visible in the region marked by the red circles.

The CAIPI 140 image has very low image quality with high amounts of noise, as would be expected given that it is identical to GRAPPA 1×4 in its undersampling pattern. When applying a CAIPI reorder shift, image quality begins to increase drastically, with all three following CAIPI patterns being noticeably better than CAIPI 140. It can also be seen that, for the Prisma Fit scanner with this specific configuration of measurement parameters and the coil used, CAIPI 142 shows the best image quality. This can be seen most easily when looking at the region marked by the red circles in Figure 32, and the overall noise distribution of the image. The CAIPI 142 sampling pattern looks identical to the one of CAIPI 221 depicted in Figure 13 (d), but rotated by 90 degrees. This possibly leads to decreased g-factor maps due to the specific GRAPPA kernel geometries.

5.2.3 Magnitude Images of CAIPI 16X Shifts at 3T

A comparison of magnitude images for all possible CAIPI shifts for an acceleration of R = 6 in the partition encoding direction can be seen in Figure 33.
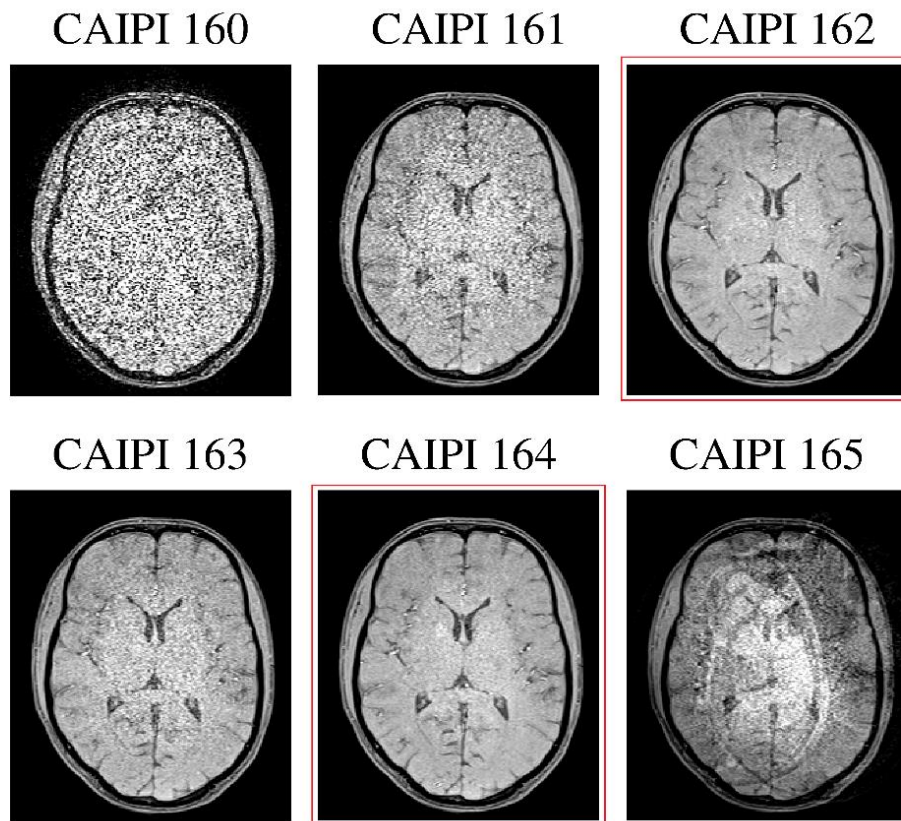
Figure 33: Comparison of how the CAIPI reorder shift affects the reconstructed magnitude image of scans acquired with an acceleration factor of R = 6 at 3 T. The reorder shift is written as the third number in the CAIPI naming scheme, the first number is the acceleration in the phase encoding direction and the second number the acceleration in the partition encoding direction. The top left CAIPI 160 is identical to GRAPPA 1×6, the reorder shift then increases up to the maximum of five. Highest image quality is seen for shifts of two and four, marked by red rectangles.

The scan acquired without any reorder shift, namely CAIPI 160 has very high noise, which - given that it is identical to GRAPPA 1×6 and an acceleration factor of R = 6 in just one direction - is to be expected. The corresponding undersampling patterns for all six configurations are visualized in Figure 34. Increasing the CAIPI reorder shift to one already improves the image quality quite drastically, and together with CAIPI 164 these two CAIPI schemes (marked by red rectangles) result in the overall best sharpness and the least amount of noise for this particular scan.
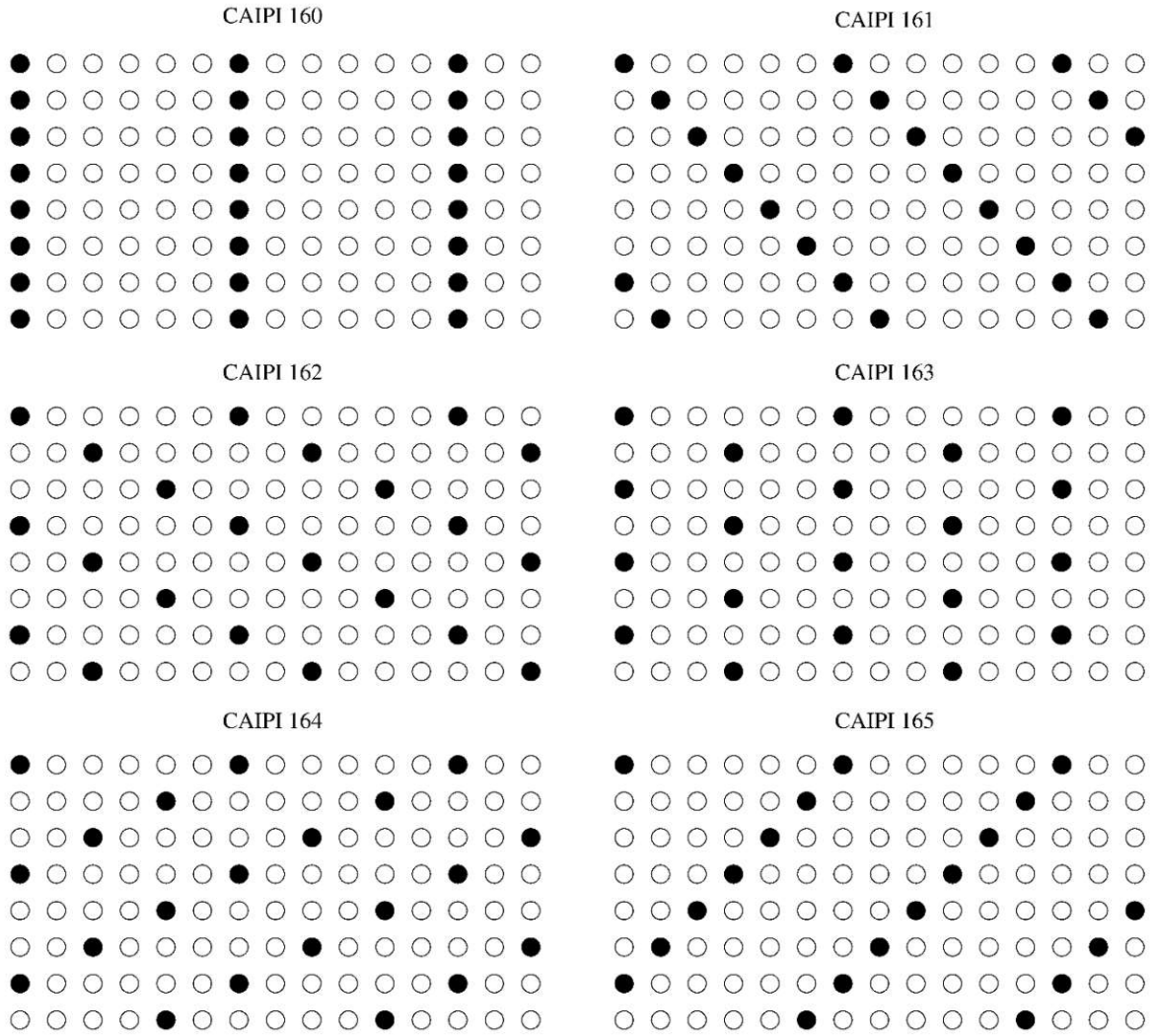
Figure 34: Schematic image of CAIPI undersampling schemes for an acceleration factor of six in the phase encoding direction. Sampled data points are marked in black while the not acquired ones are left blank. As can be seen, CAIPI 162 and CAIPI 164 show very similar patterns, which are identical except for a rotation, while CAIPI 163 has the overall best spatial distribution of acquired data points. CAIPI 160 is identical to GRAPPA 1×6.

Interestingly, CAIPI 163 with its undersampling pattern similar to CAIPI 331 creates noticeably more noise in the image compared to both CAIPI 162 and CAIPI 164, even though this configuration should result in the most evenly spaced-out sampling of k-space. CAIPI 165, which is most similar to CAIPI 161 due to the periodic nature of the reorder shift, looks surprisingly different. Besides the considerable amount of noise, aliasing artifacts begin to arise in this CAIPI scheme.

5.2.4 Comparison of Magnitude Images of GRAPPA 2×2, CAIPI 221, CAIPI 142 and GRAPPA 3×2, CAIPI 321, CAIPI 164 at 3T

In Figure 35, the magnitude images of six different acceleration schemes are shown. The differences in image quality between GRAPPA 2×2 and CAIPI 221 are very minor, to the point where these two images are almost indistinguishable. Similar to this, no clear advantage in improved image sharpness or noise reduction can be observed in the scan using CAIPI 142. When comparing the same acceleration schemes at a higher total acceleration factor of R = 6, differences between the three measured scans become more evident. This is especially visible when looking at the centre region of the scans, marked in Figure 35 by red circles. The CAIPI 321 image shows an increased amount of noise in this region compared to its GRAPPA 3×2 counterpart.
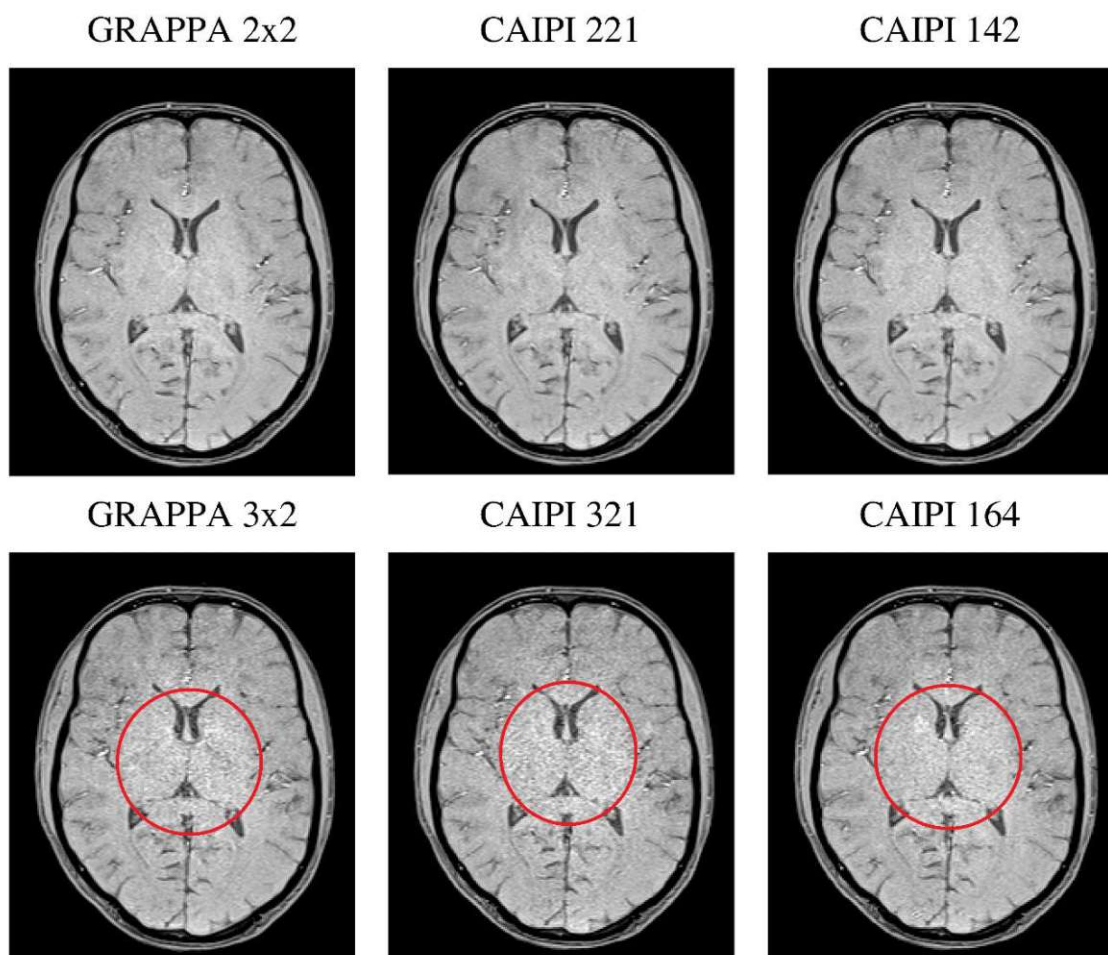
Figure 35: Comparison of magnitude images with a total acceleration factor of 4 on the top row and 6 at the bottom row. All scans were acquired at 3T, using a single echo VIBE sequence. Only very slight differences in image quality can be observed at a given acceleration factor, with CAIPI 142 and CAIPI 164 being marginally better than their GRAPPA counterparts.

The overall best image quality with the least amount of noise can be achieved in this case when using the CAIPI 164 acceleration scheme. While these are arguably just minor

improvements, switching to CAIPI 164 also results in a slightly lower acquisition time, as seen in Table 7.

5.2.5 Comparison of CLEAR-SWI Images of GRAPPA 3×2 and CAIPI 164 for different FOV's at 3T

Figure 36 shows a comparison between scans measured with GRAPPA 3×2 acceleration on the top, and CAIPI 164 in the bottom row, for three different configurations of FOV and resolution.
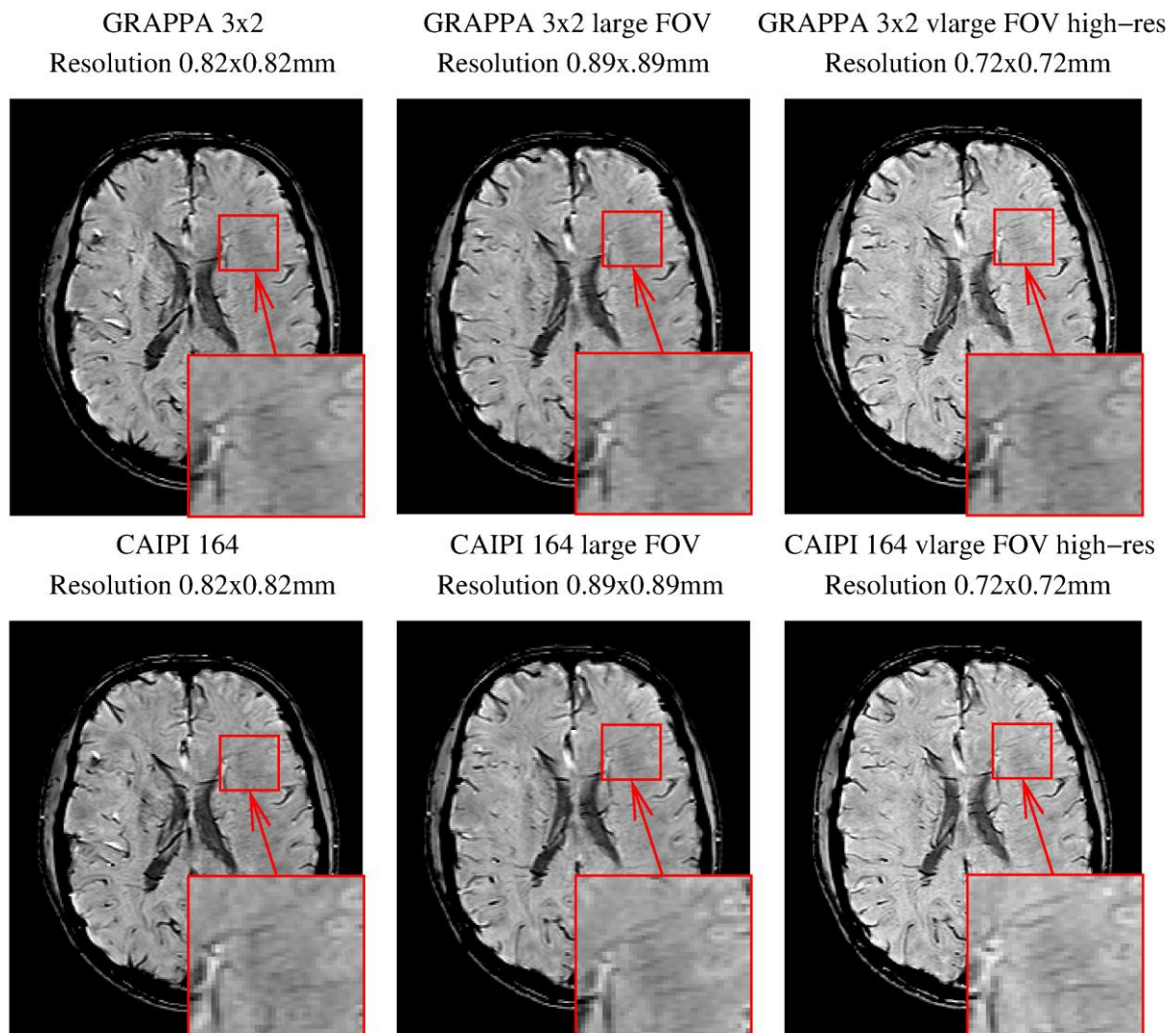
Figure 36: Comparison of CLEAR-SWI images created from multi-echo scans acquired with the VIBE sequence with GRAPPA and CAIPI acceleration methods, all scans have a total acceleration of R = 6. The red rectangles in the bottom right corners show zoomed in parts of the same image marked by an arrow. In these regions veins can be seen as black lines, with the CAIPI 164 image with higher resolution and increased FOV showing slightly increased visibility of the veins.

The scans measured with a larger FOV (middle) naturally appear to be slightly smaller and have marginally increased image quality due to a minor reduction in the resulting aliasing artifacts. Compared to that, the scans acquired with even larger FOV and increased resolution

show improved sharpness, this however also comes at the cost of higher acquisition times as seen in Table 8. Still, the acquisition times of these scans are very short, with the maximum being 154 seconds. Contrary to that, when comparing scans with the same FOV and resolution, which only differ in their acceleration method, the GRAPPA and CAIPIRINHA scans are almost indistinguishable.

5.2.6 Comparison of CLEAR-SWI Images of GRAPPA 2×2 and CAIPI 164 for different FOV's at 3T

In Table 18, a comparison of measurement parameters for a GRAPPA 2×2 and CAIPI 164 scan with increased FOV and resolution are listed. As can be appreciated from this table, the acquisition time for the CAIPI 164 scan is 12 seconds lower thanks to the higher acceleration factor, even though the resolution and field of view were increased.

Protocol	FOV	Matrix Size	Acquisition Time TA [s]
VIBE_GRAPPA_2×2	210×170	*256×208×80*	*166*
VIBE_CAIPI164_vlarge_fov_high_res	256×208	*352×286×80*	*154*

Table 18: Comparison of FOV, matrix size and acquisition time of a standard GRAPPA 2×2 scan and a CAIPI 164 scan with very large FOV and higher resolution with similar acquisition time at 3T.

Figure 37 shows the CLEAR-SWI images of GRAPPA 2×2 and the CAIPI 164 scan with the larger FOV and resolution, cropped to the same size as the GRAPPA scan for easier comparison (middle), as well as in its original form (scaled down).
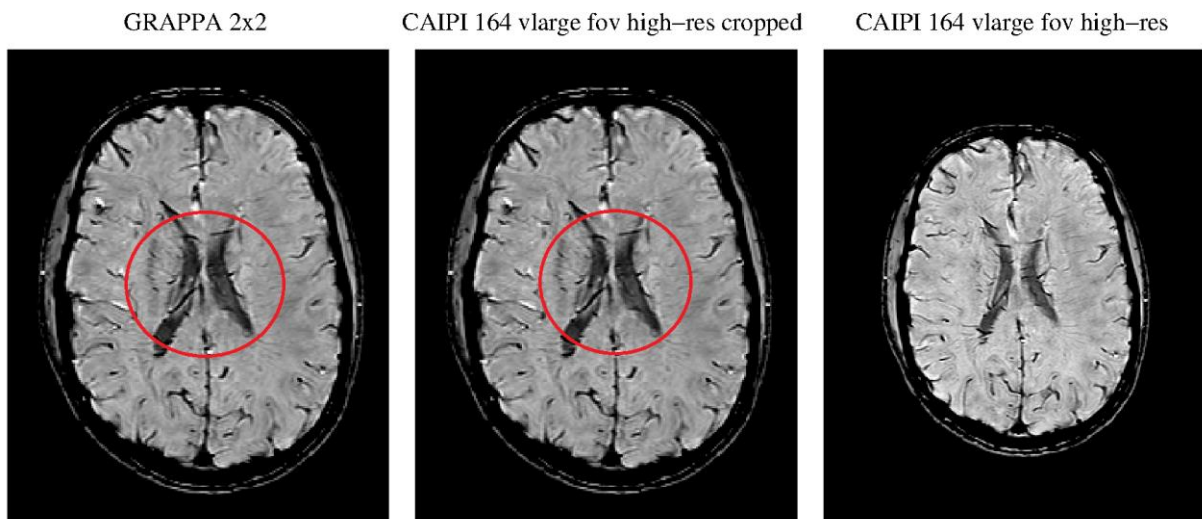
Figure 37: Comparison of CLEAR-SWI images created from multi-echo scans acquired with the VIBE sequence. The GRAPPA 2×2 images, while less accelerated, has lower FOV and resolution compared to the higher accelerated CAIPI 164 scan. Image quality is higher overall for CAIPI 164 due to the higher resolution, even though the acquisition time is shorter than for GRAPPA 2×2. The right image shows the original FOV of the CAIPI 164 scan.

The CAIPI 164 images shows slight improvements in image sharpness compared to GRAPPA 2×2, visible in the region marked by the red circle. Given that the acquisition time, in this

particular case, is still lower by around 9% for CAIPI 164, this method of acquiring images with higher acceleration factors in conjunction with increased FOV and resolution might prove beneficial for more applications.

5.2.7 Comparison of CLEAR-SWI Images of GRAPPA 2×2, GRAPPA 3×3, CAIPI 221 and CAIPI 331 at 7T

Figure 38 shows SWI images of GRAPPA 2×2, GRAPPA 3×3, CAIPI 221 and CAIPI 331.
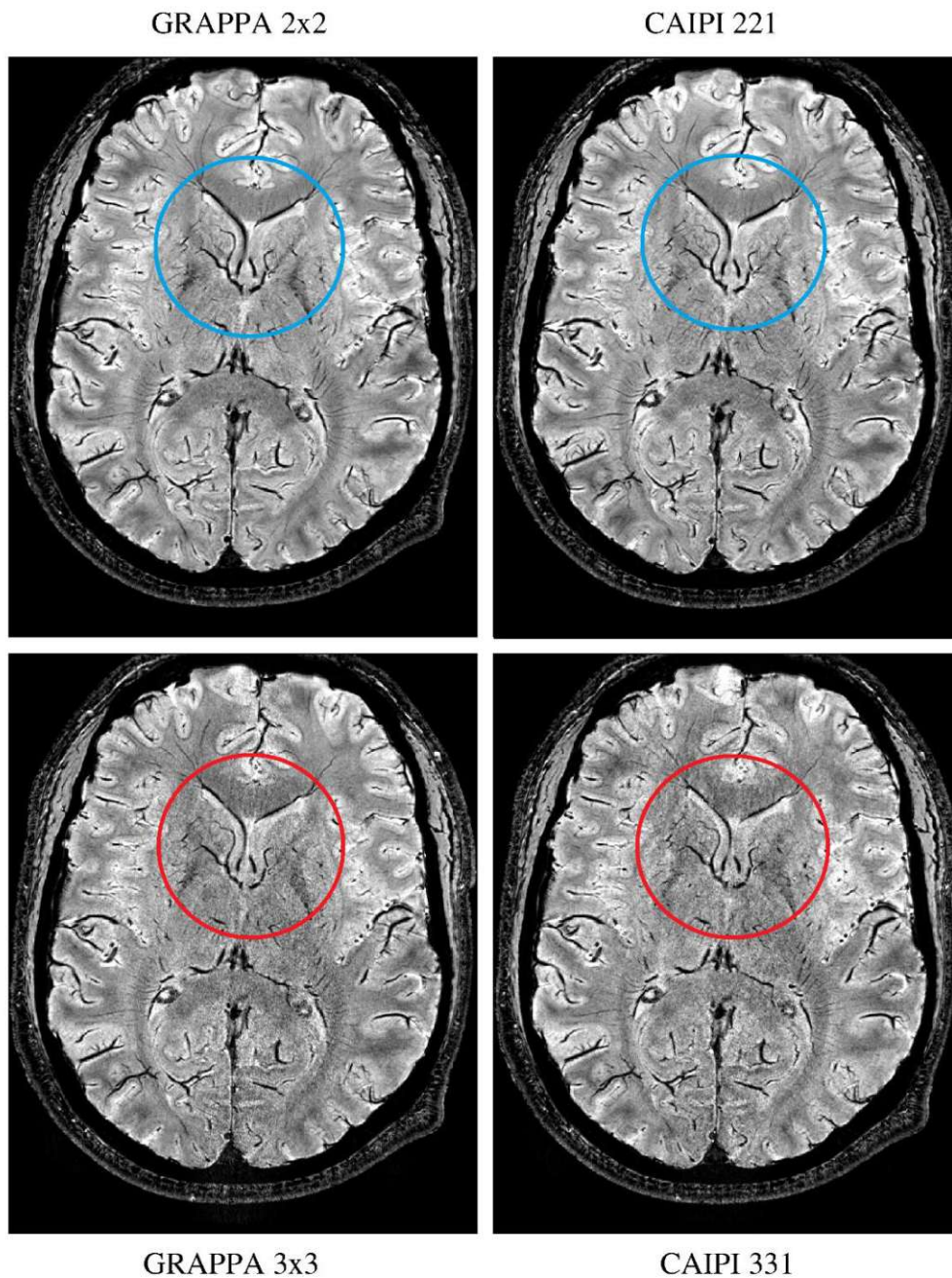
Figure 38: Comparison of in-vivo CLEAR-SWI images acquired at 7T with GRAPPA 2×2, GRAPPA 3×3, CAIPI 221 and CAIPI 331 acceleration. A noticeable increase in noise can be observed for the images measured with a total acceleration factor of R = 9 (bottom row), compared to their R = 4 counterparts (top row). A region where this

noise is especially evident is marked by red circles in the CAIPI 331 and GRAPPA 3×3 images and blue circle in GRAPPA 2×2 and CAIPI 221. There is no clearly visible improvement in image quality for CAIPI (right) compared to GRAPPA (left) at the same total acceleration factor.

A clear increase in noise can be observed in the images with a total acceleration factor of R = 9, in the bottom row, compared to their R = 4 counterparts in the top row. This is of course expected, since the SNR decreases proportional to the square root of the acceleration factor R, as seen in Eq. (20). This noise increase is especially noticeable when comparing the region marked by the blue circles in GRAPPA 2×2 and CAIPI 221 with the red circles in GRAPPA 3×3 and CAIPI 331. When comparing the GRAPPA and CAIPIRINHA accelerated images at the same total acceleration factor, more precisely GRAPPA 2×2 against CAIPI 221 and GRAPPA 3×3 with CAIPI 331, no clear improvement in image quality can be observed.

6 Discussion

The aim of this project was to compare and quantify the differences in SNR and image quality for in-vivo and phantom measurements of the GRAPPA and CAIPIRINHA acceleration methods. SNR was observed to be generally lower for CAIPI accelerated scans compared to their GRAPPA counterparts. Furthermore, CAIPI acceleration did not show significant improvements in sharpness and reduction of noise for SWI images over the more conventional GRAPPA acceleration. A combination of higher CAIPI acceleration factors, larger FOV and higher resolution, showed modest improvements in the visibility of veins compared to scans acquired using GRAPPA with lower acceleration factors at similar acquisition times. The SNR efficiency of GRAPPA accelerated scans increased for higher numbers of reference lines in the phase encoding and partition encoding directions.

At 7T field strength, the phantom measurements discussed in Chapter 5.1.1 revealed that the reference line scan mode integrated, in the case of CAIPI 331 acceleration, causes strong artifacts starting from the third of a total of six echoes. Besides this effect the acquisition time roughly doubled, which in turn increased the SNR of the first two echoes, which were unaffected from the previously mentioned effect. As feedback from the developers (private communications) revealed, this is most likely caused by an implementation issue regarding this option, with the reconstruction coefficients being calculated from scratch again for each individual echo. This would also explain the massively increased reconstruction times of around 40 minutes per scan instead of the more usual 2-3 minutes. Due to these strong artifacts, SNR efficiency was considerably lower than for the reference scan mode GRE/separate. It is important to note, however, that even using the standard separate reference lines, SNR efficiency was found to be lower overall for the scans acquired with the newer CAIPIRINHA acceleration, as opposed to their GRAPPA counterparts. Theories on why this might occur include that the GRAPPA kernels were not optimized for these high acceleration factors of R > 4, as they are not commonly used in clinical practice. This could explain why our results for CAIPI 164 and CAIPI 331 are lower than for GRAPPA 3×2 and GRAPPA 3×3. Another possibility that was brought to our attention is that the undersampling pattern for GRAPPA 3×3 might just be the ideal pattern for this specific scan we performed. To examine if these artifacts could be replicated in-vivo, measurements described in Chapter 5.2.1 were performed. Almost identical results to their phantom counterparts were obtained, with an increase in the number of reference lines only reducing the amount of blur in the first two echoes.

To investigate whether the same issues with integrated reference lines also occur on the better optimised and more thoroughly tested 3T Prisma Fit scanner, and to see if the trend of lower SNR for CAIPIRINHA acceleration continues, comparable measurements were repeated there, as described in Chapter 5.1.3. Very similar results were found at 3T, with alike to the findings at 7T, SNR was very low for all later echoes, starting from echo 3. One difference to the 7T results was the form of the artifacts in echoes five and six, which caused the magnitude

images to become saturated and therefore falsely increase SNR. This effect therefore seems to be independent on the field strength on scanner platform, and more likely stems from the reconstruction itself. Further feedback from the developers regarding the overall lower SNR of CAIPIRINHA mentioned that this could be caused by the inherent structural differences of a homogeneous phantom compared to a more varied brain, which does not allow for the full utilization of the added flexibility of the undersampling patterns provided by CAIPI. Furthermore, the standard number of 24 reference lines in phase encoding- and partition encoding directions were found to be challengingly low given the high resolution of the scans acquired with the 7T Protocol listed in Table 1.

Phantom measurements showed a clear trend towards higher SNR efficiency for increased PE and 3D reference lines. Increasing the reference lines in any of the two directions from the standard value to a higher amount successfully removed visible aliasing artifacts in the image. It would therefore be our recommendation to increase the default number of PE and 3D reference lines to at least a more moderate level, ideally even higher, to benefit from the increased SNR efficiency. This change could very easily be implemented into CLEAR-SWI and should lead to a noticeable improvement in image quality at only fractionally higher acquisition times. Using this method, it should be possible to generate diagnostically relevant SWI in the range of 2-3 minutes, compared to the current protocols with acquisition times between 6-9 minutes. This would be especially beneficial for patient groups with low compliance, where movement artifacts are of great concern.

In-vivo magnitude images, using separate and integrated reference lines and CAIPI 331 acceleration, similar to the phantom measurements in Chapter 5.1.1, showed higher SNR for the first two echoes and a steep decrease in SNR starting from echo 3, when integrated reference lines were used. In comparison to the phantom images, echoes one and two showed strong blurring which was not apparent in the comparable phantom scans, verifying the necessity for both in-vivo and phantom measurements to accurately determine the SNR and effective image quality.

Regarding the assumed benefits of CAIPIRINHA acceleration for in-vivo measurements, it was first investigated which CAIPI shift patterns result in the highest image quality, meaning the best sharpness and lowest amount of noise perceivable in the image. As described in more detail in Chapter 5.2.2, the highest image quality was perceived for CAIPI 142, which is not especially surprising, given that this configuration leads to the most even k-space sampling for this given acceleration. Similar measurements, discussed in Chapter 5.2.3, were performed for a total acceleration factor of R = 6, and out of all these scans, CAIPI 164 showed the least amount of noise, which given that this CAIPI shift does not create the most evenly spaced out sampling pattern, was less anticipated compared to the results obtained at a total acceleration of four. This is most likely caused by the effects the GRAPPA kernel geometry has for the individual undersampling patterns, and could not be accurately predicted prior to performing the measurements.

To try and replicate the results published in Figure 7A and 7B of the Magnetom Flash 1/2012 [43] article on CAIPIRINHA acceleration, single-echo in-vivo measurements were acquired using the 3T Magnetom protocol listed in Table 1. Besides the in the article compared GRAPPA 2×2 and CAIPI 221 accelerations, the previously determined coil and object specific optimal CAIPI scheme 142 was acquired as well. Similar scans with R = 6, namely GRAPPA 3×2, CAIPI 321 and CAIPI 164 were also compared to each other.

While CAIPI 142 shows minor improvements over CAIPI 221 and in the same way CAIPI 164 having slightly higher image quality compared to CAIPI 321, even the optimal CAIPI schemes only show marginal improvements over their GRAPPA 2×2 and GRAPPA 3×2 counterparts. Regarding the comparison of GRAPPA 2×2 against CAIPI 221 shown in Figure 7A and 7B of the Magnetom Flash article, which showed clearly visible improvements in the case of CAIPI 221, the scans measured with nearly identical parameters were almost indistinguishable on our 3T Prisma Fit scanner using the 20-channel head coil, as described in Chapter 5.2.4. The main difference of our measurements to the ones mentioned in the article is the use of a 3T Magnetom Skyra scanner instead of the 3T Prisma Fit scanner of the HFMRC centre and the use of different 20-channel head coils. Parameters such as the number and mode of the reference lines, echo- and repetition time, resolution and FOV were identical.

In order to investigate whether the benefits of CAIPIRINHA acceleration would become more pronounced in the case of SWI, CLEAR-SWI images were created from multi-echo scans measured with the 3T Multi-echo protocol listed in Table 1, as described in Chapter 5.2.5. While no significant improvements could be found for CAIPI 164 over the more conventional GRAPPA 3×2, both acceleration methods did benefit from increasing the FOV and resolution. The bigger field-of-view likely reduces the amount of aliasing artifacts inside the centre of the image, while the increased resolution makes up for the relatively reduced size of the measured object due to the FOV increase. While these changes naturally lead to higher acquisition times, the improvement in image quality was sizeable enough to warrant a comparison between CAIPI 164 with very large FOV and higher resolution to the less accelerated GRAPPA 2×2, as discussed in Chapter 5.2.6. Considering that the acquisition time of the CAIPI 164 scan is around 9% lower compared to GRAPPA 2×2, while still maintaining comparable image quality, this method of acquiring higher accelerated scans with increased FOV and resolution could be a useful alternative to acquiring the scans at lower acceleration.

CLEAR-SWI images were acquired using the 7T Protocol listed in listed in Table 1, with high resolutions for GRAPPA 2×2, GRAPPA 3×3, CAIPI 221 and CAIPI 331 acceleration. Comparisons between the GRAPPA and CAIPIRINHA accelerated images at the same total acceleration factor showed no clear improvement in image quality.

Overall, the benefits of CAIPIRINHA acceleration published in [41-43] by the Siemens developers could not be replicated using the scanners available at the HFMRC centre, even when using near identical scan parameters with a comparable coil. Most independent publications about the use of CAIPIRINHA concern themselves with abdominal and cardiac

imaging using breath-hold experiment at 3T, with accelerations factors often not exceeding R = 4. In these applications, scans measured using CAIPIRINHA have shown to be vastly superior in terms of image quality compared to their GRAPPA counterparts [57-60]. While these results seem promising, the low resolution and extremely short acquisition times of around 20 seconds may not make these scans the best estimate for the performance of CAIPIRINHA at high resolution structural brain imaging at ultra-high field strengths.

Nonetheless the results obtained within these publications are not questioned in any way, rather it is simply stated that for our specific circumstances, with the 7T Siemens Magnetom and the 3T Prisma Fit scanners, using the mentioned coils as well as the available VIBE sequence (fl3d_vibe) and measurement parameters listed in Chapter 3, could not replicate such benefits of CAIPIRINHA over the conventional GRAPPA acceleration. Possible reasons for the discrepancy in the original and our replicated results could be the different software versions which run on their 3T Magnetom Skyra (XA) and the 3T Prisma Fit (VE12U) at the HFMRC. The implementation of CAIPI is most likely different between the two software versions. An additional factor is that Figure 7 of the Magnetom Flash article only consists of one GRAPPA 2×2 and one CAIPI 221 scan, from one volunteer. Varying degrees of movement during the two scans may have led to more pronounced differences in the GRAPPA and CAIPI scans.

Limitations to our results are that due to the sheer flexibility of CAIPIRINHA acceleration with its reorder shift, only a small selection of the countless possible undersampling patterns could be compared extensively. Especially in the case of in-vivo scans, which require a volunteer, not all possible CAIPI schemes could be compared, and overall, the sample size of independent in-vivo samples could have been higher in order to more accurately estimate the results. Similarly, due to the extremely long acquisition times non-accelerated scans have for these high-resolution protocols, in conjunction with time-constraints based on the available scan-times, g-factor maps were only created for one of the earlier measurements, where motion artifacts were still less of a concern. This is most likely the reason why the first scans in this measurement series, namely GRAPPA 2×2 and CAIPI 221, show different behaviour to any of the later acquired scans, with the SNR of CAIPI 221 being higher than for GRAPPA 2×2. While additional g-factor maps of course would have had no direct impact on the results discussed in Chapter 5, they might have led to better insight into why exactly the SNR and image quality is not considerably higher in the case of CAIPIRINHA acceleration.

Overall, given our current understanding on the matter, and taking the obtained results into consideration, an implementation of CLEAR-SWI into the VIBE sequence solely for CAIPI acceleration may not seem especially beneficial at this point in time. The added flexibility the CAIPIRINHA acceleration offers in the achievable undersampling schemes, might still prove to be more useful in certain applications. Accounting for this extra adjustability, as well as the fact that future findings could very well solve the issues we have found during our research, the implementation might nevertheless be worth it. Notably the VIBE sequence has all the

other functionalities of the currently for CLEAR-SWI used GRE sequence, and can still be used for the standard GRAPPA accelerated scans until further insights are found.

7 Conclusion

In conclusion, using the integrated reference lines option in conjunction with CAIPIRINHA acceleration causes strong artifacts for later echoes and extremely long reconstruction times, due to implementation issues. This effect renders the resulting scans unusable and therefore the default GRE/separate reference line option should be used in most circumstances.

Contrary to expectations, SNR was observed to be lower overall for CAIPI accelerated scans as opposed to their GRAPPA counterparts. Similarly, the results published in the Magnetom Flash 1/2012 [43] article on CAIPIRINHA could not be replicated at the HFMRC centre.

Qualitative comparisons of the image sharpness and amount of noise did not show substantial improvements in CLEAR-SWI images for CAIPI acceleration compared to the more conventional GRAPPA. Images acquired with higher CAIPI acceleration factors, in conjunction with larger FOV and higher resolution, showed slight improvements in image quality compared to scans using lower GRAPPA acceleration at comparable acquisition times.

The SNR efficiency of scans acquired using GRAPPA acceleration increased according to the number of reference lines in the phase encoding and partition encoding directions. Increasing the default values of reference lines used within the GRE sequence for CLEAR-SWI should consequently results in higher SNR.

A future implementation of CLEAR-SWI into the VIBE sequence may still become valuable in terms of the added flexibility it offers in the achievable undersampling schemes, due to the CAIPI reorder shift, which might be beneficial in certain applications. Additionally, future research may reveal deeper insights into what might have caused the described issue and thus unlock the full potential of CAIPIRINHA acceleration. Based on the current findings, increasing the default number of reference lines, and if needed the resolution and FOV, at 7T should make it possible to generate diagnostically relevant SWI with acquisition times ranging between 2-3 minutes. Compared to the currently performed protocols, with acquisition times in the range of 6-9 minutes, this could be especially beneficial in patient groups with low compliance, where movement artifacts are a major concern.

List of Figures:

List of Tables

List of Equations

8 Reference

[1] R. Rao, R. Venkatesan, and S. Geethanath, "Role of MRI in medical diagnostics," *Resonance*, vol. 20, pp. 1003–1011, Nov. 2015, doi: 10.1007/s12045-015-0268-2.

[2] P. Balchandani and T. P. Naidich, "Ultra-High-Field MR Neuroimaging," *AJNR Am. J. Neuroradiol.*, vol. 36, no. 7, pp. 1204–1215, Jul. 2015, doi: 10.3174/ajnr.A4180.

[3] H. A. Chapman, D. Bernier, and B. Rusak, "MRI-related anxiety levels change within and between repeated scanning sessions," *Psychiatry Res.*, vol. 182, no. 2, pp. 160–164, May 2010, doi: 10.1016/j.pscychresns.2010.01.005.

[4] M. Zaitsev, J. Maclaren, and M. Herbst, "Motion artifacts in MRI: A complex problem with many partial solutions," *J. Magn. Reson. Imaging*, vol. 42, no. 4, pp. 887–901, 2015, doi: 10.1002/jmri.24850.

[5] H. R. Pardoe, R. K. Hiess, and R. Kuzniecky, "Motion and morphometry in clinical and nonclinical populations," *NeuroImage*, vol. 135, pp. 177–185, Jul. 2016, doi: 10.1016/j.neuroimage.2016.05.005.

[6] B. A. Duffy *et al.*, "Retrospective motion artifact correction of structural MRI images using deep learning improves the quality of cortical surface reconstructions," *NeuroImage*, vol. 230, p. 117756, Apr. 2021, doi: 10.1016/j.neuroimage.2021.117756.

[7] A. Deshmane, V. Gulani, M. A. Griswold, and N. Seiberlich, "Parallel MR imaging," *J. Magn. Reson. Imaging JMRI*, vol. 36, no. 1, pp. 55–72, Jul. 2012, doi: 10.1002/jmri.23639.

[8] D. Moratal, A. Vallés-Luch, L. Martí-Bonmatí, and M. Brummer, "k-Space tutorial: an MRI educational tool for a better understanding of k-space," *Biomed. Imaging Interv. J.*, vol. 4, no. 1, p. e15, Jan. 2008, doi: 10.2349/biij.4.1.e15.

[9] R. Pohmann, O. Speck, and K. Scheffler, "Signal-to-noise ratio and MR tissue parameters in human brain imaging at 3, 7, and 9.4 tesla using current receive coil arrays," *Magn. Reson. Med.*, vol. 75, no. 2, pp. 801–809, 2016, doi: 10.1002/mrm.25677.

[10] M. A. Griswold *et al.*, "Generalized autocalibrating partially parallel acquisitions (GRAPPA)," *Magn. Reson. Med.*, vol. 47, no. 6, pp. 1202–1210, 2002, doi: 10.1002/mrm.10171.

[11] F. Breuer, M. Blaimer, M. Griswold, and P. Jakob, "Controlled Aliasing in Parallel Imaging Results in Higher Acceleration (CAIPIRINHA)". MAGNETOM Flash · 1/2012, pp. 135-142. Accessed: Apr. 17, 2024. [Online]. Available: https://cdn0.scrvt.com/39b415fb07de4d9656c7b516d8e2d907/1800000000124408/aa 62f710d293/Controlled_Aliasing_in_Parallel_Imaging_Results_CAIPIRINHA_1800000000 124408.pdf

[12] E. M. Haacke, Y. Xu, Y.-C. N. Cheng, and J. R. Reichenbach, "Susceptibility weighted imaging (SWI)," *Magn. Reson. Med.*, vol. 52, no. 3, pp. 612–618, 2004, doi: 10.1002/mrm.20198.

[13] K. Eckstein *et al.*, "Improved susceptibility weighted imaging at ultra-high field using bipolar multi-echo acquisition and optimized image processing: CLEAR-SWI," *NeuroImage*, vol. 237, p. 118175, Aug. 2021, doi: 10.1016/j.neuroimage.2021.118175.

[14] K. Eckstein *et al.*, "Computationally Efficient Combination of Multi-channel Phase Data From Multi-echo Acquisitions (ASPIRE)," *Magn. Reson. Med.*, vol. 79, no. 6, pp. 2996–3006, 2018, doi: 10.1002/mrm.26963.

[15] W. Li *et al.*, "Differential developmental trajectories of magnetic susceptibility in human brain gray and white matter over the lifespan," *Hum. Brain Mapp.*, vol. 35, no. 6, pp. 2698–2713, Sep. 2013, doi: 10.1002/hbm.22360.

[16]   E. M. Haacke *et al.*, "Imaging iron stores in the brain using magnetic resonance imaging," *Magn. Reson. Imaging*, vol. 23, no. 1, pp. 1–25, Jan. 2005, doi: 10.1016/j.mri.2004.10.001.

[17]   B. Bilgic, A. Pfefferbaum, T. Rohlfing, E. V. Sullivan, and E. Adalsteinsson, "MRI estimates of brain iron concentration in normal aging using quantitative susceptibility mapping," *NeuroImage*, vol. 59, no. 3, pp. 2625–2635, Feb. 2012, doi: 10.1016/j.neuroimage.2011.08.077.

[18]   E. Koh, E. R. Walton, and P. Watson, "VIBE MRI: an alternative to CT in the imaging of sports-related osseous pathology?," *Br. J. Radiol.*, vol. 91, no. 1088, p. 20170815, Jul. 2018, doi: 10.1259/bjr.20170815.

[19]   I. I. Rabi, J. R. Zacharias, S. Millman, and P. Kusch, "Milestones in magnetic resonance: 'a new method of measuring nuclear magnetic moment' . 1938," *J. Magn. Reson. Imaging JMRI*, vol. 2, no. 2, pp. 131–133, 1992, doi: 10.1002/jmri.1880020203.

[20]   J. Soto Alvarez, "Quantum-mechanical aspects of magnetic resonance imaging," *Rev. Mex. Fis.*, vol. 63, pp. 48–55, Jan. 2017.

[21]   R. W. Brown, Y.-C. N. Cheng, E. M. Haacke, M. R. Thompson, and R. Venkatesan, Eds., *Magnetic resonance imaging: physical principles and sequence design*, Second edition. Hoboken, New Jersey: Wiley Blackwell, 2014.

[22]   V. P. B. Grover, J. M. Tognarelli, M. M. E. Crossey, I. J. Cox, S. D. Taylor-Robinson, and M. J. W. McPhail, "Magnetic Resonance Imaging: Principles and Techniques: Lessons for Clinicians," *J. Clin. Exp. Hepatol.*, vol. 5, no. 3, pp. 246–255, Sep. 2015, doi: 10.1016/j.jceh.2015.08.001.

[23]   M. A. Bernstein, K. F. King, and X. J. Zhou, *Handbook of MRI Pulse Sequences*. Elsevier, 2004.

[24]   M. Markl and J. Leupold, "Gradient echo imaging," *J. Magn. Reson. Imaging*, vol. 35, no. 6, pp. 1274–1289, 2012, doi: 10.1002/jmri.23638.

[25]   D. Folio and A. Ferreira, "Two-Dimensional Robust Magnetic Resonance Navigation of a Ferromagnetic Microrobot Using Pareto Optimality," *IEEE Trans. Robot.*, vol. 33, pp. 583–593, Jun. 2017, doi: 10.1109/TRO.2016.2638446.

[26]   Martin Meyerspeer, Albrecht Ingo Schmid., "Basic Seminar: Basics of MR Physics. Lecture 6-8.," Medical University of Vienna. Dec. 2023

[27]   Martin Meyerspeer, Albrecht Ingo Schmid., "Basic Seminar: Basics of MR Physics. Lecture 4-5.," Medical University of Vienna. Dec. 2023

[28]   R. Graaf, "In Vivo NMR Spectroscopy: Principles and Techniques: 2nd Edition," *Vivo NMR Spectrosc. Princ. Tech. 2nd Ed.*, pp. 1–570, Nov. 2007, doi: 10.1002/9780470512968.

[29]   Robin A. de Graaf, "Magnetic Resonance Imaging," in *In Vivo NMR Spectroscopy*, John Wiley & Sons, Ltd, 2019, pp. 211–252. doi: 10.1002/9781119382461.ch4.

[30]   R. E. Hendrick, "Breast MRI: Using Physics to Maximize Its Sensitivity and Specificity to Breast Cancer," Northwestern University's Feinberg School of Medicine. Jun. 2004. Accessed: Apr. 17, 2024. [Online]. Available: https://www.researchgate.net/figure/2D-gradient-echo-pulse-sequence-diagram-Each-line-of-the-diagram-has-the-same_fig2_228996690

[31]   "Multi-echo GRE - Questions and Answers in MRI." Accessed: Feb. 05, 2024. [Online]. Available: https://mriquestions.com/multi-echo-gre.html

[32]   C. Liu, W. Li, K. A. Tong, K. W. Yeom, and S. Kuzminski, "Susceptibility-Weighted Imaging and Quantitative Susceptibility Mapping in the Brain," *J. Magn. Reson. Imaging JMRI*, vol. 42, no. 1, pp. 23–41, Jul. 2015, doi: 10.1002/jmri.24768.

[33]   M. Kataoka *et al.*, "Contrast-Enhanced Volumetric Interpolated Breath-Hold Examination Compared with Spin-Echo T1-Weighted Imaging of Head and Neck Tumors," *Am. J. Roentgenol.*, vol. 184, no. 1, pp. 313–319, Jan. 2005, doi: 10.2214/ajr.184.1.01840313.

[34]   K. P. Pruessmann, M. Weiger, M. B. Scheidegger, and P. Boesiger, "SENSE: Sensitivity encoding for fast MRI," *Magn. Reson. Med.*, vol. 42, no. 5, pp. 952–962, 1999, doi: 10.1002/(SICI)1522-2594(199911)42:5<952::AID-MRM16>3.0.CO;2-S.

[35]   O. Dietrich, J. G. Raya, S. B. Reeder, M. F. Reiser, and S. O. Schoenberg, "Measurement of signal-to-noise ratios in MR images: Influence of multichannel coils, parallel imaging, and reconstruction filters," *J. Magn. Reson. Imaging*, vol. 26, no. 2, pp. 375–385, 2007, doi: 10.1002/jmri.20969.

[36]   M. J. Firbank, A. Coulthard, R. M. Harrison, and E. D. Williams, "A comparison of two methods for measuring the signal to noise ratio on MR images," *Phys. Med. Biol.*, vol. 44, no. 12, p. N261, Dec. 1999, doi: 10.1088/0031-9155/44/12/403.

[37]   F. A. Breuer, S. A. R. Kannengiesser, M. Blaimer, N. Seiberlich, P. M. Jakob, and M. A. Griswold, "General formulation for quantitative G-factor calculation in GRAPPA reconstructions," *Magn. Reson. Med.*, vol. 62, no. 3, pp. 739–746, 2009, doi: 10.1002/mrm.22066.

[38]   T. Yoshida, K. Shirata, A. Urikura, M. Ito, and Y. Nakaya, "Signal-to-noise ratio and parallel imaging performance of commercially available phased array coils in 3.0 T brain magnetic resonance imaging," *Radiol. Phys. Technol.*, vol. 8, no. 2, pp. 305–311, Jul. 2015, doi: 10.1007/s12194-015-0321-6.

[39]   D. Ennis and B. Hargreaves, "Rad229 – MRI Signals and Sequences, Lecture 07B, SNR_Relationships". Stanford University, 2020. Accessed: Apr. 17, 2024. [Online]. Available: https://web.stanford.edu/class/rad229/Notes/Lecture-07/Rad229_2020_Lecture07B_SNR_Relationships.pdf

[40]   J. Jin, M. Tourell, P Sati, S Patil, K Liu, J. Derbyshire, F. Han, Josef Pfeuffer, Saskia and Bollmann, Simon Robinson, Steffen Bollmann, Markus Barth, Kieran O'Brien, "Segmented 3D EPI with CAIPIRINHA Acceleration for Fast, High-Resolution T2*-weighted Imaging".

[41]   F. A. Breuer *et al.*, "Controlled aliasing in volumetric parallel imaging (2D CAIPIRINHA)," *Magn. Reson. Med.*, vol. 55, no. 3, pp. 549–556, 2006, doi: 10.1002/mrm.20787.

[42]   F. A. Breuer, M. Blaimer, R. M. Heidemann, M. F. Mueller, M. A. Griswold, and P. M. Jakob, "Controlled aliasing in parallel imaging results in higher acceleration (CAIPIRINHA) for multi-slice imaging," *Magn. Reson. Med.*, vol. 53, no. 3, pp. 684–691, 2005, doi: 10.1002/mrm.20401.

[43]   Felix Breuer; Martin Blaimer; Mark Griswold; Peter Jakob, "MAGNETOM Flash · 1/2012. Controlled Aliasing in Parallel Imaging Results in Higher Acceleration (CAIPIRINHA)", [Online]. Available: https://cdn0.scrvt.com/39b415fb07de4d9656c7b516d8e2d907/1800000000124408/aa62f710d293/Controlled_Aliasing_in_Parallel_Imaging_Results_CAIPIRINHA_1800000000124408.pdf

[44]   G. Verma and P. Balchandani, "Ultrahigh field MR Neuroimaging," *Top. Magn. Reson. Imaging TMRI*, vol. 28, no. 3, pp. 137–144, Jun. 2019, doi: 10.1097/RMR.0000000000000210.

[45]   B. A. Runderkamp, M. W. A. Caan, W. Van Der Zwaag, and A. J. Nederveen, "The way back and ahead: MR physics at ultra-high field," in *Advances in Magnetic Resonance*

Technology and Applications, vol. 10, Elsevier, 2023, pp. 3–18. doi: 10.1016/B978-0-323-99898-7.00020-1.

[46]   P. P. R. Ruetten, J. H. Gillard, and M. J. Graves, "Introduction to Quantitative Susceptibility Mapping and Susceptibility Weighted Imaging," *Br. J. Radiol.*, vol. 92, no. 1101, p. 20181016, Sep. 2019, doi: 10.1259/bjr.20181016.

[47]   "Magnetic Susceptibility - an overview | ScienceDirect Topics." Accessed: Feb. 08, 2024. [Online]. Available: https://www.sciencedirect.com/topics/medicine-and-dentistry/magnetic-susceptibility

[48]   A. Deistung, A. Rauscher, J. Sedlacik, J. Stadler, S. Witoszynskyj, and J. R. Reichenbach, "Susceptibility weighted imaging at ultra high magnetic field strengths: Theoretical considerations and experimental results," *Magn. Reson. Med.*, vol. 60, no. 5, pp. 1155–1168, 2008, doi: 10.1002/mrm.21754.

[49]   S. S. Oh *et al.*, "Improved susceptibility weighted imaging method using multi-echo acquisition," *Magn. Reson. Med.*, vol. 72, no. 2, pp. 452–458, 2014, doi: 10.1002/mrm.24940.

[50]   M. A. Schofield and Y. Zhu, "Fast phase unwrapping algorithm for interferometric applications," *Opt. Lett.*, vol. 28, no. 14, pp. 1194–1196, Jul. 2003, doi: 10.1364/ol.28.001194.

[51]   Eckstein K., Trattnig S., Robinson S.D., "High resolution frequency difference mapping using ASPIRE phase combination, in: Proceedings of the 26th Annual Meeting ISMRM. Presented at the ISMRM, Paris, France. 2018b.".

[52]   H.-B. Shin, H. Sheen, H.-Y. Lee, J. Kang, D.-K. Yoon, and T. S. Suh, "Digital Imaging and Communications in Medicine (DICOM) information conversion procedure for SUV calculation of PET scanners with different DICOM header information," *Phys. Medica PM Int. J. Devoted Appl. Phys. Med. Biol. Off. J. Ital. Assoc. Biomed. Phys. AIFB*, vol. 44, pp. 243–248, Dec. 2017, doi: 10.1016/j.ejmp.2017.05.063.

[53]   S. D. Robinson, "Siemens DICOM sort and convert to NIfTI." Accessed: Feb. 23, 2024. [Online]. Available: https://de.mathworks.com/matlabcentral/fileexchange/22508-siemens-dicom-sort-and-convert-to-nifti

[54]   M. Jenkinson, C. Beckmann, T. E. J. Behrens, M. W. Woolrich, and S. M. Smith, "FSL," *NeuroImage*, vol. 62, no. 2, pp. 782–790, 2012, doi: 10.1016/j.neuroimage.2011.09.015.

[55]   S. M. Smith *et al.*, "Advances in functional and structural MR image analysis and implementation as FSL," *NeuroImage*, vol. 23 Suppl 1, pp. S208-219, 2004, doi: 10.1016/j.neuroimage.2004.07.051.

[56]   Dr. Harald Werthner et al. HC DI MR R&D, "ICE User's Guide. Manual for ICE programmers. V 0.78a." May 15, 2017.

[57]   M. Ogawa *et al.*, "Shortened breath-hold contrast-enhanced MRI of the liver using a new parallel imaging technique, CAIPIRINHA (controlled aliasing in parallel imaging results in higher acceleration): a comparison with conventional GRAPPA technique," *Abdom. Imaging*, vol. 40, no. 8, pp. 3091–3098, Oct. 2015, doi: 10.1007/s00261-015-0491-z.

[58]   K. L. Wright *et al.*, "Clinical Evaluation of CAIPIRINHA: Comparison Against a GRAPPA Standard," *J. Magn. Reson. Imaging JMRI*, vol. 39, no. 1, Jan. 2014, doi: 10.1002/jmri.24105.

[59]   A. C. Morani *et al.*, "CAIPIRINHA-VIBE and GRAPPA-VIBE for Liver MR Imaging at 1.5T: a Comparative in vivo Patient Study," *J. Comput. Assist. Tomogr.*, vol. 39, no. 2, p. 263, Apr. 2015, doi: 10.1097/RCT.0000000000000200.

[60]   B. Stemkens *et al.*, "An optimization framework to maximize signal-to-noise ratio in simultaneous multi-slice body imaging," *NMR Biomed.*, vol. 29, no. 3, pp. 275–283, 2016, doi: 10.1002/nbm.3457.